Crownwalls with a fully curved face.

An experimental study.

D. Dermentzoglou

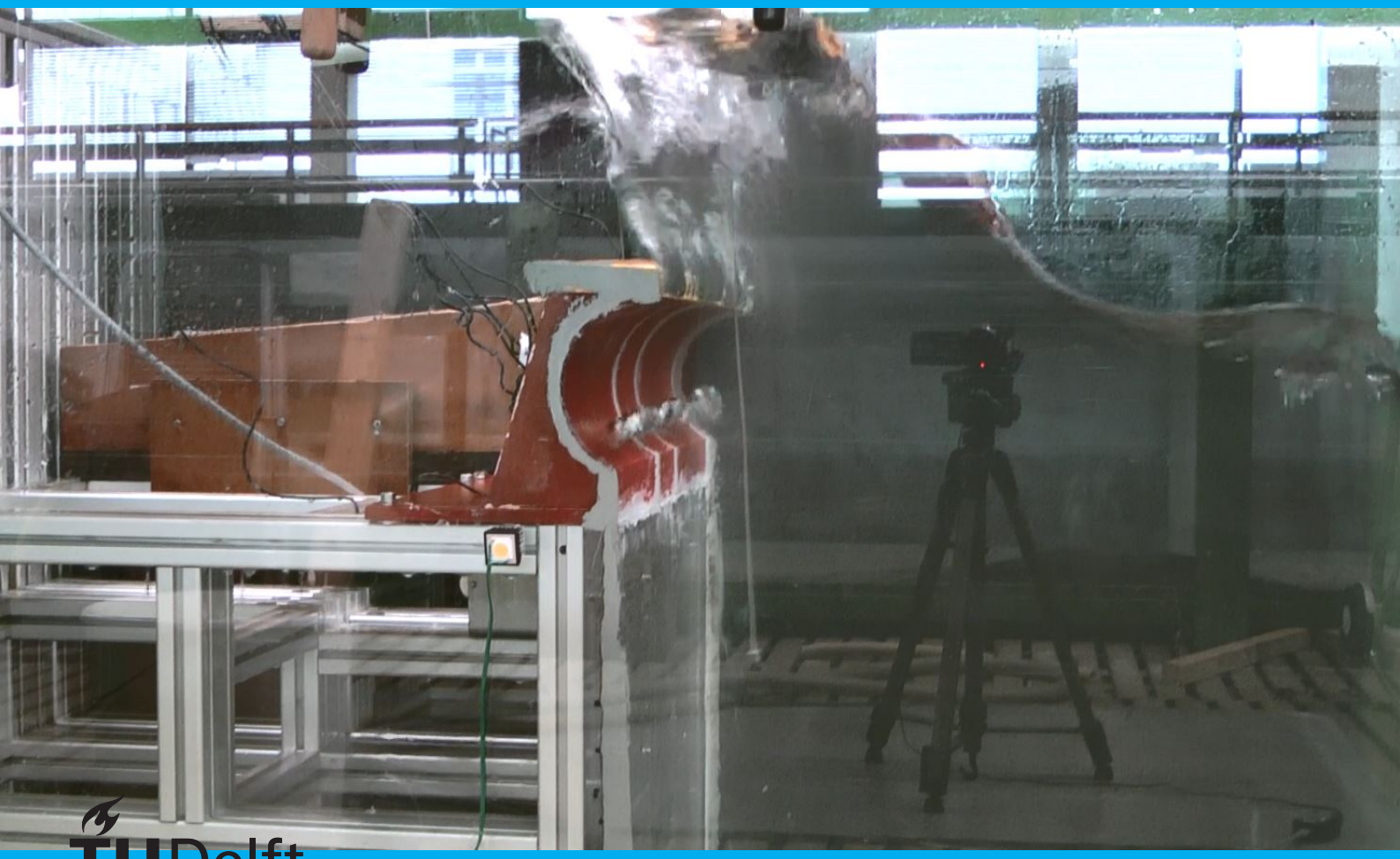

TUDelft

Crownwalls with a fully curved face.

An experimental study.

by

D. Dermentzoglou

in partial fulfillment of the requirements for the degree of Master of Science
at the Delft University of Technology,
to be defended publicly on Tuesday April 28, 2021 at 11:00 AM.

Student number:	4797817	
Project duration:	February 2, 2020 – April 28, 2021	
Thesis committee:	Dr. ir. A. Antonini	TU Delft, supervisor
	Dr. ir. B. Hofland	TU Delft
	Ir. E. de Almeida	TU Delft
	Dr. ir. P. de Girolamo	Sapienza University of Rome

An electronic version of this thesis is available at `http://repository.tudelft.nl/`.

TU Delft

Preface

This Master Thesis with the subject "*Crownwalls with a fully curved face. An experimental study.*" is the final part of my Master degree "*Hydraulic Engineering*" at the Delft University of Technology. I am very thankful for the opportunity I had to use the flume in the lab of fluid mechanics. It was truly a unique learning experience, as lab experiments give a much more direct sense of the processes studied.

Completing this thesis would not have been possible without the guidance of my Thesis committee. Firstly, I would like to thank Alessandro Antonini for chairing the committee, giving valuable advice and spending a lot of his time guiding me through the process of my Thesis. I also want to thank Bas Hofland for the guidance and coming up with ideas that greatly helped me proceed. I am very thankful to Ermano de Almeida, as his advice and methodology for calculating impulses were very useful. I want to express my gratitude to Paolo de Girolamo for coming up with the idea of the parapet and for the valuable advice. I am truly grateful to the University of l'Aquila for constructing the crownwalls and to *Sapienza University of Rome* and *TU Delft* for supporting this project.

Lastly, I want to thank the technicians of the hydraulic lab, Sander de Vree, Pieter van der Gaag and Arno Doorn, whose contributions were absolutely vital during the performing of the experiments. This project would not have been possible without them.

I wish you a pleasant read,

D. Dermentzoglou
Delft, March 2021

Contents

Summary

Vertical breakwaters are structures usually built in deep water and their main goal is reducing the wave agitation and overtopping volume of water reaching its port side. A pretty common tactic to further reduce overtopping is to apply crownwalls on top of the vertical breakwater, which is a superstructure that usually forms seaward extensions. There is a very large number of different shapes of crownwalls that have been applied over the years e.g. bullnoses with different exit angles, curved parapets, crownwalls with a fully curved face. The latter, is a very new design and research on the effect of this shape on the performance of a breakwater is very limited. This shape is most commonly applied for seawalls and not breakwater crownwalls and is commonly found in UK coasts (Penrhyn Bay, Guernsey, Scarborough), usually designed for breaking wave conditions. It is quite interesting though to explore the possibility of applying this type of crownwall in deep water and compare its behavior with a typical vertical breakwater. For this reason, the research question has been formulated as follows:

"How does a crownwall with a fully curved face perform in comparison with a vertical wall, in non–breaking wave conditions and in terms of loading and overtopping?"

Which can further be broken down in two sub-questions.

"What equations can be used to predict overtopping and loading on a crownwall?"

"How can the results from these equations be compared to a vertical wall?"

In order to give an answer to these questions, small scale experiments of the two structures are carried in a flume with a flat bottom. A setup is installed in a flume, which consists of a flat vertical wall model, on top of which the crownwalls are screwed. In order to provide stability to the system, the wall model is mounted on a 1.5 *ton* concrete block. The front seaside of the structure is positioned 33.33 m away from the wave generator. Two different superstructures are used during the tests, a flat crownwall which mimics a standard vertical wall and a crownwall with a fully curved face. The crest freeboard R_c is 0.20 m for both shapes, while the water depth for all experiments is set to 0.50 m with a horizontal bottom. An overtopping box is positioned behind the superstructures which collects overtopping volumes. A total of nine gauges are used to record water elevation in the flume and in the overtopping box, while eight pressure sensors are used to measure pressure on the surface of the superstructures. The experiments consist of 21 regular wave states, applied for 7 different values of target wave height ($H = 0.10m - 0.22m$) and for 3 values of wave steepness ($s = 3\% - 4\%$).

Although crownwalls manage to reduce overtopping volumes, this comes at the cost of increased loads. During experiments with large wave heights, the water column reaches the top of the recurve, gets blocked and deflected offshore, leading to very high impulsive pressures on the structure. For this reason, the variables considered for both shapes are the wave characteristics, overtopping (V), maximum pressure (P), force (F), force angle (θ) and force point of application (ζ). While for the wave states impacts occurred for the crownwall, the impulse (I) and its duration (t_{imp}) are considered as well.

A reflection analysis followed by a zero-down crossing analysis are performed in order to obtain wave period (T) and wave height (H) for each individual wave event. The linear dispersion relationship is used to calculate wave length (L). A reflection coefficient is calculated for each pair of aligned incident and reflected waves as the fraction of the incoming to reflected wave height, $K_{r,i} = \frac{H_{ref,i}}{H_{in,i}}$. The crownwall barely has an effect on the reflection coefficient for high relative freeboard values (R_c/H), as for the cases the water column does not reach the tip of the recurve, the mean values $K_{r,S1} \approx 0.94$ for the vertical wall and $K_{r,S2} \approx 0.92$ for the crownwall almost coincide. Lower R_c/H values lead to reduced reflection coefficient values as a result of overtopping.

This is calculated by using the signal from the wave gauge that is positioned in the overtopping box. A moving median is applied on this signal in order to remove noise and results in a modified signal with identifiable overtopping steps. As this phenomenon is found to be dominated by wave length and wave height,

the fraction of the *Ursell* number (U) and relative freeboard (R_c/H), $\frac{U}{R_c/H} = \frac{H^2L^2}{R_c d^3}$ is used to express it. The effectiveness of the crownwall in reducing overtopping volumes is found to be 100% for $15 < \frac{U}{R_c/H} < 25$, while higher values result in decreased values of this effectiveness.

The pressure analysis deals with the removal of thermal shock from the pressure signal and the calculation of maximum pressure, impulse and impulse duration for each single wave event. A smoothing function is applied on the pressure signals for both shapes in order to identify the quasi-static parts of the loading. The results of the vertical wall are found to show a great agreement with the results of $Goda$ at still water level. Pressure for the case of the vertical wall is found to be dominated by wave height, as steepness is of minor importance. The results of the crownwall show a great agreement with the vertical wall for $\frac{U}{R_c/H} < 15$, while higher waves that reach the top of the crownwall generate impacts near the outer seaward edge, leading to an increase of the mean value of maximum pressure up to 1100%. Pressure distribution on the crownwall is found to be dominated by wave height, while for $15 \leq \frac{U}{R_c/H} \leq 60$ steepness is also highly relevant. The values of impulse and its duration are calculated manually for each wave assuming that all pressure sensors record impulses with duration equal to the one recorded by the highest pressure sensor. The results of impulses show a similar trend to pressure results and are found to be less uncertain. The duration of the impulse is found to become shorter for increased wave loads.

The pressure signal is integrated on the surface of the crownwall in order to generate signals of force (F), angle relative to the ground (θ) and point of application (ζ) of the force. θ and ζ are found to be dominated by the relative freeboard R_c/H and acquire a stable mean value for $R_c/H \leq 1.17$, around $\theta = 25.1^\circ$ and $\zeta = 0.55R_c$. Force is found to follow a similar trend to pressure, as the distributions of the two variables have a very similar shape. The *Goda* formula underestimates F or ζ as obtained from the integration of P.

Corresponding equations are derived by curve fitting for each of the mentioned variables. These are overtopping (V), maximum pressure (P), impulse (I), impulse duration (t_{imp}), force (F), force angle (θ) and point of application (ζ). These variables are mostly expressed through $\frac{U}{R_c/H}$, while their range of application is expressed in terms of relative freeboard R_c/H, relative water depth d/L and wave steepness s.

In order to provide comparison tools between the two shapes, an equation is derived for the prediction of overtopping on a vertical wall. The formula of $Goda$ is also evaluated, which is found to predict loads accurately at still water level, but underestimate pressure at higher positions. Nevertheless, the employment of this formula to estimate loading on a vertical wall is suggested due to its range of applicability and high accuracy at SWL.

1

Introduction

Vertical breakwaters are structures usually built in deep water and their main goal is reducing the wave agitation and overtopping volume of water reaching its port side. Modern design guidelines (e.g. EurOtop; van der Meer et al.,2016) prose the solution of a vertical wall with extensions in the seaward direction, crownwalls, which help to further reduce the overtopping volume of water, leading to lower visual impact and eventually a more economical design. An example of the *Dover, UK* breakwater is shown in Figure 1.1.

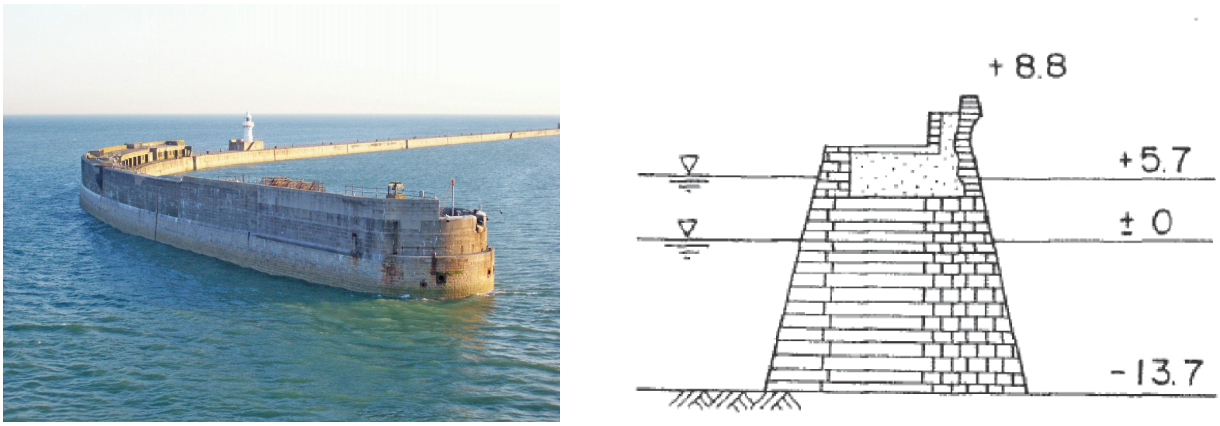

(a) Plan view.

(b) Cross section.

Figure 1.1: Vertical breakwater in Dover, UK. Image taken from Takahashi (2002).

Although these structures manage to reduce overtopping volumes, this comes at the cost of increased loads, as waves hit the front of the wall, reach its top, get blocked and deflected offshore, leading to very high impulsive pressures on the structure. This phenomenon was firstly highlighted by Castellino et al. (2018) for recurved parapets and called confined crest impact (*C-CI*). Parapets are rather stiff structures as they are usually made of reinforced concrete, rendering them quite sensitive to the exerted impulsive loads. Many failures of hydralic structures have been observed in the past as a result of wave impacts. More specifically, Allsop et al. (1997) report failures addressed to impacts in Wick (Scotland,1863), Catania (Italy,1930), Genoa (Italy,1955), Ventotene (Italy,1966), Palermo (Italy,1973), Sakata (Japan,1973), Bari (Italy,1974), Naples (Italy,1987), Mutsu-Ogawara (Japan,1991) Amlwch (Wales,1990) Porthcawl (Wales,1966), Schoonees (2014) and Roux (2013) report damage on the recurves in Strand (Africa) and Martinelli et al. (2018) report damages for parapets in Pico Island (Portugal) and Civitavecchia (Italy). The latter failure was demonstrated in Dermentzoglou et al. (2021) where through an offline coupling of computational fluid dynamics and finite element analysis, it was shown how impulsive forces lead to very high tensile stresses in the vertical direction and eventually to the failure of the crownwall e.g. Civitavecchia's one. Allsop and Bruce (2020a,b) performed stability analyses of historic breakwaters in Wick (failed between 1870-1877), Alderney (damaged even during construction, lost its outer length 1865–1889) by making use of the empirical formulas for wave impacts derived during the PROVERBS project for caisson breakwaters without overhangs (Oumeraci et al., 2001). The aforementioned

failures of breakwaters highlight the importance of taking impulsive wave forcing into account during design, in addition to the performance of the crownwall regarding overtopping.

1.1. Literature review

Wave forces on vertical walls have been investigated extensively in the past. The first attempt to measure wave impacts on a marine structure took place 150 years ago by Stevenson (1886) in Scerryvore Rocks. Hiroi (1920) suggested a formula for the average pressure from non-breaking waves, while later Sainflou (1928) developed a method for predicting wave pressure on a vertical wall. Neither of the formulas could be used for the prediction of impacts, as until 1935, no high-frequency instruments were available and impulsive forces could not be measured properly. The first high-frequency measurements that were able to capture this phenomenon were made in Dieppe by de Rouville et al. (1938). Bagnold (1939) a year later was able to capture the impulsive phenomenon in a laboratory, when he found that the maximum pressure occurred when there was air trapped by the wave. Based on Bagnold's piston model, Minikin (1963) developed a method for predicting impact forces caused by waves breaking directly on a vertical wall based on Bagnold's piston model and Ramkema (1978) described wave impacts caused by standing waves in front of a coastal structure, stating that most mathematical wave impact models originate from the Von Karman (1929) model. Goda (1974) developed a formula for predicting wave loads on a vertical wall, and determined the empirical parameters of the formula by making use of laboratory data and evaluating the performance of existing breakwaters. This method is given in Appendix B.1. This approach was extended further by Tanimoto et al. (1976) and Takahashi et al. (1994) by taking into account the effect of incident wave angle, berm, wave breaking and a sloping top. To this day, the *Goda* method with its extension for wave impacts by Takahashi (1993) is the main prediction method of wave forces on a vertical breakwater. Blackmore and Hewson (1984) later derived a formula for the prediction of impact pressures on coastal structures in shallow water based on measurements of full-scale wave impact pressures on a seawall in West England. The authors reached to the conclusion that the impact pressures measured in the field are generally lower than those measured by scaled experiments due to the high percentage of air trapped between the incident waves and the structure, while Cuomo et al. (2010b) investigated this phenomenon. The authors confirmed that the use of Froude's scaling law may lead to significant over-estimation of impact pressures at prototype scale, and derived correction factors. Kirkgöz (1990, 1991, 1992, 1995) investigated the impact pressures with experiments of regular waves breaking on a vertical wall. He found that the impulsive pressures on the wall can differ significantly for small changes in the water depth. The effect of the trapped air was also studied, highlighting that the pressure can reduce significantly if an air pocket is trapped between the wave and the structure. Marinski and Oumeraci (1993) evaluated modern design guidelines for composite breakwaters with experimental results, reaching to the conclusion that the Goda (1974) method is more conservative than other dynamic approaches. Pedersen and Burcharth (1993) studied the forces and overtopping rates for a rubble mound breakwater with crownwall, developed an overtopping formula and stated that the Jensen (1984) formula can be used as a first estimate for wave loads on rubble mound breakwaters with a crownwall . Allsop et al. (1996) studied the magnitude and probability of occurence of impact loadings on vertical walls reaching to the conclusion that the Goda (1974) method does not describe impact loads well. Allsop et al. (1997) performed an experimental study of impact loadings on vertical and composite breakwaters without a parapet, where an evaluation of existing force prediction methods based on experimental results took place. The effect of wave direction on wave impact was investigated by Allsop and Calabrese (1998). More recently, Chiu et al. (2007) performed an experimental study trying to evaluate the Goda (1974) method. The authors suggest that Goda's wave force theories underestimate the wave forces acting on a caisson for small wave height and overestimate for large wave heights. Cuomo et al. (2010a) proposes a formula for wave impact loads on a vertical breakwater without a crownwall. Valdecantos et al. (2014) evaluates existing methods for prediction of forces on vertical breakwaters with breaking waves. Castellino et al. (2021) performed a numerical study on a recurved parapet by testing numerous exit angles, reaching to the conclusion that a 90^o exit angle for a parapet can increase the loads significantly. The product of this study was an extension of the *Goda* formula that can be used to predict impulsive pressure of a *C-CI* on a recurved parapet for various exit angles and recurve radii. More information on this method is given in Appendix B.3. de Almeida and Hofland (2020b) performed a series of experiments studying the wave impacts caused by standing waves on structures with a short overhang, validating the pressure impulse theory for this case, while the same group of authors study the same type of structure in terms of velocity and trapped air area (de Almeida and Hofland, 2020a).

In the same way, overtopping of vertical walls has been investigated extensively in the past as well e.g.

Besley (1998), while usually modern guidelines refer to EurOtop (van der Meer et al., 2016). Although the methodologies proposed by EurOtop include the effect of a bullnose (Cornett et al., 1999; Kortenhaus et al., 2004; Pearson et al., 2005), the effect of different shapes has not been investigated as much, as parapets is a relatively new design. Some early guidelines can be found in Owen and Steele (1993) for recurved parapets. Kortenhaus et al. (2002), studies the influence of a parapet attached on a vertical wall on top of a steep embankment while later Kortenhaus et al. (2004) performed an extensive study on recurves in which results from various laboratory tests were retrieved, deriving reducing overtopping factors for the use of parapets. Stagonas et al. (2014) during the HYDRALAB IV project, performed an experimental analysis of recurves in breaking wave conditions, investigating overtopping and wave forcing. More recent investigation can be found in Martinelli et al. (2018), who performed an experimental study of a recurved parapet for different exit angles in terms of overtopping and wave forces, where the authors found an underestimation of the overtopping as predicted by EurOtop (van der Meer et al., 2016).

1.2. Scope of the study

There is a very large number of different shapes of crownwalls that have been constructed over the years e.g. bullnoses with different exit angles, curved parapets, crownwalls with a fully curved face. A first classification of vertical breakwater crownwalls mainly distinguishes two categories, see Figure 1.2. As highlighted by EurOtop (van der Meer et al., 2016), the type shown in Figure 1.2a with $B_r > 0$ is characterized by lower overtopping rates with respect to the type shown in Figure 1.2b.

Assuming $B_r > 0$, three shapes can roughly be distinguished for a crownwall, as shown in Figure 1.3. The mentioned literature highlights that while the first two shapes have been applied and studied widely in recent past (Dermentzoglou et al., 2021; Martinelli et al., 2018; Molines et al., 2020), crownwalls with a fully curved face are a very new design and research on the effect of this shape on the performance of the breakwater is very limited. This shape is usually applied for seawalls and not breakwater crownwalls and is commonly found in UK coasts (Penrhyn Bay, Guernsey, Scarborough), usually designed for breaking wave conditions. Examples of this application is shown in Figure 1.4. It is quite interesting though to explore the possibility of applying this type of crownwall in deep water and compare its behavior against wave loading with a typical vertical breakwater.

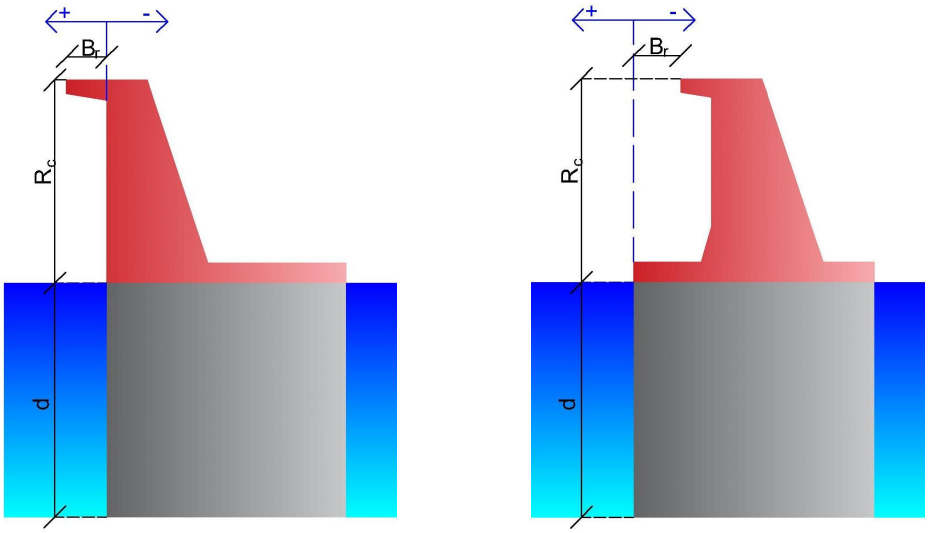

(a) Crownwall vertically aligned with the breakwater.

(b) Crownwall inward shifted with respect to breakwater.

Figure 1.2: Classification of crownwalls based on B_r.

This work explores this potential and its main aim is to study a crownwall with a fully curved face in non-breaking wave conditions and provide tools that can be used to compare its performance with a vertical wall. For this reason, the research question has been formulated as follows:

"How does a crownwall with a fully curved face perform in comparison with a vertical wall, in non–breaking wave conditions and in terms of loading and overtopping?"

Which can further be broken down in two sub-questions.

"What equations can be used to predict overtopping and loading on a crownwall?"

"How can the results from these equations be compared to a vertical wall?"

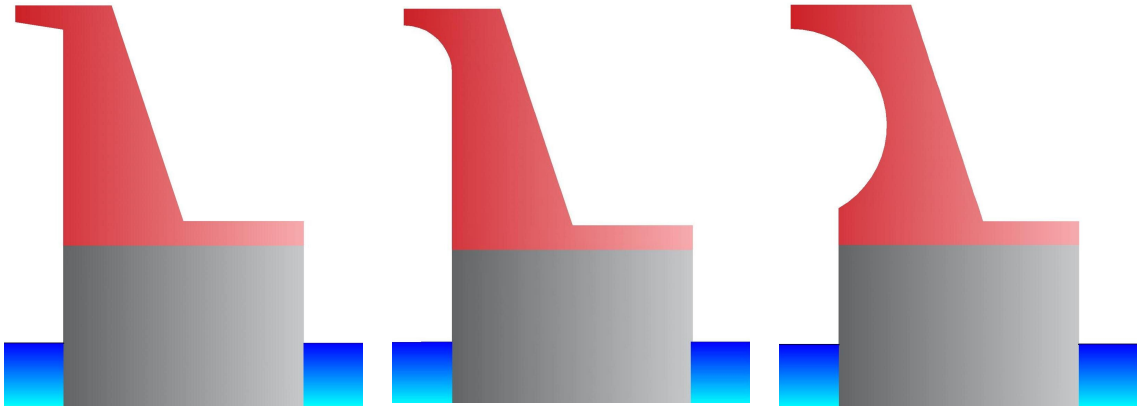

(a) Rectilinear parapet. (b) Recurved parapet. (c) Crownwall with fully curved face.

Figure 1.3: Classification of crownwalls vertically aligned with the breakwater, based on shape.

Figure 1.4: Left panel: Wave return wall located in Penrhyn Bay, Great Britain.Right panel: Recurved seawall at Scarborough. Image taken from Castellino et al. (2019)

In order to give an answer to these questions, small scale experiments of the two structures are carried in a flume with a flat bottom. Regular wave trains are used in the experiments, as single waves are a more fundamental approach that can later help study and understand whole wave spectra. Vertical breakwaters are usually built in intermediate water depths, as deep water depths are usually avoided due to increased costs. Thus, the experiments are performed with intermediate water depth to wave length ratios ($d/L = 0.07 - 0.20$) and a moderate wave steepness ($s = 3 - 4\%$). A flat bottom for the experiments is used in order to avoid shoaling and breaking of the waves. Lastly, in order to carry these experiments, small scale structures that mimic the vertical wall and the crownwall were materially built and provided by *University of L'Aquila* under the original design idea coming from *Sapienza University of Rome*.

In terms of engineering, there are two primary concerns when designing such a structure; its effectiveness against overtopping and the increased load on the superstructure due to the impact. Overtopping is the variable that is most commonly used to define the crest freeboard (R_c). A proper description of the overtopping

performance can be done in terms of discharge over time, $q\,[m^3/s]$ or the individual overtopping volume per wave $V\,[m^3]$. On the contrary, loading on the cross section of the structure has a specific distribution and the load varies at different positions, meaning that more variables are needed to properly describe it. This is further enhanced by the various failure mechanisms of crownwalls, which require the use of different variables to properly describe them. For example, a proper description of the maximum force applied on the crownwall is necessary to design against shear sliding and overturning, while a proper description of the pressure field on the surface of the crownwall is much more useful for designing against structural failure in general. The importance of impacts was already highlighted above, and how they should always be considered, as they may lead to partial or total failure of a crownwall (Allsop and Bruce, 2020a,b; Dermentzoglou et al., 2021; Schoonees, 2014). Impacts are defined as very abrupt changes in the pressure signal, and impulse theory suggests that the area of impacts in the pressure-time diagram (impulses) is much more stable compared to the maximum pressure occuring (Bagnold, 1939). Their study on the other side though requires a very fine time-step, as their time duration is very small, $\mathcal{O} < 0.1\,s$. For these reasons, the studied variables are individual overtopping ($V\,[m^3]$), pressure ($P\,[Pa]$), impulse ($I\,[Pa \times s]$), impulse duration ($t_{imp}\,[s]$), force ($F\,[N]$), force angle ($\theta\,[^\circ]$) and force vertical point of application ($\zeta\,[m]$).

This study is structured as follows. Chapter 2 is a description of the laboratory setup, the performed tests and the post processing methods applied to retrieve wave characteristics, overtopping volumes, maximum pressure, impulse and force variables; Chapter 3 presents the experimental results of the aforementioned variables and their corresponding derived equations; Chapter 4 is a discussion on the findings and the derived equations; lastly, Chapter 5 is a sum up of the results and their applicability range.

2

Tools and Methods

2.1. Description of experiments

2.1.1. Laboratory set-up

The experiments took place at the wave flume of the Hydraulic Engineering Laboratory of Delft University of Technology. The flume is 0.80 *m* wide, 1 *m* tall and 42 *m* long and is equipped with a piston type wavemaker, able to generate regular and irregular waves. The piston-type wave generation system includes second order steering and active reflection compensation (ARC). The bottom of the flume is made of a thick plastic layer, fixed over a metal structure while the sides are made of glass. The setup (Figures 2.1, 2.2) consists of a support structure made of aluminium beams (see Section A.4), on top of which the superstructures are screwed, while a plexiglass front (Figures 2.1 and 2.2, yellow) is fixed on the sea side of the support structure and is aligned with the edge of the crownwall. In order to provide stability to the system, the support structure is mounted on a 1.5 *ton* concrete block (Figures 2.1 and 2.2, grey color), 0.80 *m* wide, 0.80 *m* long and 1.00 *m* high. The front seaside of the structure is positioned 33.33 *m* away from the wave generator.

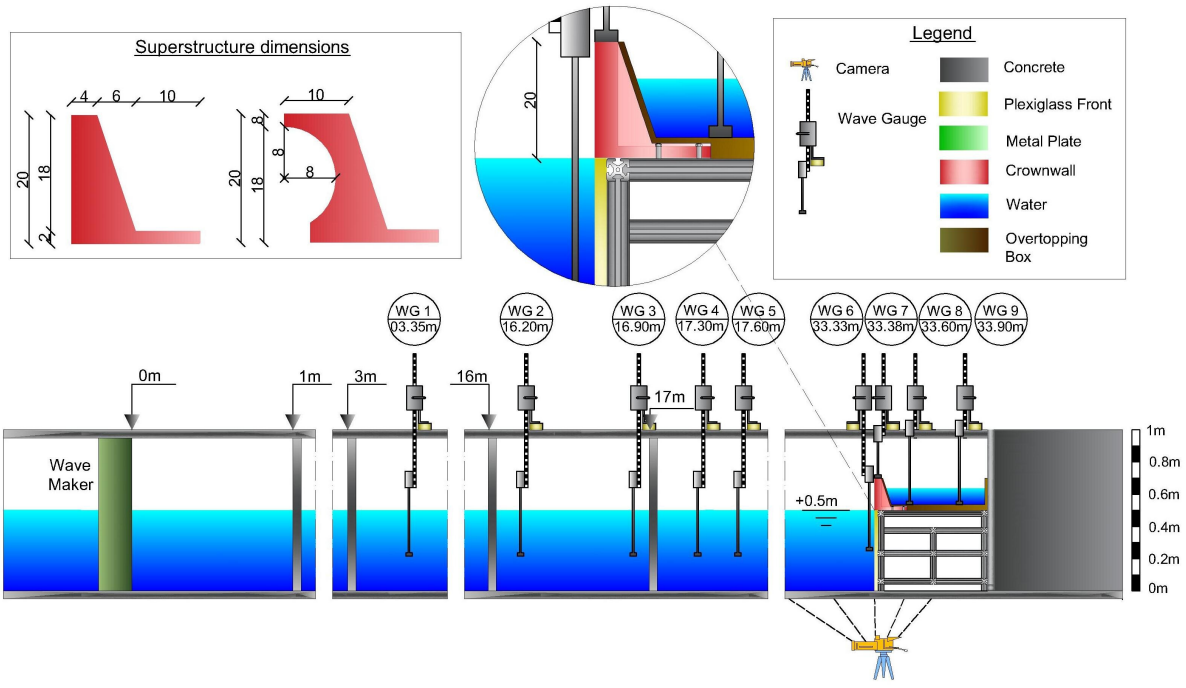

Figure 2.1: Bottom panel: Longitutional cross section of experimental set-up. Top left panel: Dimensions of superstructures. Top middle panel: Zoom of cross section at the position of the crownwall.

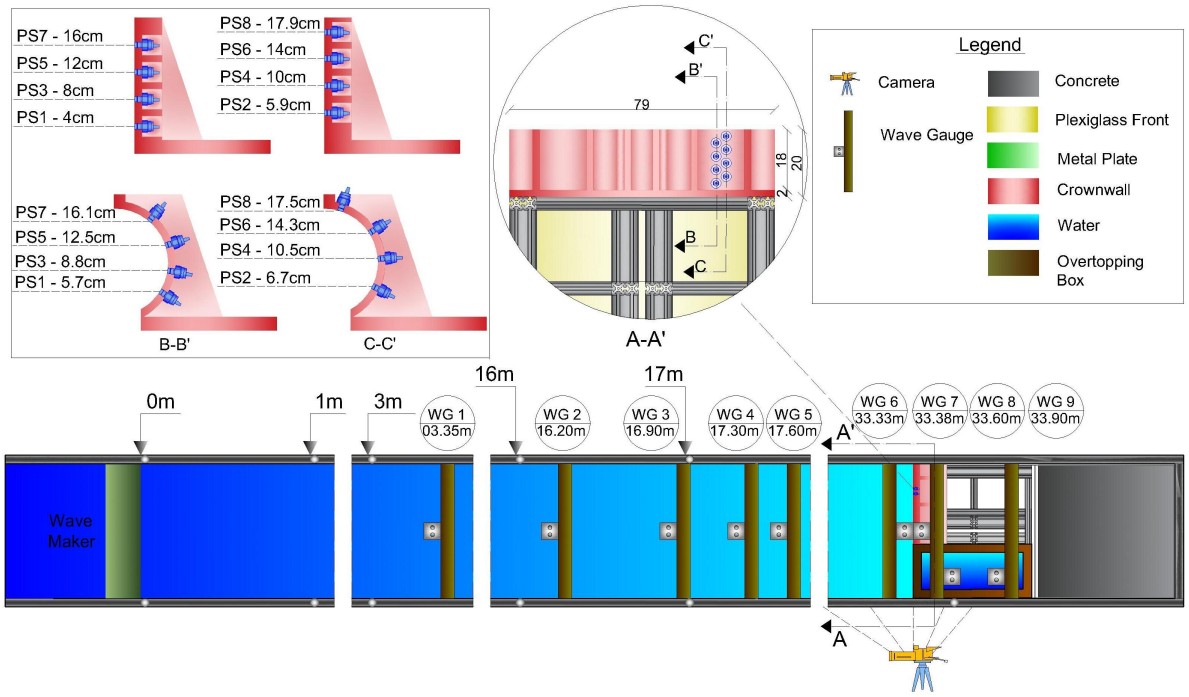

Figure 2.2: Bottom panel: Top view of experimental set-up. Top left panel: positioning of pressure sensors. Top middle panel: Cross section A-A' of *S*1.

Two different superstructures are used during the tests whose cross section is shown in Figure 2.1, a flat crownwall which mimics a standard vertical wall (*S*1), and a crownwall with a fully curved face (*S*2). The crest freeboard R_c is 0.20 m, while the total width of the crownwall setup is 0.795m, barely fitting in the flume. The water depth d for all cases is set to 0.50 m with a horizontal bottom. The gaps created between the crownwalls, the sides of the flume and the vertical front are sealed with silicone and tape.

A total of nine wave gauges (*WG*) are employed, the position of which is shown in Figures 2.1 and 2.2. *WG*1 is used to record water elevation close to the wave generator, *WG2-5* are used to record water elevation in the flume and perform a reflection analysis, *WG*7 is used to identify overtopping events and *WG*8 and *WG*9 are recording water elevation in the overtopping box. The latter, is positioned behind the superstructure (Figure 2.3) and is used to collect overtopping water volumes during the tests. The mouth of the overtopping box is 0.112 m wide while more information about its geometry is provided in Appendix A.3.

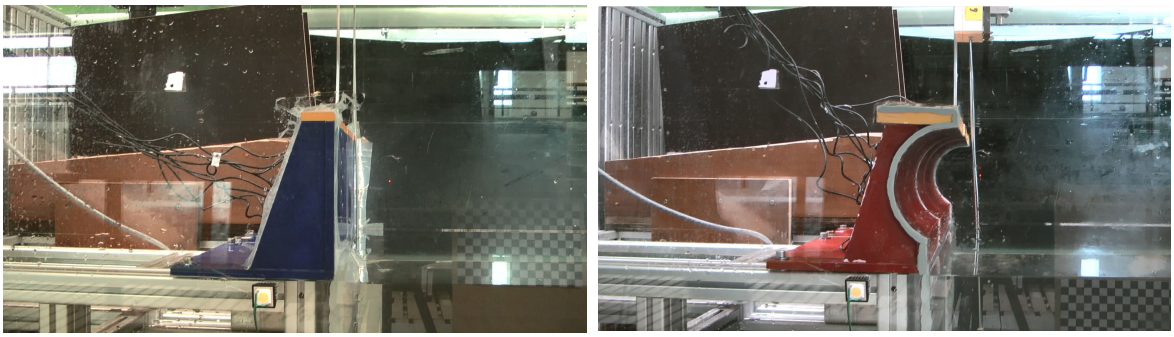

(a) S1, side view of the structure.

(b) S2, side view of the structure

Figure 2.3: Setup of the experiments. *WG*7, the overtopping box and cables of the pressure sensors are visible in both pictures in front and behind of the superstructure.

Eight Kulite HKM-375(M) pressure sensors with a 2 bar measurement range and sealed gauge are used in this study, screwed through metal threads and glued in the superstructures. Similarly to recurves, impacts are expected to occur at the outer seaward edge of the recurve (Martinelli et al., 2018); therefore, the pressure sensors (*PS*) are positioned in a way to cover the widest range of the crownwall face possible. More specifically,

PS1 and *PS8* are positioned, within the limitations of the geometry of the superstructures, at the lowest and highest possible points respectively. They are placed with an interval of approximately 2 cm between them, while their exact position relative to SWL is shown in Figure 2.2, top left panel.

Lastly, the sampling frequency for all instruments is $f_s = 2\,kHz$. Instrument calibration functions before and after the execution of the experiments showed a variation of approximately 1%, which is considered acceptable in this study. More information about the selection of instruments is found in Appendix A.1, about the calibration of instruments in Appendix A.2 and the selection of the positioning of the wave gauges in Appendix B.2.

2.1.2. Test description

A summary of the performed tests and their target wave characteristics is presented in Table 2.1. Both shapes are tested for regular wave trains of 20 waves and 3 different target values of wave steepness (s), $s = 4\%$, $s = 3.5\%$ and $s = 3\%$. For each of the 3 values of wave steepness, 7 different wave heights (H) are applied ranging from $0.10m$ to $0.22m$, resulting in a total of 21 different regular wave states. All the tests are performed in intermediate waters with a ratio of water depth to wave length $0.07 \leq d/L \leq 0.20$.

Table 2.1: Test ID and target values of wave height (H), wave period (T), wave length(L), wave steepness (s), water depth to wave length ratio (d/L) and Ursell number (U) of regular wave tests.

ID	$H[m]$	$T[s]$	$L[m]$	$s[-]$	$d/L[-]$	$U[-]$
R11	0.10	1.37	2.50	4.0%	0.20	5.00
R12	0.12	1.57	3.00	4.0%	0.17	8.60
R13	0.14	1.77	3.50	4.0%	0.14	13.72
R14	0.16	1.98	4.00	4.0%	0.13	20.48
R15	0.18	2.19	4.50	4.0%	0.11	29.16
R16	0.20	2.40	5.00	4.0%	0.10	40.00
R17	0.22	2.61	5.50	4.0%	0.09	53.24
R21	0.10	1.90	2.86	3.5%	0.18	6.53
R22	0.12	2.00	3.43	3.5%	0.15	11.28
R23	0.14	2.10	4.00	3.5%	0.13	17.92
R24	0.16	2.20	4.57	3.5%	0.11	26.75
R25	0.18	2.30	5.14	3.5%	0.10	38.08
R26	0.20	2.40	5.71	3.5%	0.09	52.24
R27	0.22	2.95	6.29	3.5%	0.08	69.54
R31	0.10	2.00	3.33	3.0%	0.15	8.88
R32	0.12	2.15	4.00	3.0%	0.13	15.36
R33	0.14	2.25	4.67	3.0%	0.11	24.39
R34	0.16	2.40	5.33	3.0%	0.09	36.41
R35	0.18	2.50	6.00	3.0%	0.08	51.84
R36	0.20	2.60	6.67	3.0%	0.08	71.11
R37	0.22	2.70	7.33	3.0%	0.07	94.65

2.2. Post-processing

2.2.1. Wave characteristics

This subsection presents the analyses performed in order to retrieve the wave characteristics and reflection coefficients. Firstly, the signals of *WG2-5* are used to perform a reflection analysis with the method proposed by Zelt and Skjelbreia (1993), and retrieve the incident (η_{in}) and reflected (η_{ref}) water elevation signals. More information on this method is provided in Appendix B.2.

The two signals are retrieved 3 m away from the structure, which creates a time lag between them. Figure 2.4 presents the methodology followed in order to remove it. The initial signal (Figure 2.4, top left panel) is split into two components (Figure 2.4, top right panel) following the method of Zelt and Skjelbreia (1993). The time lag between the two signals is removed by shifting η_{ref} (Figure 2.4, top right panel) by time intervals of $1/f_s = 1/2000 = 5 \times 10^{-4}\,s$ and calculating the normalized cross correlation for each time shift (Figure 2.4, bottom left panel). The time lag is defined as the time shift with the maximum cross correlation and η_{ref} is shifted accordingly. The resulting aligned η_{in} and η_{ref} are shown in the bottom right panel of Figure 2.4.

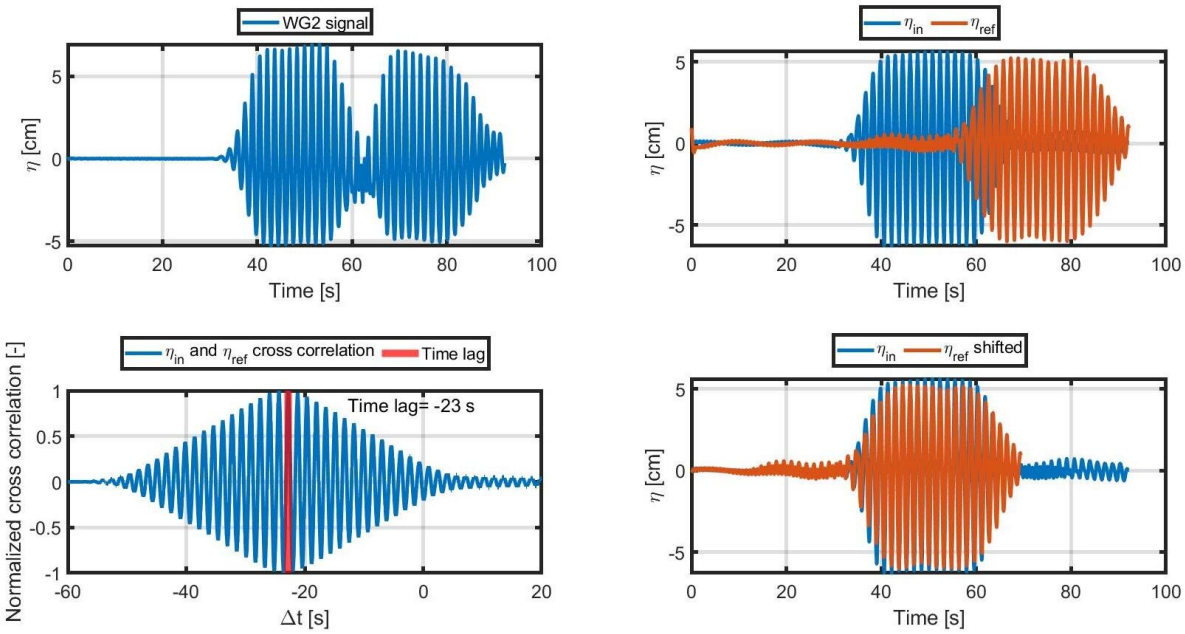

Figure 2.4: Methodology for removing time lag. Top left panel: $WG2$ signal; Top right panel: Results of reflection analysis; Bottom left panel: Cross correlation function; Bottom right panel: Aligned signals.

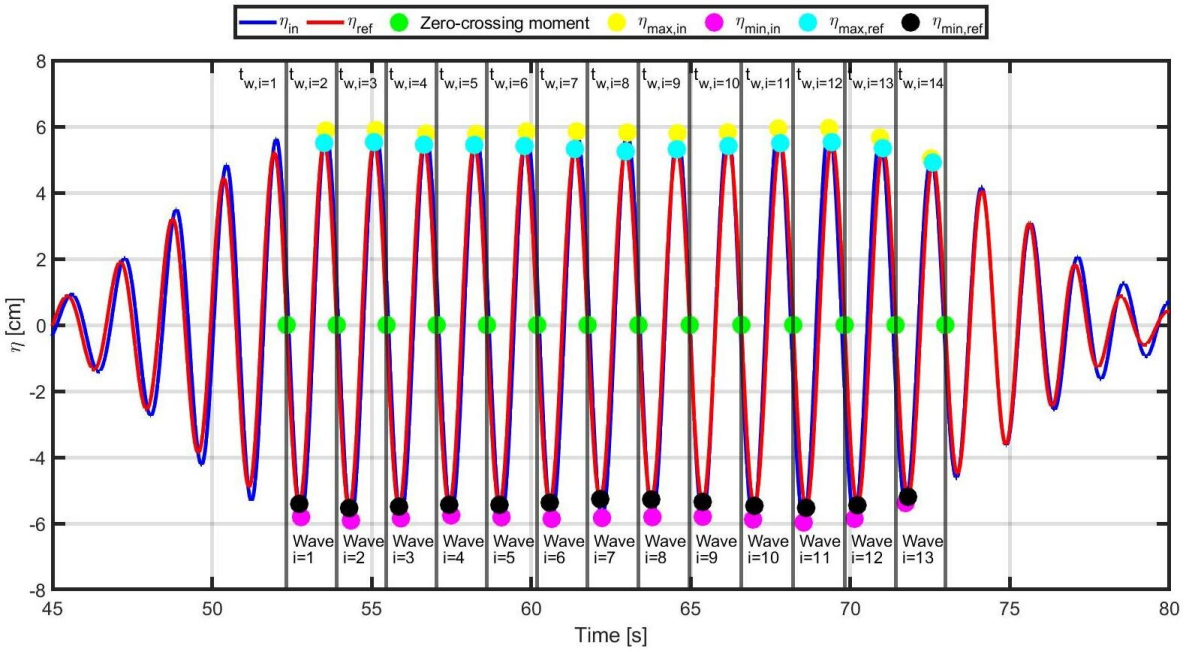

Figure 2.5: Zero-down crossing analysis. Incident η_{in} and reflected η_{ref} water elevation signals are shown as blue and red lines; green dots are the zero-down crossing moments of the selected waves; maximum and minimum values of η_{in} for each time interval are shown as yellow and purple dots; maximum and minimum values of η_{ref} for each time interval are shown as cyan and black dots.

The aligned incident and reflected signals are used in a zero-down crossing analysis, as demonstrated in Figure 2.5. The zero-down crossing moments are identified (Figure 2.5, green dots) for η_{in}, at which the initiation of each wave event $t_{w,i}$ is defined. In other words, the time domain is divided in time intervals $t_{w,i} - t_{w,i+1}$ which show the beginning and ending of the wave event i. Hereinafter, the index i refers to *wave event i* and is used to highlight that a variable is referring to individual waves. The indexes $S1$ and $S2$ are also used in order to distinguish between the vertical wall and the crownwall with a fully curved face.

The incident wave period $T_{in,i}$ is calculated as the difference $t_{w,i+1} - t_{w,i}$ for each wave event. While

the incident wave height $H_{in,i}$ as the difference of the maximum (Figure 2.5, yellow dots) and minimum (Figure 2.5, black dots) value of η_{in} for the time interval $t_{w,i} - t_{w,i+1}$. A similar time domain is created for η_{ref} and the according wave characteristics $H_{ref,i}$ and $T_{ref,i}$ of single wave events are calculated in the same way. Wave length $L_{in,i}$ is calculated through $T_{in,i}$ and by using the linear dispersion relationship.

An example result of a zero-down crossing analysis is shown in Figure 2.6. The wave paddle needs an approximate 5 waves to steer up and reach the target wave height (Figure 2.6, top left panel) and an approximate 5 to steer down; notice the gradually increasing and decreasing values of H_{in}. In addition, experiments *R16*, *R26*, *R36* result in light breaking of some individual waves, while experiments *R17*, *R27* and *R37* result in total breaking of most waves. Wave breaking occurs for all experiments right after their generation and before $WG1$. In order to overcome these issues, breaking, steer-up and steer-down waves are excluded from the results by taking into account waves whose wave height is larger than 90% of the experiment's target wave height H (Table 2.1). This is the reason the time domain in Figure 2.5 is divided only for the higher waves of the record, as lower peaks before $t_{w,i=1}$ and after $t_{w,i=14}$ are much smaller. The results regarding *R17*, *R27* and *R37* are completely excluded from this study.

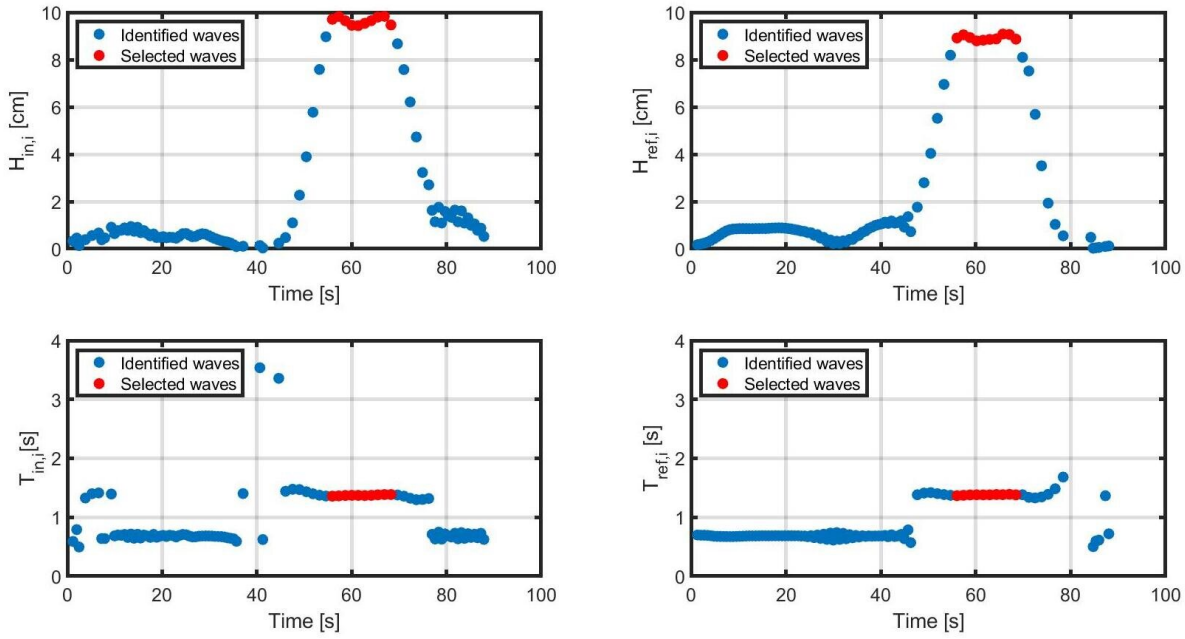

Figure 2.6: Results of zero down analysis of $R12$ and $S1$. Top left panel: Incident wave height $H_{in,i}$. Bottom left panel: Incident wave period $T_{in,i}$. Top right panel: Reflected wave height $H_{ref,i}$. Bottom right panel: Reflected wave period $T_{ref,i}$. Selected waves are highlighted in red.

Finally, a reflection coefficient is calculated for each single wave event, as the fraction between the reflected and incident wave height, $K_{r,i} = \frac{H_{ref,i}}{H_{in,i}}$, while the total reflection coefficient K_r per wave state is calculated as the mean value of the corresponding $K_{r,i}$.

2.2.2. Overtopping

Individual overtopping volumes (V_i) are determined by making use of the signal from *WG9* (Figure 2.7, black line). The time domain is divided similarly as described in Subsection 2.2.1. For each time interval $t_{w,i} - t_{w,i+1}$, an overtopping event (Figure 2.7, red dots, denoted as OE_i) is identified when the $WG7$ signal (Figure 2.7,blue line) has an abrupt change, while time intervals with no change are automatically assigned a zero overtopping volume. A moving median is applied on $WG9$ signal (Figure 2.7, black line) to remove noise, which results in a modified signal with distinguishable steps(Figure 2.7, brown line). These steps correspond to the overtopping volumes V_i of OE_i, and are identified automatically at the point of maximum derivative of the smoothed signal. The identified points are highlighted in green, and the individual overtopping volume (V_i) for each wave event is calculated as the difference between the two subsequent identified steps in the $WG9$ signal.

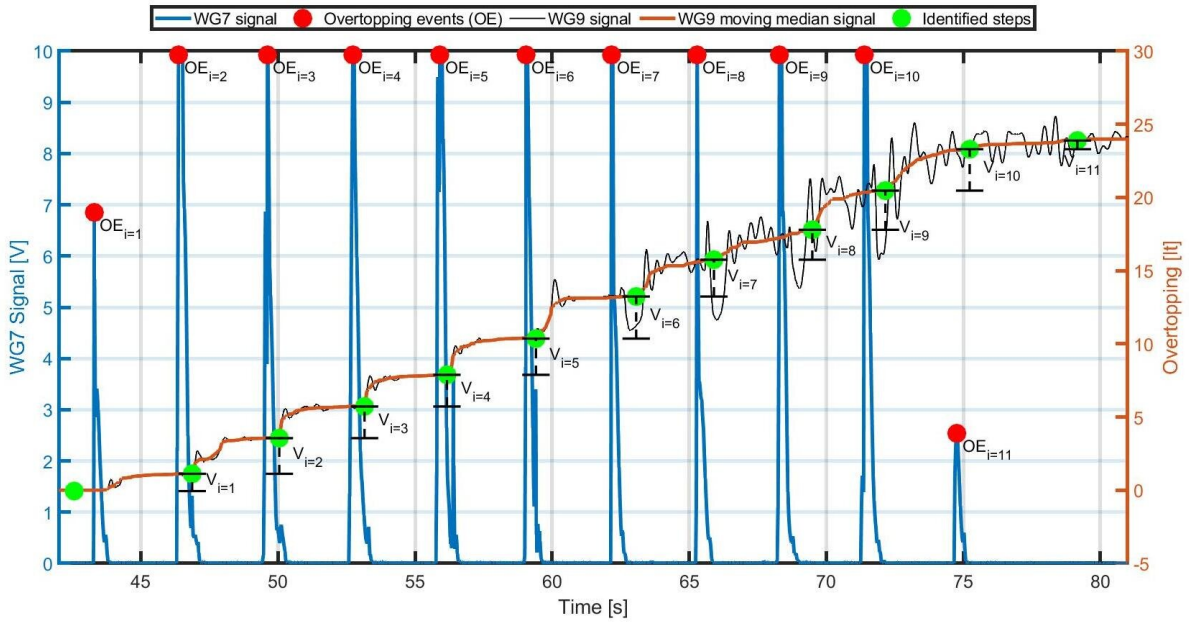

Figure 2.7: Determination of overtopping volumes for experiment $R36$ and $S1$. Blue line is $WG7$ signal; red dots are the identified overtopping events (OE_i); black line is the original $WG9$ signal; brown line is the $WG9$ signal filtered with a moving median; green dots are the identified steps in the signal. The difference between two subsequent steps results equals to the overtopping volume V_i.

2.2.3. Pressure and impacts

The main goal of this analysis is the calculation of maximum pressure ($P_{i,j}$), impulse ($I_{i,j}$) and duration of impulse ($t_{imp,i}$) of single wave events from the pressure signal. As the signal from 8 different pressure sensors is used, the index j is used to distinguish between them in addition to the already introduced indexes. For example, $P_{i=3,j=7}$ refers to the pressure signal of the 3^{rd} of the selected waves (Figure 2.5) from $PS7$.

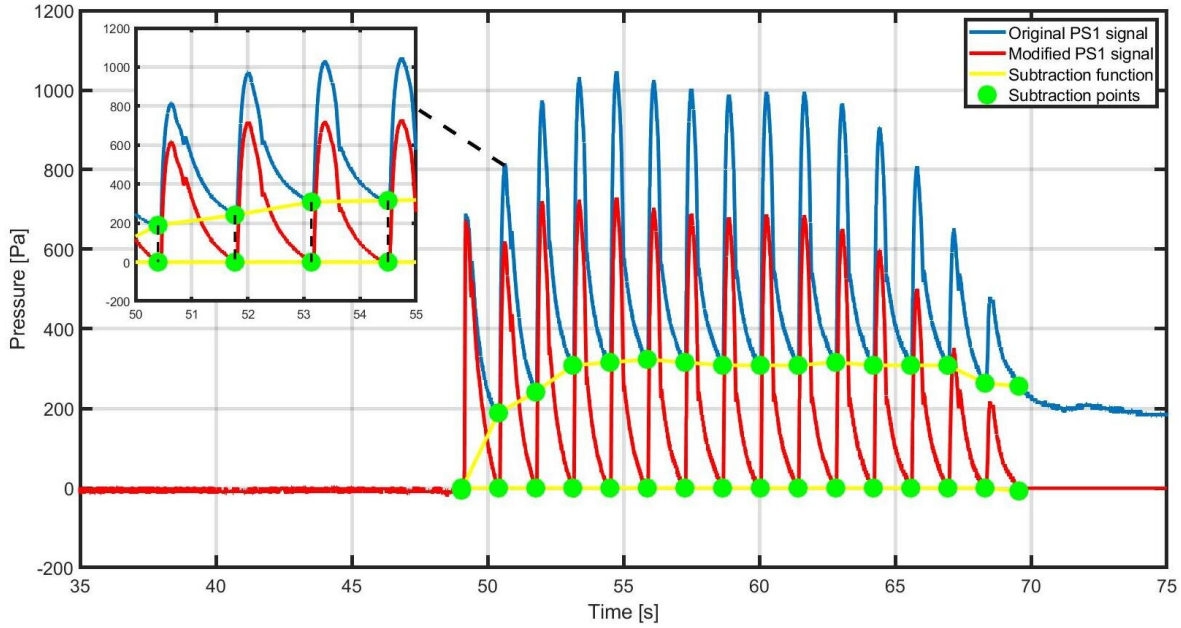

Figure 2.8: Removal of thermal expansion from pressure signal for experiment R12 and PS1.

One of the issues encountered during this analysis is the thermal shock of pressure sensors. In order to address it, the time domain is divided similarly as described in Subsection 2.2.1 and each wave is treated seperately. For each time interval $t_{w,i} - t_{w,i+1}$, the minimum value of the pressure signal is determined (Figure 2.8, green dots). These points are connected to create a function (Figure 2.8, yellow line) that is subtracted

from the PS signal (Figure 2.8, blue line). Obviously, cases without thermal expansion result in a subtraction line $y = 0$, having no effect on the signal. Thermal shock happens randomly, mostly for $S1$ and for around 25% of the total experiments. Waves for which thermal shock is removed are also checked from the camera videos to ensure there is no water on the pressure sensor at the moment of local minimum pressure (Figure 2.8, green dots). Further references to "pressure signal" below refer to this modified signal (Figure 2.8, red line).

It was firstly observed experimentally by Bagnold (1939) that peak impulsive pressures exhibit a large variation. Although these variations were partially induced by scaled effects during his experiments, the nature of impacts is also quite variable, as identical waves can give variable impacts (Bagnold, 1939; Hofland et al., 2010; Losada et al., 1995). On the other hand, it has been observed that although the shape of an impulse might show a great variance, the integral of the impulsive load in the pressure time diagram is very stable and predictable (Cooker and Peregrine, 1991; Cuomo et al., 2010b; Hofland et al., 2010). In addition, although most structural methods make use of the maximum forcing, recent research (Chen et al., 2019) highlights the possibility of using impulses to calculate reaction forces. As a consequence of the above, the determination of impulses is considered necessary for this study.

Indeed, for all wave events for which an impulsive load occurs, not only the shape and intensity varies for identical waves, but for the different pressure sensors as well. The impulse on the other hand is considerably more stable, which is shown below in Subsection 3.3.2.

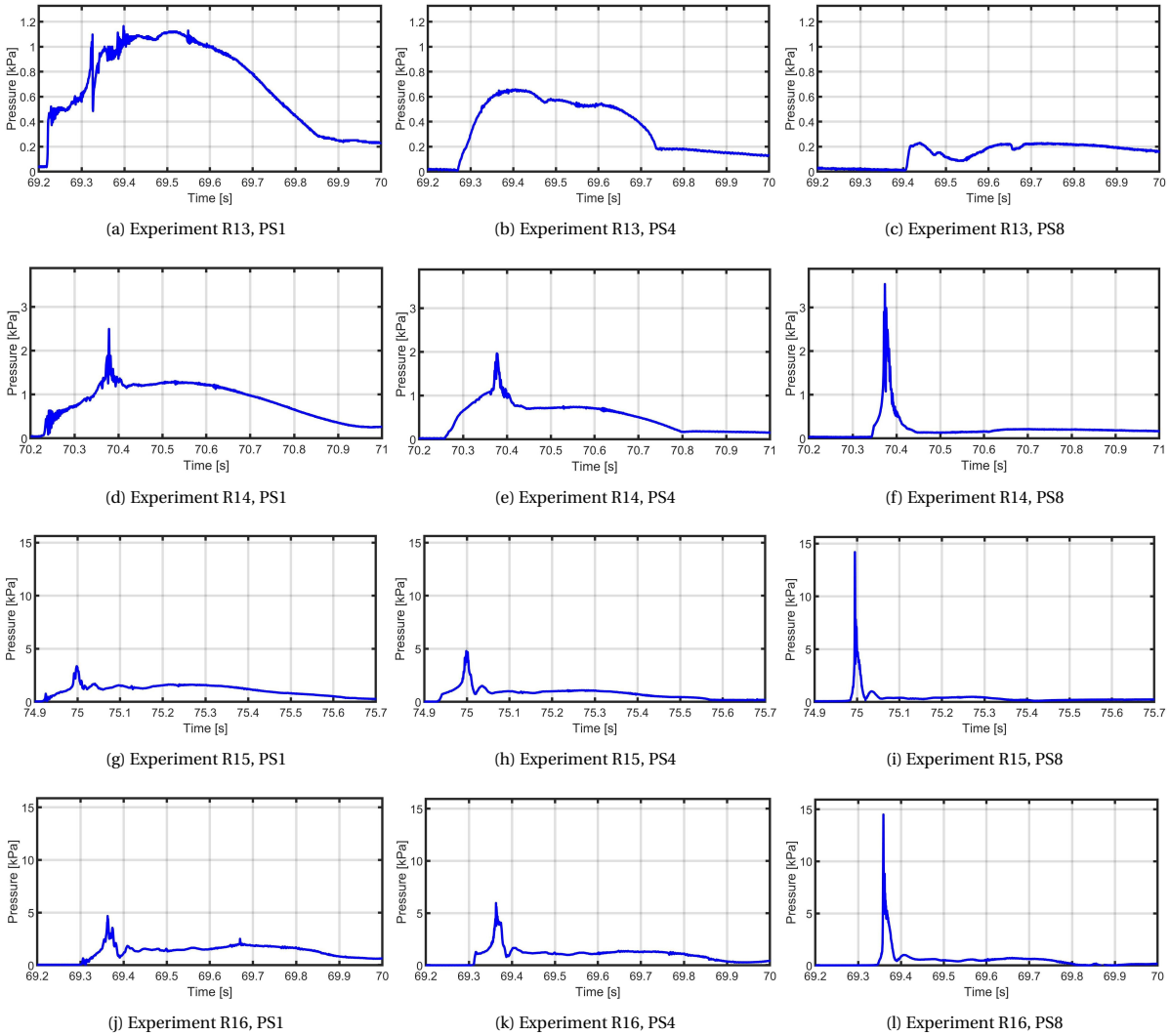

(a) Experiment R13, PS1 (b) Experiment R13, PS4 (c) Experiment R13, PS8

(d) Experiment R14, PS1 (e) Experiment R14, PS4 (f) Experiment R14, PS8

(g) Experiment R15, PS1 (h) Experiment R15, PS4 (i) Experiment R15, PS8

(j) Experiment R16, PS1 (k) Experiment R16, PS4 (l) Experiment R16, PS8

Figure 2.9: Plot of maximum $P_{i,j}$ for $S2$, wave states $R13$, $R14$, $R15$ and $R16$ and $PS1$, $PS4$ and $PS8$

Figure 2.9 presents the pressure signal of $S2$ during the wave event with maximum pressure, for experiments $R13$, $R14$, $R15$ and $R16$ and for $PS1$, $PS4$ and $PS8$. It is quite obvious that for $R13$ the water column

barely reaches $PS8$ (Figure 2.9c) and creates a small perturbation in the signal. This though cannot be considered an impulsive load, as the water column does not fill the area below the recurve completely. This perturbation is also detected by $PS1$ (Figure 2.9a) as a small peak during the uprising of pressure, while it is not recorded by $PS4$ (Figure 2.9b). In general, a lot of these waves create a large uncertainty in the results. For this reason the experiments that are considered in the results regarding the impulsive load are $R14-R16$, $R23-R26$ and $R33-R36$, which are the cases the area below the recurve fills up and a distinguishable impulsive peak occurs in the pressure signal.

It is also notable that for the experiments for which impacts are identified, there is a considerable time lag of the impulse between different sensors. For example, at $PS8$ (Figure 2.9f) the impulse happens instantaneously while at $PS1$ (e.g. Figure 2.9d) there is a smoother rise first. This is a result of the fact that the impact occurs at the outer edge of the recurve. $PS1$ receives a quasi-static load at the moment a wave reaches the recurve; the load slowly rises until the water column reaches the outer edge of the recurve. Then, a violent rise of the pressure signal occurs instantaneously at all pressure sensors as a result of the impact.

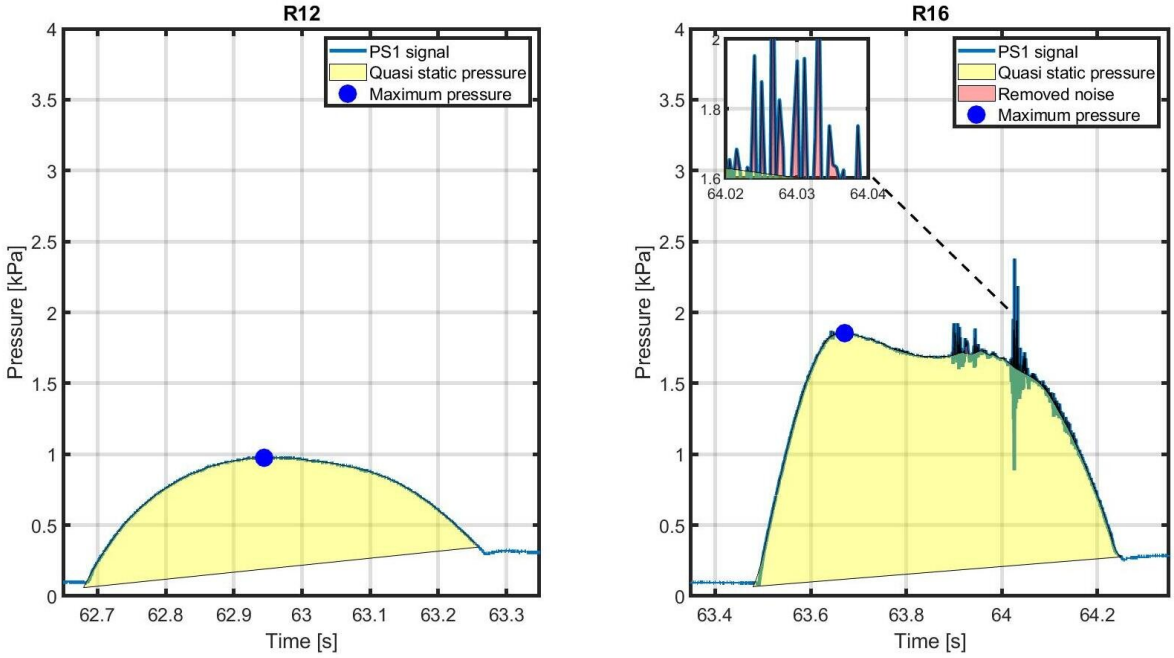

Figure 2.10: Left panel: Calculation of maximum pressure $P_{i,j}$ for experiment $R12$ and $PS1$. Right panel: Calculation of maximum pressure $P_{i,j}$ for experiment $R16$ and $PS1$.

In addition, it may be noticed that for higher wave heights (e.g.Figure 2.9j- Figure 2.9l) the impulse gets shorter and its shape changes as lower peaks appear after the first highest peak. This variety in shape between experiments and sensors create the demand for a homogeneous way of calculating the impulse and its time duration. In order to address these issues, the impulse duration for each wave event $t_{imp,i}$ is defined only at $PS8$, while it is assumed the same for the rest of the pressure sensors. Consequently, the variables that are considered for $S2$ are the maximum pressure $P_{i,j}$ and impulse $I_{i,j}$ per wave per sensor, and the impulse duration $t_{imp,i}$ only for the signal of $PS8$. While for $S1$ no impulsive loading occurs and only $P_{i,j}$ is considered.

The procedure showing the retrieving of pressure for $S1$ is demonstrated in Figure 2.10. Each wave is treated separately, by splitting up the signal according to the $t_{w,i} - t_{w,i+1}$ intervals. During experiments with highest wave heights (e.g. $R16$, $R26$, $R36$), large water volumes overtop the crownwalls, hit the back of the sensors and create noise in the signal (Figure 2.10, right panel). As a result, experiments with low wave heights like $R12$ (Figure 2.10, left panel)) and no overtopping result in a quasi static shape with no noise, while experiments like $R16$ result in high frequency noise near the downfall of the quasi static pressure (Figure 2.10, right panel). In order to remove this noise, the function *smooth* along with the method *rloess* are employed in *Matlab 2020a*. This is a function which performs a local regression using linear least squares and a 2^{nd} degree polynomial model, while assigning lower weights to outliers. More information on this method is provided in Appendix B.4. The maximum pressure for the wave event $P_{i,j}$ is calculated as the maximum of the smoothed

signal in the time interval $t_{w,i} - t_{w,i+1}$ (Figure 2.10).

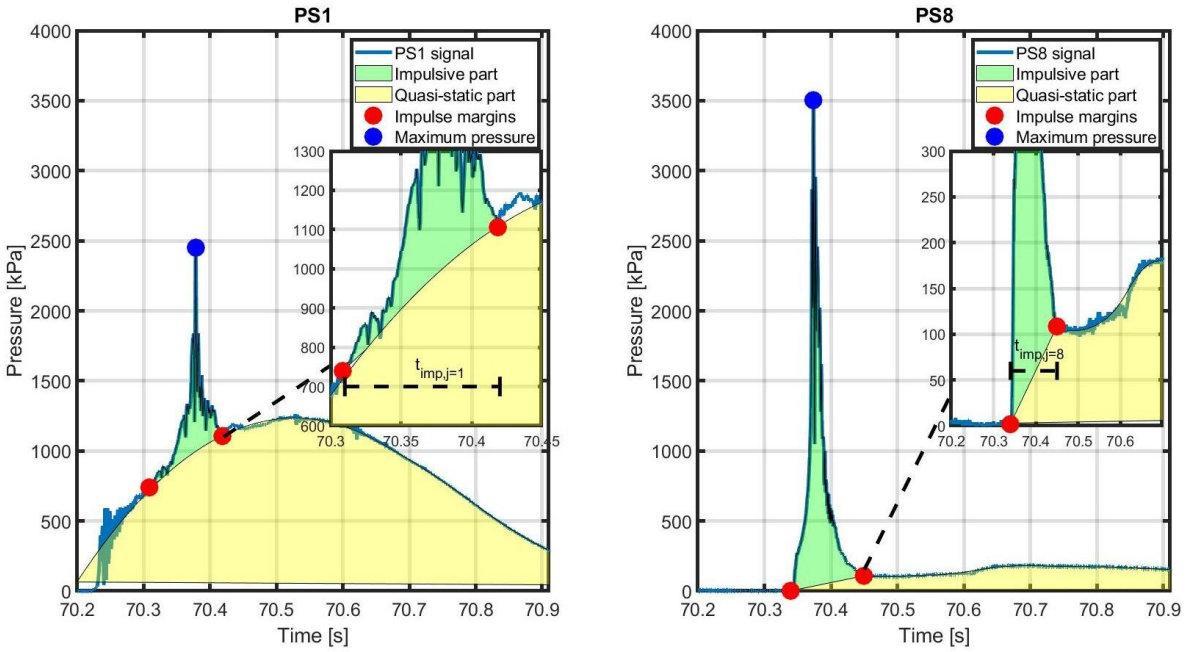

Figure 2.11: Definition of maximum pressure $P_{i,j}$, impulse $I_{i,j}$ and impulse duration $t_{imp,i}$. Left panel: Experiment $R14$ and $PS1$. Right panel: Experiment $R14$ and $PS8$.

The procedure showing the retrieving of data from the pressure signals for $S2$ is presented in Figure 2.11. The time domain is divided by using the time intervals $t_{w,i} - t_{w,i+1}$ as described in Subsection 2.2.1. For each individual wave event, the maximum pressure per wave per sensor $P_{i,j}$ is calculated as the maximum value of the corresponding pressure signal (Figure 2.11, blue dots). The quasi-static pressure (Figure 2.11, yellow) is approximated by applying the same *smooth* function as described in the case of $S1$.

As already mentioned, the duration of the impulse is defined at $PS8$. For that PS, the beginning of the impulse is defined as the first point of the time interval $t_{w,i} - t_{w,i+1}$ with a pressure larger than zero (Figure 2.11, right panel, $t \approx 70.35s$). While the end of the impulse is defined manually and graphically as the first point after the peak with a value lower than the approximated quasi-static pressure (Figure 2.11, right panel, $t \approx 70.45\ s$). The two points are connected with a straight line, defining the impulse (Figure 2.11, green). The impulse duration ($t_{imp,i}$) per wave is defined as the difference on the x axis between these two points. In this case for example, $t_{imp,i} \approx 70.45 - 70.35 = 0.1\ s$.

For lower sensors (e.g. Figure 2.11, left panel), the ending moment of the impulse is defined at the point after the peak pressure when the pressure signal becomes lower than the quasi-static pressure (Figure 2.11, left panel, $t \approx 70.42\ s$). The beginning of the impulse is calculated by subtracting $t_{imp,i}$ from the ending moment of the impulse (Figure 2.11, left panel, $t \approx 70.42 - 0.1 = 70.32\ s$).

The impulse $I_{i,j}$ is approximated for all sensors by connecting the starting and ending points with a straight line and subtracting any possible overlapping parts with the quasi-static pressure. The core idea of this method stems from (de Almeida and Hofland, 2020a) and has the advantage of offering a homogeneous way of analyzing signals from different pressure sensors.

2.2.4. Wave forces

Forces can be very useful as they can serve as a first estimate to calculate the stability of a crownwall against typical failures e.g. shear sliding and overturning. In this study, wave forces (F), their angle of application relative to the ground (θ) and their point of application in the vertical direction (ζ) are also calculated by integrating the pressure signal on the surface of the crownwall.

The front faces of $S1$ and $S2$ are divided in eight areas for each of the pressure sensors, as shown in Figure 2.12, left panel. The different areas are distinguished by switching color between white and black and the margins between adjacent pressure sensors are set in the middle of their distance. The length of the cross section of each area (A_j) is given in Table A.5.

S2 has two additional areas for which data is not available, which are the bottom (Figure 2.12, named *EX0*) and top flat face areas. A pressure signal for the centre point of the bottom flat part ($EX0$) is approximated by performing a linear extrapolation and using the pressure signals from $PS1$ and $PS2$, while the top part is considered irrelevant to the loading of the structure. Hereinafter, the pressure signal of the area *EX0* is denoted with the index $j = 0$.

Five signals, F_{tot}, F_x, F_z, θ and ζ, referring to total force, force in the the x and y directions, angle of application of the force relative to the ground and point of application of F_x relative to still water level (*SWL*) respectively, are composed by making use of the pressure signals $P_{j=0}$-$P_{j=8}$ as shown in Equations 2.2-2.5. The definition of these variables is shown in Figure 2.12.

$$F_x = \sum_{j=0}^{j=8} P_j A_j cos(\phi_j) \tag{2.1}$$

$$F_z = \sum_{j=0}^{j=8} P_j A_j sin(\phi_j) \tag{2.2}$$

$$F_{tot} = \sqrt{F_x^2 + F_z^2} \tag{2.3}$$

$$\theta = \frac{F_z}{F_x} \tag{2.4}$$

$$\zeta = \frac{\sum_{j=0}^{j=8} P_j z_j cos(\phi_j)}{\sum_{j=0}^{j=8} P_j cos(\phi_j)} \tag{2.5}$$

Where A_j is the length of the cross section of each area attributed to pressure sensor j, and z_j is the distance of pressure sensor j from *SWL*, (Figure 2.12, shown for $PS4$). The angle ϕ is the orientation of each pressure sensor relative to the ground and is used to decompose the total force to its tangential components (Equations 2.2, 2.3). Its values for each pressure sensor are given in Table A.5.

Similarly as above, the F_{tot} signal is split up according to the $t_{w,i} - t_{w,i+1}$ time intervals. The maximum total force of individual waves $F_{tot,i}$ is calculated for each time interval, while $F_{x,i}$, $F_{z,i}$, θ_i and ζ_i are identified as the values of these signals at the moment maximum $F_{tot,i}$ occurs.

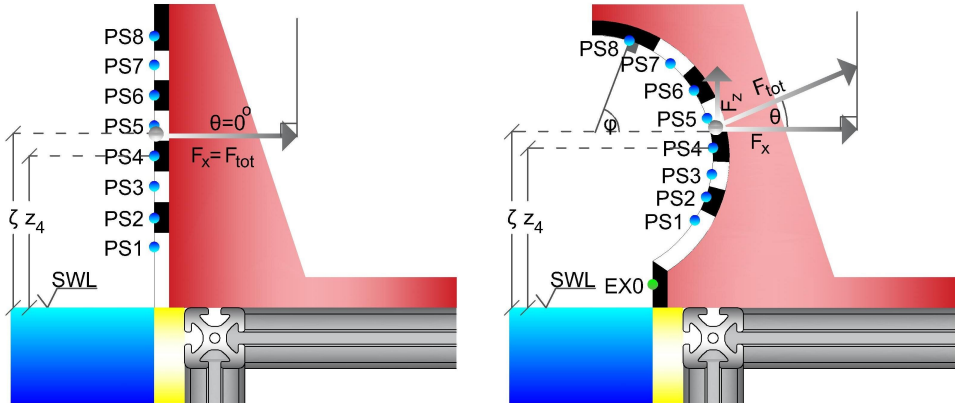

Figure 2.12: Integration areas of pressure sensors and definition of F_x, F_z, F_{tot}, θ, ϕ and ζ. Left panel: Vertical wall. Right panel: Crownwall with a fully curved face.

3

Results

3.1. Wave characteristics

This section presents the results regarding the wave characteristics of incident and reflected waves. The mean values of incoming wave characteristics H, L, T and dimensionless numbers d/L, U and K_r are given in Tables 3.1 and 3.2 for $S1$ and $S2$ respectively. The measured generated wave height is very similar to the target wave height (Table 2.1), as for all experiments the deviation between them is $0-6\%$, while only for experiment $R21$ the mean wave height is 10% smaller than the target value. The period (T) of the generated waves is also very similar to the target value, as the largest deviation occurs for $R16$ and $S1$ with a value of 1.5%.

Table 3.1: Mean values of wave height (H), wave period (T), wave length (L), wave steepness (s), water depth to wave length ratio (d/L), *Ursell* number (U) and reflection coefficient (K_r) for $S1$.

Wave state	$H\,[cm]$	$T\,[s]$	$L\,[m]$	$s\,[\%]$	$d/L\,[-]$	$U\,[-]$	$K_r\,[-]$
$R11$	9.44	1.37	2.50	3.77	0.20	4.73	0.93
$R12$	11.42	1.57	3.01	3.80	0.17	8.26	0.92
$R13$	13.92	1.78	3.53	3.95	0.14	13.84	0.94
$R14$	17.00	1.99	4.03	4.22	0.12	22.12	0.94
$R15$	18.85	2.20	4.54	4.16	0.11	31.04	0.92
$R16$	20.10	2.44	5.10	3.94	0.10	41.82	0.86
$R21$	9.45	1.52	2.88	3.28	0.17	6.26	0.93
$R22$	11.63	1.73	3.40	3.42	0.15	10.77	0.93
$R23$	14.71	1.99	4.04	3.65	0.12	19.16	0.91
$R24$	16.36	2.23	4.61	3.55	0.11	27.77	0.95
$R25$	18.86	2.48	5.20	3.63	0.10	40.75	0.87
$R26$	19.79	2.71	5.73	3.45	0.09	52.03	0.83
$R31$	9.75	1.70	3.33	2.93	0.15	8.64	0.94
$R32$	12.30	1.98	4.01	3.07	0.12	15.82	0.94
$R33$	14.08	2.25	4.65	3.03	0.11	24.39	0.94
$R34$	16.34	2.55	5.36	3.05	0.09	37.57	0.94
$R35$	17.56	2.85	6.05	2.90	0.08	51.47	0.87
$R36$	19.53	3.24	6.71	2.91	0.07	70.34	0.85

Figure 3.1 shows the mean values of the reflection coefficient (K_r) per wave state against the dimensionless freeboard (R_c/H). Experiments with $R_c/H > 1.20$ (Figure 3.1, light hues) have a constant value of K_r for both shapes, and the mean value is calculated as $K_{r,S1} = 0.94$ and $K_{r,S2} = 0.92$. The deviation from the ideal $K_r = 1$ is addressed to friction energy loss between the water column and the crownwalls. The fact that $K_{r,S2} < K_{r,S1}$ is addressed to the fact that $S2$ has a longer contact surface, and thus more energy loss occurs for its case.

For roughly $R_c/H < 1.20$ the values of K_r start to drop, which is attributed to large overtopping volumes. For higher wave heights, large overtopping masses cause energy loss leading to much lower energy content in the reflected wave and eventually lower K_r values.

Table 3.2: Mean values of wave height (H), wave period (T), wave length (L), wave steepness (s), water depth to wave length ratio (d/L), *Ursell* number (U) and reflection coefficient (K_r) for $S2$.

Wave state	$H\,[cm]$	$T\,[s]$	$L\,[m]$	$s\,[\%]$	$d/L\,[-]$	$U\,[-]$	$K_r\,[-]$
$R11$	9.52	1.37	2.49	3.82	0.20	4.74	0.92
$R12$	11.48	1.57	3.00	3.82	0.17	8.28	0.92
$R13$	13.74	1.78	3.53	3.90	0.14	13.67	0.95
$R14$	16.8	1.99	4.04	4.16	0.12	21.89	0.95
$R15$	18.37	2.19	4.51	4.07	0.11	29.90	0.89
$R16$	20.21	2.43	5.08	3.98	0.10	41.71	0.77
$R21$	9.01	1.51	2.85	3.16	0.18	5.87	0.93
$R22$	11.63	1.75	3.45	3.37	0.14	11.08	0.92
$R23$	14.44	1.98	4.01	3.60	0.12	18.57	0.93
$R24$	16.26	2.22	4.58	3.55	0.11	27.32	0.92
$R25$	18.79	2.48	5.20	3.62	0.10	40.60	0.85
$R26$	20.12	2.7	5.71	3.53	0.09	52.42	0.77
$R31$	9.36	1.7	3.33	2.81	0.15	8.26	0.93
$R32$	11.95	1.98	4.01	2.98	0.12	15.37	0.95
$R33$	13.72	2.26	4.68	2.93	0.11	24.02	0.94
$R34$	16.07	2.55	5.36	3.00	0.09	36.95	0.93
$R35$	18.18	2.84	6.03	3.01	0.08	52.88	0.83
$R36$	19.81	3.14	6.72	2.95	0.07	71.57	0.79

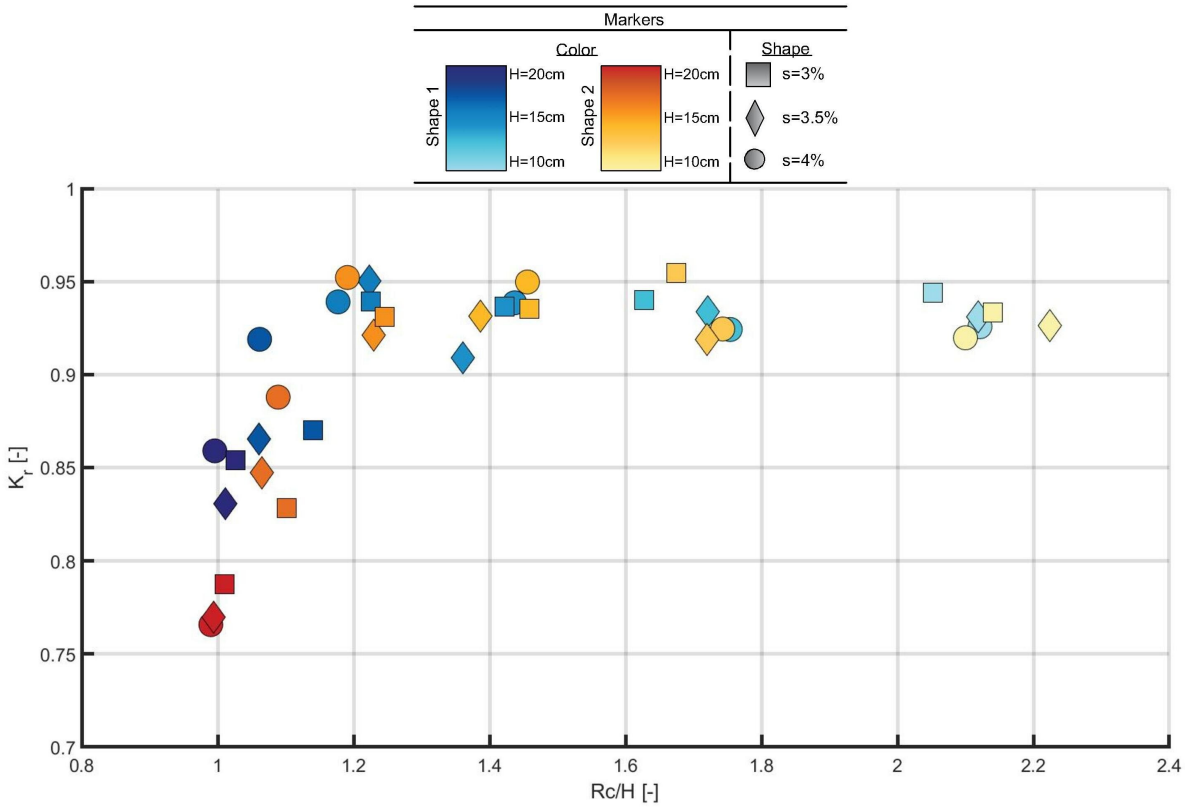

Figure 3.1: Scatter plot of mean values of reflection coefficient K_r against R_c/H per experiment; blue spectrum colors symbolize experiments performed with $S1$ and red spectrum colors for $S2$; light and dark hues distinguish between different wave target heights ($H = 10cm - H = 20cm$ respectively); wave target steepness of 4%, 3.5% and 3% is symbolized with circles, diamonds and squares respectively.

For the area $R_c/H < 1.20$, the values of $K_{r,S2}$ are lower compared to $K_{r,S1}$, especially for the highest wave height experiments with $H = 20cm$ (Figure 3.1, $R_c/H \approx 1$). As overtopping in the case of a vertical wall is

larger, this would logically lead to $K_{r,S1}$ being much lower than $K_{r,S2}$. This difference can be explained by the additional energy loss from the impact.

Consequently, it looks like the factor that decides if the value of K_r is steady, is the wave run-up. Energy loss from overtopping and the impact have solely to do with how high a wave can reach, while none of these occur if the water column does not reach the tip of the crownwall. For vertical walls, wave run-up is known to be a function of wave height and not wave period (Goda, 1974). It is logical though to express the reflection coefficient K_r in Figure 3.1 through the relative freeboard R_c/H. This is further enhanced by the fact that wave states of same wave height tend to have similar K_r (e.g. Figure 3.1 markers with same color and hue). For $R_c/H > 1.20$, all mean values with the same target wave height (and thus R_c/H) are more or less grouped up in the vertical. While for $R_c/H < 1.20$, a similar grouping of K_r occurs, which is a little more scattered as a result of the random nature of overtopping. This indeed shows that steepness, and thus wave period, do not have a large effect on the reflection coefficient.

3.2. Overtopping

It is pretty common to present scaled experimental results in a dimensionless way, as in this way it is easier to generalize and interpret them. The tests are performed with regular waves and therefore it is reasonable to express the resulting individual overtopping volumes V_i (Subsection 2.2.2) as the dimensionless volume per wave $V_i/(BH^2)$, where B is the mouth width.

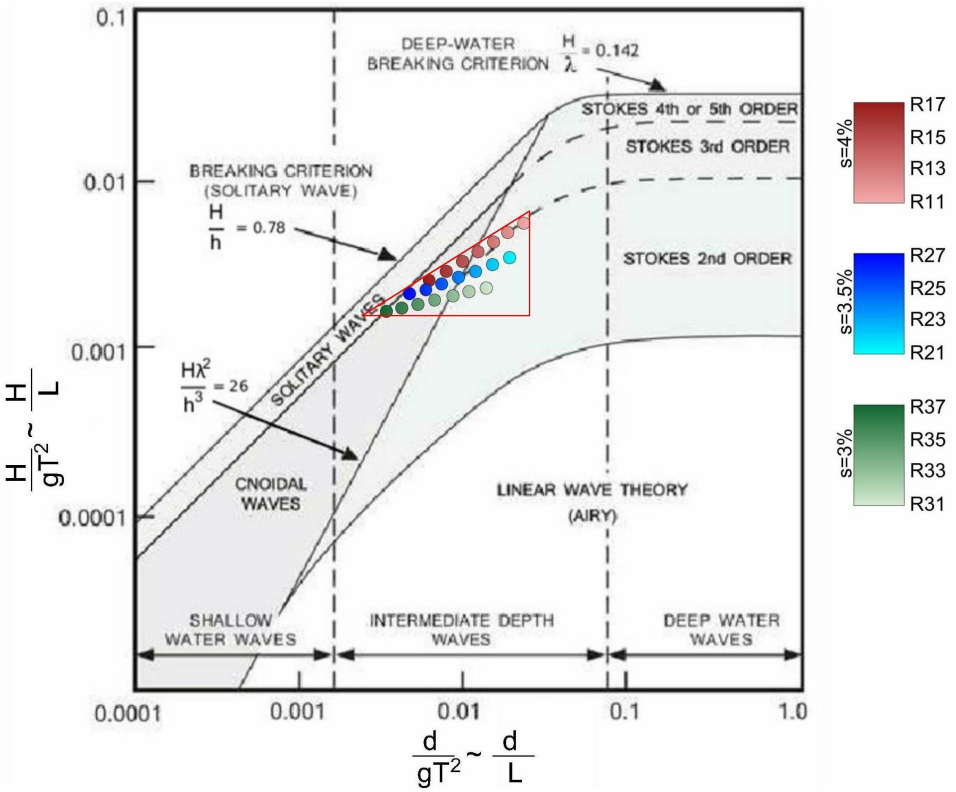

Figure 3.2: Validity of several theories for periodic water waves, according to Le Méhauté (2013). The different wave steepness of $s = 4\%$, $s = 3.5\%$ and $s = 3\%$ is distinguished with red, blue and green spectrum colors while lights and dark hues distinguish between low and large wave heights respectively.

Figure 3.2 presents the experiments performed on a diagram showing the validity of wave theories by Le Méhauté (2013). This figure shows on the y axis the ratio $\frac{H}{gT^2} \sim \frac{H}{L}$, which represents the wave steepness, while the x axis shows shows the ratio of $\frac{d}{gT^2} \sim \frac{d}{L}$, which represents the relative water depth. This figure indicates that the experimental results presented in this Chapter have a certain applicability range, which should be expressed through wave steepness s and relative water depth d/L, which will be discussed further in Chapter 5.

It is quite obvious that larger wave heights are closer to the solitary wave limit, meaning that the presence

of non-linearities will be more evident for these cases. Indeed, these are the cases which result in breaking, as described in Subsection 2.2.1. A way to estimate the degree of non-linearity of waves is the *Ursell* number $U = \frac{HL^2}{d^3}$ (Dingemans, 1997; Dingemans et al., 1987). For non-breaking waves, higher waves (H) can run-up higher on the crownwalls resulting in larger overtopping volumes, while longer waves (L) contain more water mass, resulting in larger overtopping volumes as well. This means, that with increasing U and for a standard water depth, the $Ursell$ number can be used to express overtopping. The problem with its use is that it does not provide any information regarding the crest freeboard, which is one of the dominant factors of overtopping. Naturally, low crests lead to higher overtopping volumes compared to higher crests for the same wave height. It is pretty common in hydraulic engineering to address this issue by expressing overtopping as a function of the relative freeboard R_c/H. For a standard crest freeboard, increasing R_c/H should result in decreasing overtopping volumes. The above lead to expressing $\frac{V}{BH^2}$ as a function of $\frac{U}{R_c/H} = \frac{H^2L^2}{R_c d^3}$.

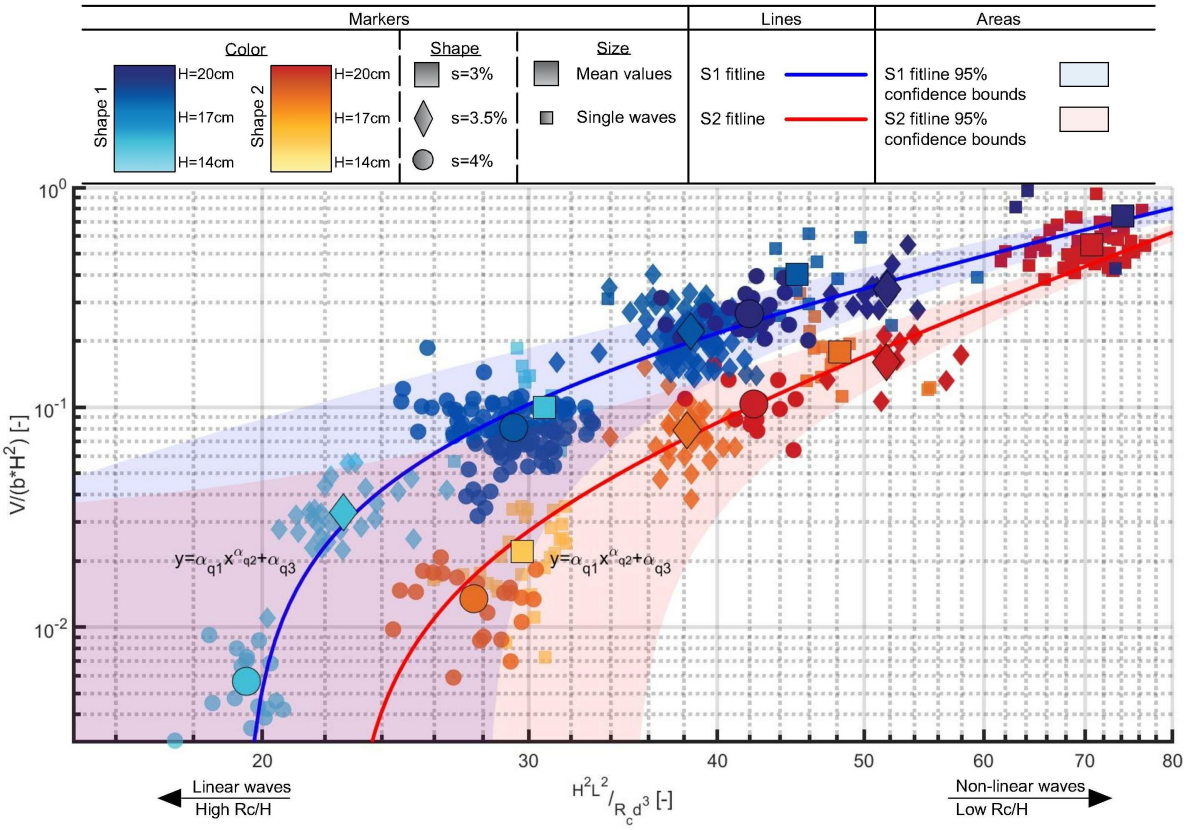

Figure 3.3: Scatter plot of dimensionless overtopping volume $\frac{V}{BH^2}$ against $\frac{U}{R_c/H}$ for single wave events (small markers) and mean values per experiment (larger markers); blue spectrum colors symbolize experiments performed with $S1$, red spectrum colors for $S2$; light and dark colors distinguish between different wave heights; wave target steepness of 4%, 3.5% and 3% is symbolized with circles, diamonds and squares respectively; fit results are presented as solid lines with their 95% confidence intervals as light shaded blue and red areas.

Results from all waves regarding the overtopping volumes are presented in Figure 3.3. In this plot, the dimensionless overtopping volume ($\frac{V}{BH^2}$) is used on the y axis and $\frac{U}{R_c/H}$ is used on the x axis. Single wave events are plotted with small markers, while the mean value per wave state is plotted with larger markers (e.g. Table 2.1). Blue spectrum colors represent experiments performed with $S1$, while red spectrum colors with $S2$. Hues of the spectra distinguish between wave heights, with light hues symbolizing low and dark hues higher wave heights. The circle (*R11-R16*), diamond (*R21-R26*) and square (*R31-R36*) shapes are used to distinguish between different steepness (4%, 3.5%, 3% respectively).

Wave height is the obvious variable that affects overtopping volumes, as higher wave heights (darker hues of blue and red spectra) are located on the top right of the plot, while lower wave heights (light hues of blue and red spectra) are located at the bottom.

Wave steepness is also found to greatly affect the overtopping volumes, as for waves with lower steepness (e.g. squares for $s = 3\%$), overtopping volumes are considerably higher. This can also be observed for same

wave height experiments; notice markers of same color and different shape on the graph. This confirms the initial assumption that both H and L are relevant to this phenomenon.

The effect of the parapet on the overtopping volumes is evident mainly for low wave height experiments for which the water column is blocked completely, or a large part of it is deflected. For the experiments with the largest overtopping volumes (e.g. $R36$, $\frac{U}{R_c/H} \approx 75$), the results for the two shapes almost coincide, which implies that a blocking threshold of the parapet exists. For a relatively large wave height, part of the wave can simply overtop the crownwall without interacting with it. The solid lines in Figure 3.3 are results of curve fitting the values of $\frac{V_i}{BH_i^2}$ and $\frac{U_i}{R_c/H_i}$. Both lines can be described as shown in Equation 3.1.

$$\frac{V}{(BH^2)} = \alpha_{q1}\left(\frac{U}{R_c/H}\right)^{\alpha_{q2}} + \alpha_{q3} \tag{3.1}$$

Where α_{q1} [−], α_{q2} [−] and α_{q3} [−] are fit coefficients as given in Table 3.3, V $[m^3/m]$ is the individual overtopping volume of the wave , H $[m]$ is the wave height, U [−] the *Ursell* number and R_c $[m]$ the crest freeboard.

Table 3.3: Mean values $\mu(\alpha_q)$ and standard deviation $\sigma(\alpha_q)$ of fit coefficients of overtopping.

Coefficient	$\mu(\alpha_{q,S1})$ [−]	$\sigma(\alpha_{q,S2})$ [−]	$\mu(\alpha_{q,S2})$ [−]	$\sigma(\alpha_{q,S1})$ [−]
α_{q1}	1.47×10^{-3}	4.57×10^{-4}	9.10×10^{-6}	3.47×10^{-6}
α_{q2}	1.47	7.04×10^{-2}	2.55	8.72×10^{-2}
α_{q3}	-1.15×10^{-1}	1.61×10^{-2}	-2.60×10^{-2}	1.11×10^{-2}

3.3. Pressure and impacts

3.3.1. Pressure

Figures 3.4 and 3.5 present the pressure profiles on the two superstructures at the moment of maximum pressure per wave state (Table 2.1). The pressure profiles (Figures 3.4, 3.5, blue line) are produced by plotting these readings on the x axis and connecting them with a straight line. In these figures, experiments with the same target wave steepness are presented in same columns, while experiments with same target wave height are shown in same rows. Each of the black dashed lines indicate the position of a pressure sensor. Note that the x axis limits are identical for the cases of Figure 3.4 and Figure 3.5a-Figure 3.5i, and for the cases of 3.5j-3.5r.

Pressure distribution for $S1$ is trapezoidal and the maximum pressure occurs near SWL at $PS1$, which comes in line with the findings of Goda (1974). The effect of wave height is also evident; notice how the peak pressure evolves for experiments of waves with same steepness and different wave height e.g. compare subfigures vertically on the graph. On the other hand, there seems to be an effect of the wave steepness on pressure as well, especially for the highest wave states e.g. compare subfigures of the same row. While the peak pressures of $R11$ (Figure 3.4a) and $R21$ (Figure 3.4b) are just a little lower than $R31$ (Figure 3.4c), for higher wave states this difference becomes much larger. For example, the maximum pressure for experiments $R16$ (Figure 3.4p), $R26$ (Figure 3.4q) and $R36$ (Figure 3.4r) is approximately 1.75 kPa, 1.9kPa and 2.4 kPa respectively. As a result, there seems to be some correlation between wave steepness and maximum pressure. This is not the case for wave run-up though. Although the number of points is small, these pressure profiles can give an indication regarding wave run-up. With only the exemption of $R33$, same pressure sensors are triggered for experiments of same wave height e.g. compare subfigures horizontally. Notice for example the lowest point of the crownwall at each subfigure for which pressure is 0. It can be concluded though, that wave run-up is mostly dominated by wave height rather than wave steepness. This comes in agreement with the formulas of Goda (1974) (Equation B.1) for the vertical wall.

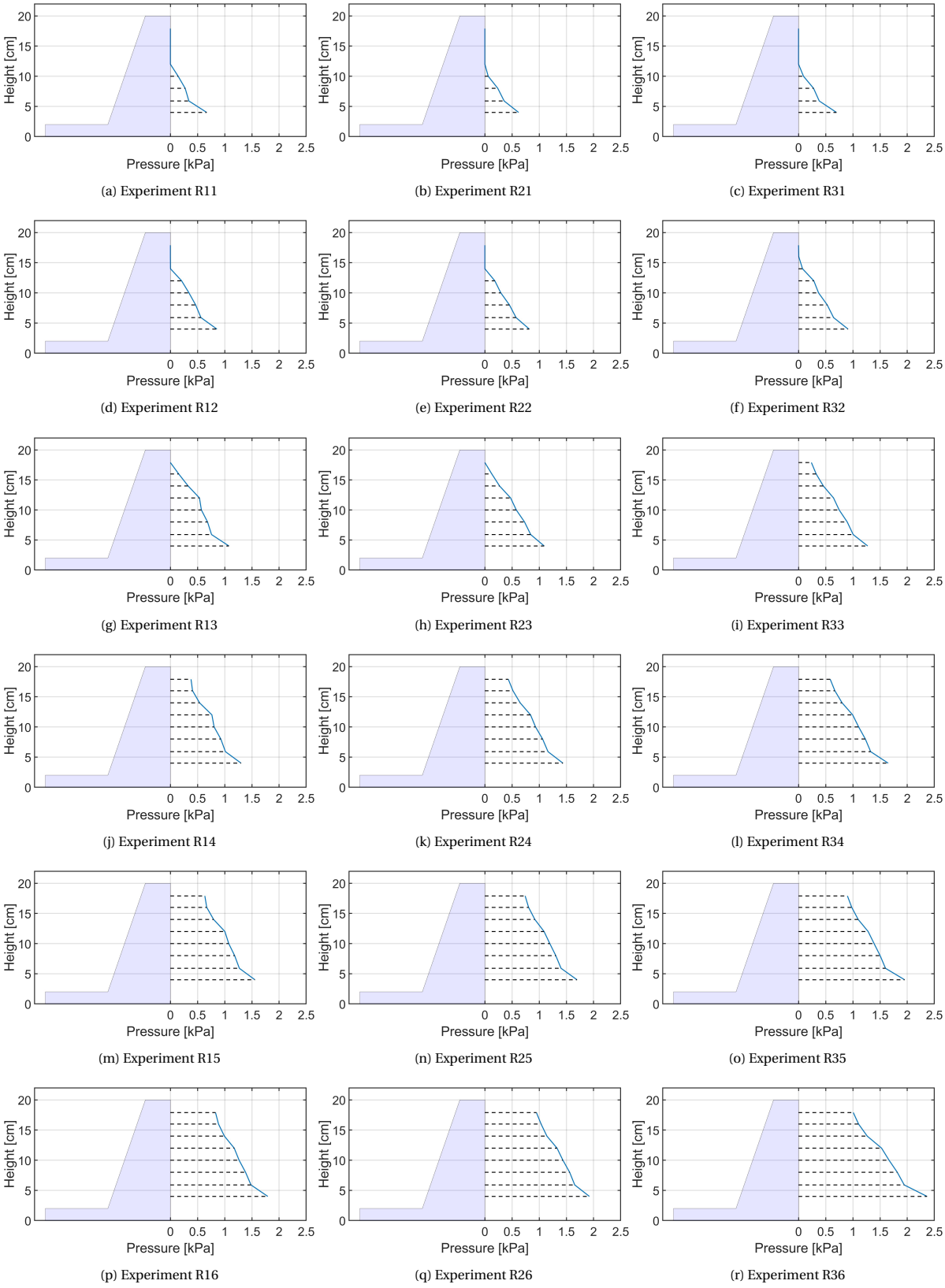

(a) Experiment R11 (b) Experiment R21 (c) Experiment R31

(d) Experiment R12 (e) Experiment R22 (f) Experiment R32

(g) Experiment R13 (h) Experiment R23 (i) Experiment R33

(j) Experiment R14 (k) Experiment R24 (l) Experiment R34

(m) Experiment R15 (n) Experiment R25 (o) Experiment R35

(p) Experiment R16 (q) Experiment R26 (r) Experiment R36

Figure 3.4: Plots of pressure distribution on $S1$ per wave state at the moment of maximum pressure.

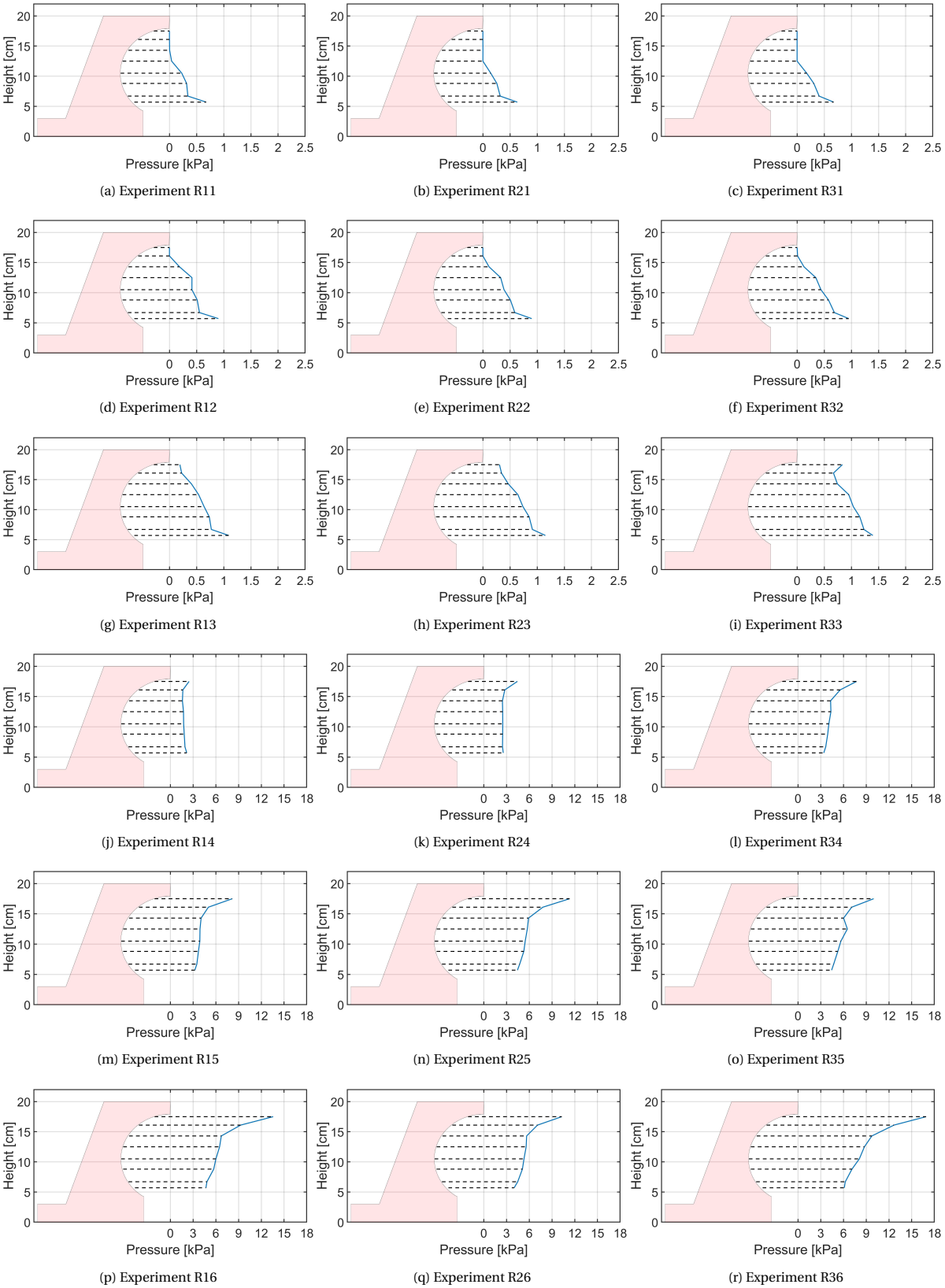

(a) Experiment R11 (b) Experiment R21 (c) Experiment R31

(d) Experiment R12 (e) Experiment R22 (f) Experiment R32

(g) Experiment R13 (h) Experiment R23 (i) Experiment R33

(j) Experiment R14 (k) Experiment R24 (l) Experiment R34

(m) Experiment R15 (n) Experiment R25 (o) Experiment R35

(p) Experiment R16 (q) Experiment R26 (r) Experiment R36

Figure 3.5: Plots of pressure distribution on *S*2 per wave state at the moment of maximum pressure.

The case of *S*2 in Figure 3.5 is completely different. For Figures 3.4a-3.4f there is a remarkable similarity between the trapezoidal distributions of *S*1 and *S*2, but in this case there is an evident spike at the bottom.

This difference is attributed to the orientation of the recurve, as the two superstructures receive loads in a different way. The vertical wall receives horizontal loads, while the crownwall receives loads in both directions. The maximum pressure for these cases occurs at $PS1$, and these cases are very similar to the vertical wall, as impacts do not occur and the load is quasi-static. Maximum pressure for these cases is very similar for different values of wave steepness (e.g. compare subfigures of the same row), as waves with lower steepness have slightly more pressure. For the wave states of Figures 3.4g-3.4i, the water column triggers $PS8$ and almost fills the entire area below the recurve. Experiments $R13$ and $R23$ have a trapezoidal distribution, while the longer wave of $R33$ applies a larger pressure on the crownwall, and a spike is evident (Figure 3.5i). For all of these cases, maximum pressure occurs again at $PS1$, while as already mentioned (Subsection 2.2.3) only the cases of $R23$ and $R33$ are considered in the results of impacts. For larger wave states (Figures 3.5j-3.5r), large impulsive load occurs and the distribution changes considerably, as the largest pressure for these cases occurs at $PS8$. This confirms the fact that impacts occur at the outer edge of the recurve, similarly to recurved parapets (Castellino et al., 2018). The effect of wave steepness is higher for increasing wave height, as for these longer waves pressure is evidently larger. Lastly, for all experiments of same wave height, the same pressure sensors are triggered. This leads to the same conclusion as for the vertical wall that wave run-up is not dominated from wave steepness, and results in similarly shaped distributions for same wave heights.

As a result of the above, similar arguments as in Section 3.2 can be made for pressure. The effect of wave steepness becomes important for higher waves that generate impacts, as longer (L) and higher (H) waves apply a larger load. For the same water depth, high U numbers translate to long, high waves and eventually high pressure (Figures 3.4,3.5). It is reasonable though to express pressure through $U = \frac{HL^2}{d}$. On the other hand, the nature of the load, quasi-static or impulsive, is directly related to the wave run-up, and consequently the relative freeboard. Waves with low R_c/H reach the tip of the parapet and generate impulsive loads, while waves with high R_c/h apply a quasi static load. As a result, both of these dimensionless numbers are used and dimensionless pressure $\frac{P}{\rho g H}$ is expressed as a function of $\frac{U}{R_c/H}$.

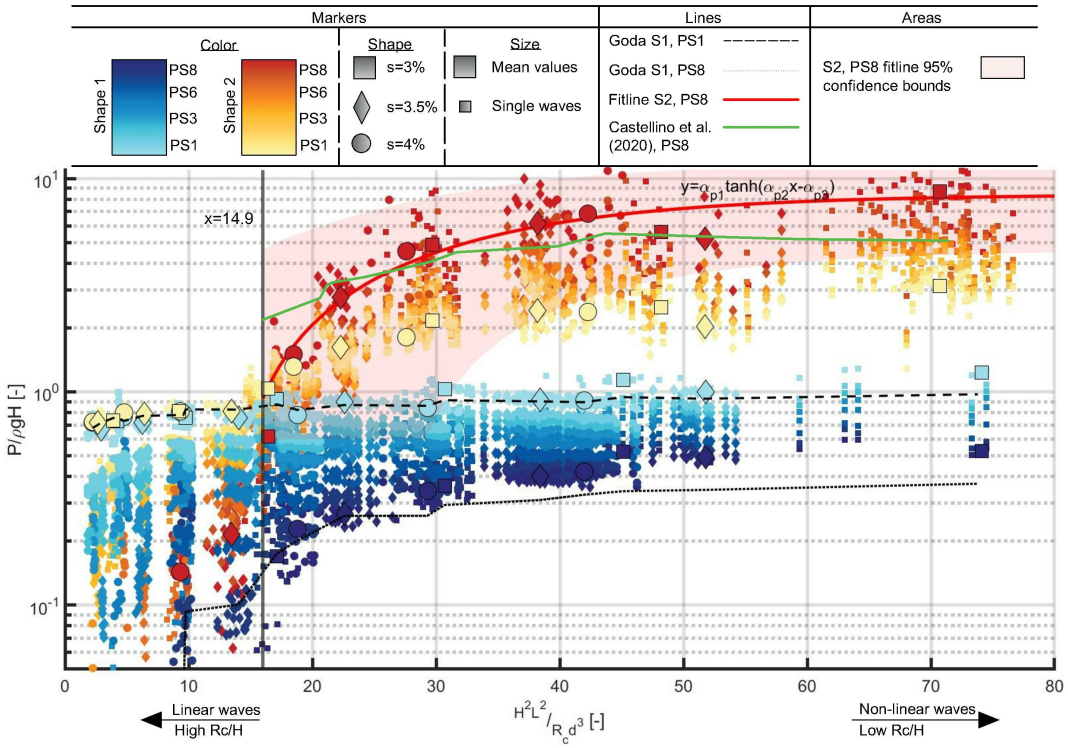

Figure 3.6: Scatter plot of dimensionless peak pressure $\frac{P}{\rho g H}$ from all pressure sensors against $\frac{U}{R_c/H}$ for single wave events (small markers) and mean values per experiment (larger markers); blue spectrum colors symbolize experiments performed with $S1$, red spectrum colors for $S2$; light and dark hues distinguish the signal used from different pressure sensors; wave target steepness of 4%, 3.5% and 3% is symbolized with circles, diamonds and squares respectively; fit result is presented as a solid red line with its 95% confidence intervals as a light shaded red area.

Results of the experiments regarding the maximum pressure are shown in Figure 3.6. In this plot, the di-

mensionless pressure ($\frac{P}{\rho g h}$) is used on the y axis and $\frac{U}{R_c/H}$ is used on the x axis. Single wave events are plotted with small markers, while the mean values of each wave state are shown with large markers. The corresponding $\frac{U}{R_c/H}$ number of these mean values is calculated by using the mean values of wave characteristics (Tables 3.1 and 3.2). Blue spectrum colors represent experiments performed with $S1$, while red spectrum colors with $S2$. Hues are used to identify maximum pressure from different pressure sensors, with $PS1$ having the lightest hue and $PS8$ the darkest. The circle (*R11-R16*), diamond (*R21-R26*) and square (*R31-R36*) shapes are used to distinguish between different wave steepness (4%, 3.5%, and 3% respectively). The dashed black line is calculated from the Goda (1974) formula (Equations B.1-B.9) for $S1$, by using the mean values of H and L per wave state (Tables 3.1 and 3.2). The wave propagation angle relative to the crownwall is 0 and the wall is vertical, therefore the variables $\beta = 0, \lambda_1 = 0$, $\lambda_2 = 0$ and $\lambda_3 = 0$ are used in the application of the *Goda* formula. The green line is calculated by using the methodology of Castellino et al. (2021), as described in Appendix B.3. For this method, pressure at $PS8$ is calculated by using the mean values of wave characteristics per wave state for $S2$ (Table 3.2) and the overhang length $l = 4\,cm$.

Pressure developed on $S1$ is described very well by the *Goda* formula for $s = 4\%$ (circles) and $s = 3.5\%$ (diamonds), while it is slightly underestimated for experiments with $s = 3\%$ (squares). Notice for example for $\frac{U}{R_c/H} \geq 14.9$, the mean values of $PS1$ for $S1$ and $s = 3\%$ (large, light blue squares) lie above the *Goda* approximation. On the other hand, the application of *Goda* formula for the position of $PS8$ (Figure 3.3, dotted line) is lower compared to the calculated mean values per experiment; notice the relative position of this line and dark blue markers. It is evident that for the vertical wall, the highest pressure occurs for $PS1$ (Equation 3.2, light hue, blue spectrum), and the lowest on the top $PS8$ which comes in line with the findings by Goda (1974). Thus, the Goda (1974) formula predicts fairly well maximum pressure at *SWL*, but it underestimates pressure at higher positions of the wall.

The crownwall receives very similar loads to the vertical wall for $\frac{U}{R_c/H} \leq 14.9$ and maximum pressures are well described by the Goda formula. Maximum pressure for these cases occurs for the lowest pressure sensor $PS1$ (Equation 3.2,dark red color) while after the transition point, waves completely fill the area below the recurve and impacts cause a rapid increase of the pressure and deviation from the Goda formula. The formula of Castellino et al. (2021) is positioned mostly below the experimental results of $PS8$ (Figure 3.6, dark red hues), showing possibly that a crownwall with a fully curved face receives larger loads compared to recurved parapets. For $\frac{U}{R_c/H} \approx 70$, the red fit line of the crownwall results is approximately 45% larger than the application of Castellino et al. (2021). The highest pressure for these results occurs for *PS8* (Figure 3.6, dark red color), and the trend plotted against $\frac{U}{R_c/H}$ can be approximated with a *tanh* function, as shown in Equation 3.2. This function with its confidence bounds are highlighted in red and transparent red color respectively in Figure 3.6.

$$\frac{P}{\rho g H} = \alpha_{p1}\, tanh(\alpha_{p2}\frac{U}{R_c/H} - \alpha_{p3}) \qquad for\ \frac{U}{R_c/H} \geq 14.9 \tag{3.2}$$

Where α_{p1} [−], α_{p2} [−] and α_{p3} [−] are fit coefficients as given in Table 3.4, P $[N/m^2]$ is the maximum pressure at the outer edge of the recurve, H $[m]$ is the wave height, U [−] the *Ursell* number and R_c $[m]$ the crest freeboard. The mean values and standard deviations of the fit coefficients are given in Table 3.4. The limit of $\frac{U}{R_c/H} = 14.9$ is defined at the crossing point of the Goda formula application and the fitline.

Table 3.4: Mean values $\mu(\alpha_{p1})$ and standard deviation $\sigma_(\alpha_{p2})$ of fit coefficients of pressure.

Coefficient	$\mu(\alpha_p)$ [−]	$\sigma(\alpha_p)$ [−]
α_{p1}	8.42×10^{1}	3.53×10^{-1}
α_{p2}	3.46×10^{-2}	7.78×10^{-3}
α_{p3}	4.42×10^{-1}	7.47×10^{-2}

These results show that a threshold for this equation exists; for very large $\frac{U}{R_c/H}$, water positioned higher in the water column would simply overtop the structure without causing any additional impulsive load, similarly as explained in Section 3.2. This threshold value for the 95% confidence interval can be approximated by considering $tanh(\alpha_{p2}\frac{U}{R_c/H} - \alpha_{p3}) = 1$ for large $\frac{U}{R_c/H}$ values and using $\alpha_{p1,95\%} = \mu(\alpha_{p1}) + 1.96\sigma(\alpha_{p1}) = 9.1$, as shown in Equation 3.3. This equation shows that $P/\rho g H$ tends to become constant for large values of $\frac{U}{R_c/H}$. This means that steepness is relevant mainly for $\frac{U}{R_c} \approx 15 - 60$, while wave height is dominating for all wave states. The results of $S1$ show a similar type of distribution, as the trends of all sensors tend to attain a steady

$P/\rho gH$ mean value. This shows the dominancy of wave height on this phenomenon. Higher sensors like $PS7$ or $PS8$ have an increasing trend for the lowest $\frac{U}{R_c/H}$ values, showing that wave length, thus wave steepness, is relevant in this interval.

$$P = 9.1\rho gH \qquad for\ \frac{U}{R_c/H} \geq 60 \tag{3.3}$$

3.3.2. Impulse

As impulses are derived from the pressure signal, both the impulse I_j and impulse duration t_{imp} are expressed through $\frac{U}{R_c/H}$, similarly as described in Subsection 3.3.1. Figure 3.7 presents collective results of I. Similarly as the case of pressure, the dimensionless impulse ($\frac{I}{\rho ghT}$) is used on the y axis and $\frac{U}{R_c/H}$ is used on the x axis. Individual impulses are plotted with small markers for the experiments which impacts occur. The larger markers represent the mean values of of $I_{i,j=8}$ and are shown only for $PS8$. This plot naturally presents only results from $S2$, as for $S1$ impacts do not occur (Subsection 2.2.3). Hues in this case are used to distinguish different pressure sensors, with $PS1$ having the lightest hue and $PS8$ the darkest. The circle ($R14$-$R16$), diamond ($R23$-$R26$) and square ($R33$-$R36$) shapes are used to distinguish between different steepness (4%, 3.5%, 3% respectively).

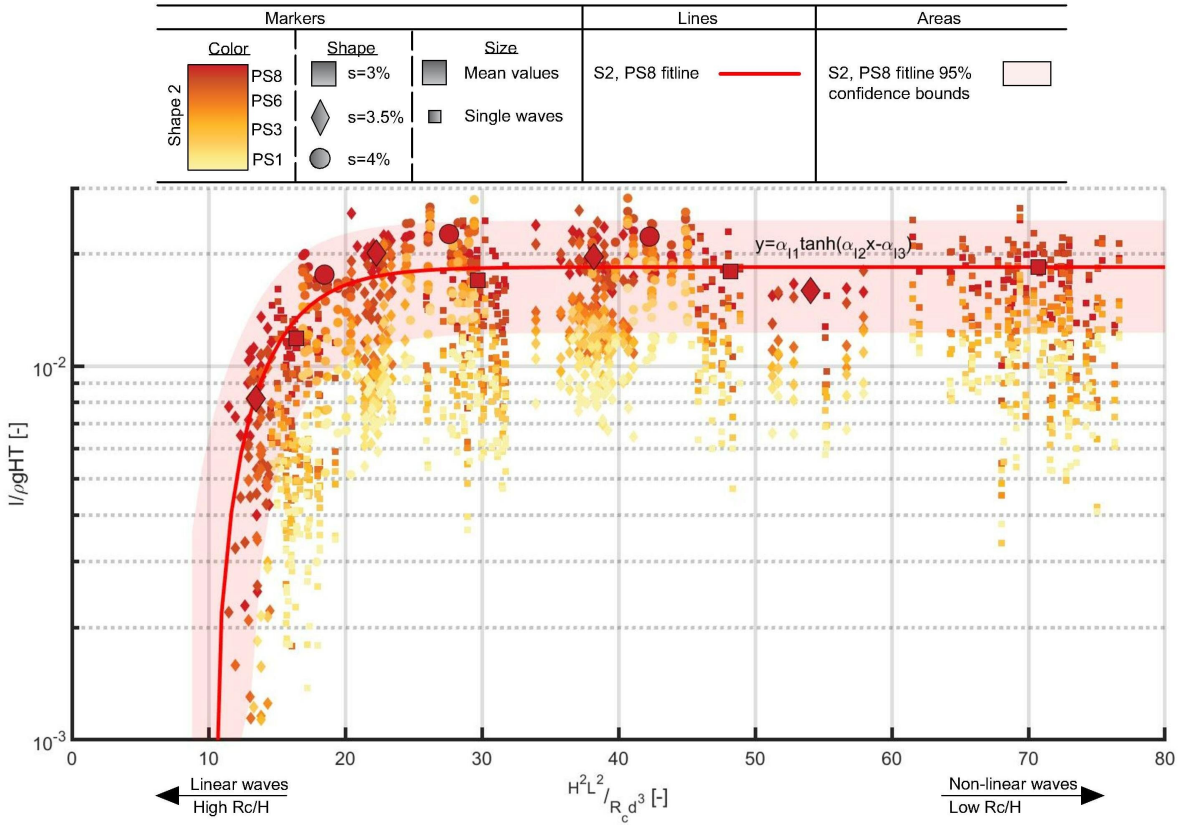

Figure 3.7: Scatter plot of dimensionless impulse $\frac{I}{\rho gHT}$ against $\frac{U}{R_c/H}$ for single wave events (small markers) and mean values per experiment (larger markers); red-yellow spectrum colors symbolizes experiments performed with $S2$; light and dark hues distinguish the signal used from different pressure sensors; wave target steepness of 4%, 3.5% and 3% is symbolized with circles, diamonds and squares respectively; the fit result is presented as a solid line with its 95% confidence intervals as a light shaded red area.

Impulsive loading occurs for waves who reach the outermost crownwall edge, which is for experiments $R14-R16$, $R23-R26$ and $R33-R36$ (Subsection 2.2.3). For experiments with $\frac{U}{R_c/H} \geq 20$, impulses look relatively constant, but comparing with Figure 3.6, maximum pressure attains a constant value for approximately $\frac{U}{R_c/H} \approx 60$. This is because the increase of the peak pressure is compensated by the reduction of the impulse duration, which is demonstrated below in Subsection 3.3.3.

The largest values of impulse occur for $PS8$, as the value $I/\rho gHT$ is lower for lower parts of the crownwall. This furthermore confirms the statement that impacts occurs at the outer edge of the crownwall. These

impulses can be described similarly to the case of pressure by a $tanh$ function, which is given for $PS8$ in Equation 3.4.

$$\frac{I}{\rho g H T} = \alpha_{I1} tanh\left(\alpha_{I2} \frac{U}{R_c/H} - \alpha_{I3}\right) \tag{3.4}$$

Where α_{I1} $[-]$, α_{I2} $[-]$ and α_{I3} $[-]$ are fit coefficients as given in Table 3.5, I $[Ns/m^2]$ is the impulse, H $[m]$ is the wave height , U $[-]$ the *Ursell* number and R_c $[m]$ the crest freeboard. Interestingly, the coefficients of variation ($\nu = \sigma/\mu$) of the fit coefficients of impulse $\nu(a_{i1}) = 1.38 \times 10^{-2}$, $\nu(a_{i2}) = 1.33 \times 10^{-1}$ and $\nu(a_{i3}) = 1.88 \times 10^{-1}$ are smaller than the corresponding coefficients of variation of the fit coefficients of pressure (Equation 3.2) $\nu(a_{p1}) = 4.23 \times 10^{-2}$, $\nu(a_{p2}) = 1.75 \times 10^{-1}$ and $\nu(a_{p3}) = 2.05$. This indicates that indeed impulses are more stable and predictable compared to peak pressure. For $\frac{U}{R_c/H} \approx 20$, this equation attains a relatively constant value and can be approximated by setting $tanh\left(\alpha_{I2} \frac{U}{R_c/H} - \alpha_{I3}\right) = 1$. Then, the 95% confidence bound of this equation can be approximated by using $\alpha_{I1,95\%} = \mu(\alpha_{I1}) + 1.96\sigma(\alpha_{I1}) \approx 1.9$, as shown in Equation 3.5.

Table 3.5: Mean values $\mu(\alpha_I)$ and standard deviation $\sigma(\alpha_I)$ of fit coefficients of impulse.

Coefficient	$\mu(\alpha_I)$ $[-]$	$\sigma(\alpha_I)$ $[-]$
α_{I1}	1.84×10^{-2}	2.55×10^{-4}
α_{I2}	1.46×10^{-1}	1.95×10^{-2}
α_{I3}	1.48	2.78×10^{-1}

$$I = 1.9 \rho g H T \qquad \text{for} \quad \frac{U}{R_c/H} > 20 \tag{3.5}$$

3.3.3. Impulse duration

Impulse duration on the other hand follows a hyperbolic trend as shown in Figure 3.8. This plot presents the impact duration formulated in a dimensionless way by dividing with the corresponding wave period (t_{imp}/T), as a function of $\frac{U}{R_c/H}$. Obviously, the wave events contained in Equation 3.6 correspond to the ones in Figure 3.7 for impulse, meaning that this graph contains results from $R14-R16$,$R23-R26$ and $R33-R36$, as for lower wave height impacts do not occur. The symbolism of the markers is the same as the one used in Figure 3.7.

The hyperbolic trend means that the impulse duration t_{imp} gets shorter with an increasing $\frac{U}{R_c/H}$ ratio, which makes sense for two reasons.

As already explained, high $\frac{U}{R_c/H}$ ratio can mean a high U, which translates to higher pressure and higher run up. These waves produce more violent impacts, resulting in a more rapid peak in the pressure signal.

Alternatively, it can mean low R_c/H. According to linear wave theory, orbital velocities are proportional to the wave amplitude α, and thus H. This means that a low R_c/H ratio can be translated to high H, and thus high orbital velocities, with a low crest freeboard R_c. Because the maximum vertical orbital velocities occur at SWL, a low R_c/H also means small distance between SWL and the outer edge of the recurve, and a theoretically larger velocity at the outer edge of the crownwall.

Eventually, both of these aspects affect the duration of the impulse, as waves with a low R_c/H and high U cause more violent and quick impacts. The function for approximating the impulse duration is given in Equation 3.6.

$$\frac{t_{imp}}{T} = \frac{\alpha_{t1}}{\frac{U}{R_c/H} + \alpha_{t2}} \tag{3.6}$$

Where α_{t1} $[-]$ and α_{t2} $[-]$ are fit coefficients as given in Table 3.6, t_{imp} $[s]$ is the impulse duration, H $[m]$ is the wave height, U $[-]$ the *Ursell* number and R_c $[m]$ the crest freeboard.

Table 3.6: Mean values $\mu(\alpha_t)$ and standard deviation $\sigma(\alpha_t)$ of fit coefficients of impulse duration.

Coefficient	$\mu(\alpha_t)$	$\sigma(\alpha_t)$
α_{t1}	8.49×10^{-1}	4.45×10^{-2}
α_{t2}	6.32×10^{-1}	7.78×10^{-1}

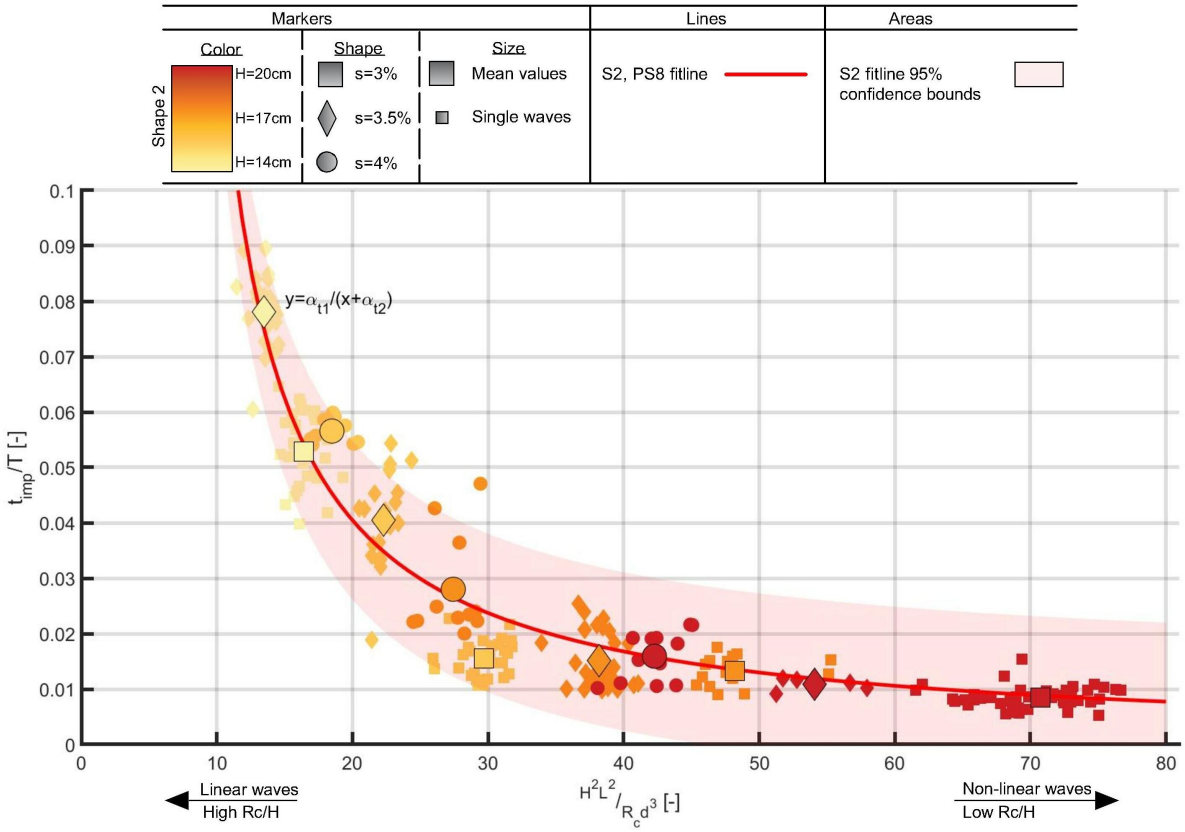

Figure 3.8: Scatter plot of dimensionless impulse duration $\frac{t_{imp}}{T}$ against $\frac{U}{R_c/H}$ for single wave events (small markers) and mean values per experiment (larger markers); red-yellow spectrum colors symbolizes experiments performed with S2; light and dark colors distinguish between different wave heights; wave target steepness of 4%, 3.5% and 3% is symbolized with circles, diamonds and squares respectively; the fit result is presented as a solid line with its 95% confidence intervals as a light shaded red area.

3.4. Wave forces

3.4.1. Loading

Results regarding wave forces are summarized in Figure 3.9, with the same symbolism as the one described for pressure. As force is derived by integrating the pressure signal on the contact surface A_j, it is logical to express dimensionless force $F/(\rho g H^2)$ against the same variable $\frac{U}{R_c/H}$, and naturally this plot follows a similar trend as pressure (Equation 3.2). The *Goda* formula is applied for the case of $S1$ by making use of the mean values of H and T (Tables 3.1 and 3.2), while mean L is calculated from the linear dispersion relationship. Pressure distribution is assumed trapezoidal in this formula, therefore pressure is calculated at SWL and at the highest point of the crownwall on which the wave runs up. These values of pressure are integrated on the surface of the crownwall with the methodology described in Subsection 2.2.4 resulting in the dashed line shown in Figure 3.9.

In this plot, two areas can be distinguished as $\frac{U}{R_c/H} = 14.7$ separates them. For $\frac{U}{R_c/H} < 14.7$, the low wave states result in a quasi static forcing for both shapes, which is pretty similar for $S1$ and $S2$. This is logical though since the pressure distributions are very similar for these cases (Figure 3.4, Figure 3.5), while the forces of $S2$ are slightly larger as a result of the larger integration surface of the recurve. The *Goda* formula slightly underestimates the pressure for $S1$, which is anticipated since it is shown in Section 3.3 that the formula underestimates pressure at higher positions of the crownwall. For values larger than $\frac{U}{R_c/H} = 14.7$, the results of

S1 follow the trend of the *Goda* formula approximation, (Figure 3.9, black dashed line) but have a considerably larger value.

For *S2*, the function showing the trend of the results for $\frac{U}{R_c/H} > 14.7$ is given in Equation 3.7. The limit $\frac{U}{R_c/H} = 14.7$ is the point around which roughly impacts start to occur, and differs slightly from $\frac{U}{R_c/H} = 14.9$ which is the margin for pressure (Equation 3.2). This is logical though, as both points are calculated as the crossing point of the *Goda* approximation and the fit function, while the integration and uncertainty in the fitting make them differ slightly.

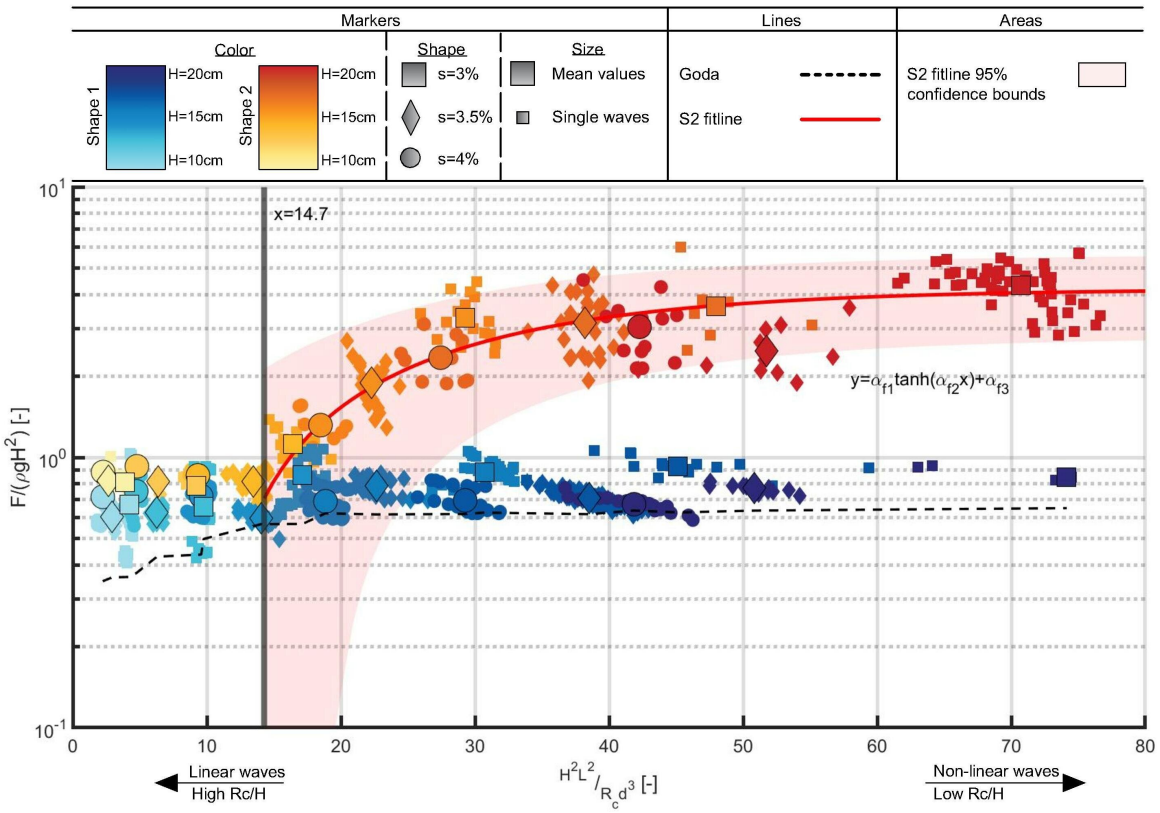

Figure 3.9: Scatter plot of dimensionless peak force $\frac{F}{\rho g H L}$ against $\frac{U}{R_c/H}$ of single wave events (small markers) and mean values per experiment (larger markers); blue spectrum colors symbolize experiments performed with S1 and red spectrum colors for S2; light and dark colors distinguish between different target wave heights; wave target steepness of 4%, 3.5% and 3% is symbolized with circles, diamonds and squares respectively; fit results are presented as solid lines with their 95% confidence intervals as light shaded red areas.

$$\frac{F}{\rho g H^2} = \alpha_{f1} tanh\left(\alpha_{f2} \frac{U}{R_c/H} - \alpha_{f3}\right) \qquad \text{for} \quad \frac{U}{R_c/H} \geq 14.9 \tag{3.7}$$

Where α_{f1} [−], α_{f2} [−] and α_{f3} [−] are fit coefficients as given in Table 3.7, F [N] is the force, H [m] is the wave height, A [m] is the contact surface of water and crownwall, U [−] the *Ursell* number and R_c [m] the crest freeboard. A similar asymptote can be calculated for the 95% confidence bound and for approximately $\frac{U}{R_c/H} \geq 60$ by using $\alpha_{f1,95\%} = \mu(\alpha_{f1}) + 1.96\sigma(\alpha_{f1}) = 6.9$, as shown in Equation 3.8.

$$F = 6.9 \rho g H^2 \qquad \text{for} \quad \frac{U}{R_c/H} \geq 60 \tag{3.8}$$

Table 3.7: Mean values $\mu(\alpha_f)$ and standard deviation $\sigma(\alpha_f)$ of fit coefficients of force.

Coefficient	$\mu(\alpha_f)$	$\sigma(\alpha_f)$
α_{f1}	6.05	4.27×10^{-1}
α_{f2}	3.16×10^{-2}	3.22×10^{-3}
α_{f3}	1.86	4.94×10^{-1}

3.4.2. Point of application

This section presents the results regarding the point of application of the force in the vertical direction relative to SWL (ζ), following the methodology described in Subsection 2.2.4. ζ is formulated in a dimensionless form as ζ/R_c, as this gives an instant indication of the vertical position of the force relative to the crownwall. When integrating on a surface, the point of application of the force is affected by two things; the wave run-up and the pressure distribution. Wave states with similar pressure distribution shape but different magnitudes result in the same ζ. Both of these aspects are discussed in Subsection 3.3.1, in which it is shown that the wave load is affected by wave steepness, but the latter is not highly relevant to the shape of the distribution and wave run-up . For example, assuming two cases of same wave height and different wave length (e.g. Figures 3.4m and 3.4o) the two distributions have the same shape but different maximum values. Integrating the pressure distribution results in a difference in the point of application of 2%. This indicates that there is no evident effect of wave steepness, and thus wave length, on ζ. Consequently, z/R_c is expressed through R_c/H as shown in Figure 3.10, and the Ursell number is not used.

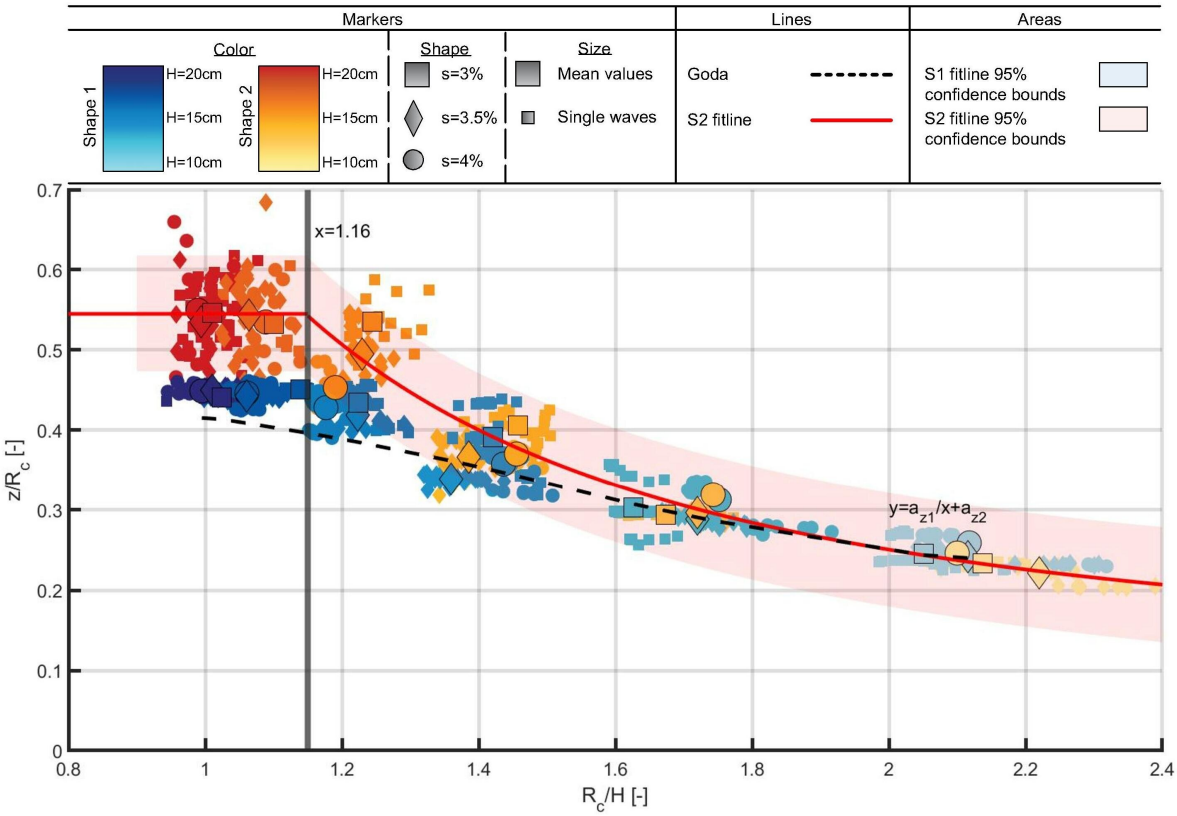

Figure 3.10: Scatter plot of dimensionless vertical coordinate of peak force application point (z/R_c) against $\frac{R_c}{H}$ for single wave events (small markers) and mean values per experiment (larger markers); red spectrum colors symbolize experiments performed with S2; light and dark hues distinguish between different wave heights; wave target steepness of 4%, 3.5% and 3% is symbolized with circles, diamonds and squares respectively; fit results are presented as solid lines with their 95% confidence intervals as light shaded blue and red areas.

In this figure, similar symbolism as the one described in Figure 3.9 is used. The *Goda* formula (Figure 3.10, dashed line) is applied by making use of the mean values of H and L of each wave state. Pressure is calculated at the SWL and at the highest run-up point of the crownwall. ζ for *Goda* is then calculated by integrating the trapezoidal distribution following the methodology described in Subsection 2.2.4.

For high R_c/H, the point of application is almost identical for the two lines and ζ is predicted very well by the Goda formula. The pressure applied is quasi-static and the point of application is totally defined by the wave run-up. The point of application ζ increases for decreasing R_c/H as a result of the higher run-up and the orientation of the recurve. For $R_c/H \approx 1.16$, the results of the two experiments start to deviate a lot, while the *Goda* formula predicts fairly well ζ for $S1$. The wave states shown around this point are $R13$ (Figure 3.4g), $R23$ (Figure 3.4h), $R33$ (Figure 3.4i), with $R23$ and $R33$ being the lowest wave height experiments in which waves reach $PS8$. The results of pressure show that the highest load occurs at the highest outer edge of the

crownwall(e.g. Figure 3.5r), which explains why the point of application for $S2$ is higher compared to $S1$. The function describing ζ for $R_c/H > 1.16$ is a hyperbola, as given in Equation 3.9b.

For $R_c < 1.16$, the mean value of the application point is steady, as a result of the similarly shaped distributions (Figure 3.5) of experiments. The function describing ζ for this interval as given in Equation 3.9a, is calculated as the mean value of ζ_i for wave states with $R_c/H \leq 0.2/0.18 = 1.11$. The transition point $R_c/H = 1.16$ is defined at the crossing of the two lines, and corresponds to the $\frac{U}{R_c/H} = 14.9$ limit found in Equation 3.2. Using the mean values of H and L of an experiment around this point (e.g. $R23$) and $d = 0.5$, R_c/H can be modified as $\frac{U}{R_c/H} = 15.1$, showing its relation with the limit $\frac{U}{R_c/H} = 14.9$ that was derived for pressure.

$$\zeta = \begin{cases} \alpha_{\zeta 1} & R_c/H < 1.16 \quad (3.9a) \\ \alpha_{\zeta 2}\left(R_c/H\right)^{\alpha_{\zeta 3}} + \alpha_{\zeta 4} & R_c/H \geq 1.16 \quad (3.9b) \end{cases}$$

Where ζ is the vertical point of application of the force, H the wave height, U $[-]$ the *Ursell* number and R_c $[m]$ the crest freeboard. $\alpha_{\zeta 1}$ $[-]$ and $\alpha_{\zeta 2}$ $[-]$ are fit coefficients as given in Table 3.8.

Table 3.8: Mean values $\mu(\alpha_\zeta)$ and standard deviation $\sigma(\alpha_\zeta)$ of fit coefficients of force angle.

Coefficient	$\mu(\alpha_{\zeta 1})$	$\sigma(\alpha_{\zeta 1})$
$\alpha_{\zeta 1}$	5.55×10^{-1}	3.5×10^{-2}
$\alpha_{\zeta 2}$	5.19×10^{-1}	7.78×10^{-2}
$\alpha_{\zeta 3}$	-9.54×10^{-1}	2.42×10^{-1}
$\alpha_{\zeta 4}$	-9.59×10^{-3}	8.56×10^{-2}

3.4.3. Force angle

This section presents the results regarding the angle of force θ relative to the flat bottom following the methodology described in Subsection 2.2.4. These results are presented in Figure 3.11, while the symbolism is the same as the one described in Subsection 3.4.1. Naturally, only results for $S2$ are presented as the angle of application for the vertical wall is always 0. In this plot, θ is expressed through R_c/H because the angle of application of the force is totally defined by the point of application of the force. Waves which run-up higher on the superstructure apply load with different angle as a result of the orientation of the recurve. In addition, as shown in Subsection 3.4.2, wave steepness does not dominate ζ, as the mean values of experiments with same R_c/H and different wave steepness group up in the vertical. This means that waves of similar wave height are expected to have similar ζ and thus similar θ. As a result, the expression of θ through R_c/H is logical.

Very low wave heights (large R_c/H for constant R_c) result in a negative angle around $\theta = -20°$, as a result of the curvature. For higher waves, the increased run up causes an increase of θ. This is logical, as the lowest parts of the recurve have a negative ϕ (angle of PS relative to ground), while ϕ gradually increases for higher pressure sensors (Table A.5).

The angle θ gradually increases for decreasing R_c/H, till the point $R_c/H = 1.17$, after which impacts occur and θ has an approximately steady mean value of 25.14°. Interestingly, experiments with $R_c/H \approx 1.4$ are located around zero, which are the experiments $R13, R23, R33$ during which the area under the recurve is mostly filled up (Figures 3.5g, 3.5h, 3.5i). The fit functions in this graph are provided in Equations 3.10a and 3.10b, and the transition point $\frac{U}{R_c/H} = 1.17$ is defined as the crossing point of these to equations.

$$\theta = \begin{cases} \alpha_{\theta 1} & R_c/H < 1.17 \quad (3.10a) \\ \alpha_{\theta 1}\left(R_c/H\right)^{\alpha_{\theta 2}} + \alpha_{\theta 3} & R_c/H \geq 1.17 \quad (3.10b) \end{cases}$$

Where $\alpha_{\theta 1}$ $[-]$, $\alpha_{\theta 2}$ $[-]$ and $\alpha_{\theta 3}$ $[-]$ are fit coefficients as given in Table 3.7, F $[N]$ is the force, H $[m]$ is the wave height, U $[-]$ the *Ursell* number and R_c $[m]$ the crest freeboard.

Table 3.9: Mean values $\mu(\alpha_\theta)$ and standard deviation $\sigma(\alpha_\theta)$ of fit coefficients of force angle.

Coefficient	$\mu(\alpha_\theta)$	$\sigma(\alpha_\theta)$
$\alpha_{\theta 1}$	25.14	6.94
$\alpha_{\theta 2}$	82.14	5.00
$\alpha_{\theta 3}$	−3.78	0.42
$\alpha_{\theta 4}$	−21.20	1.76

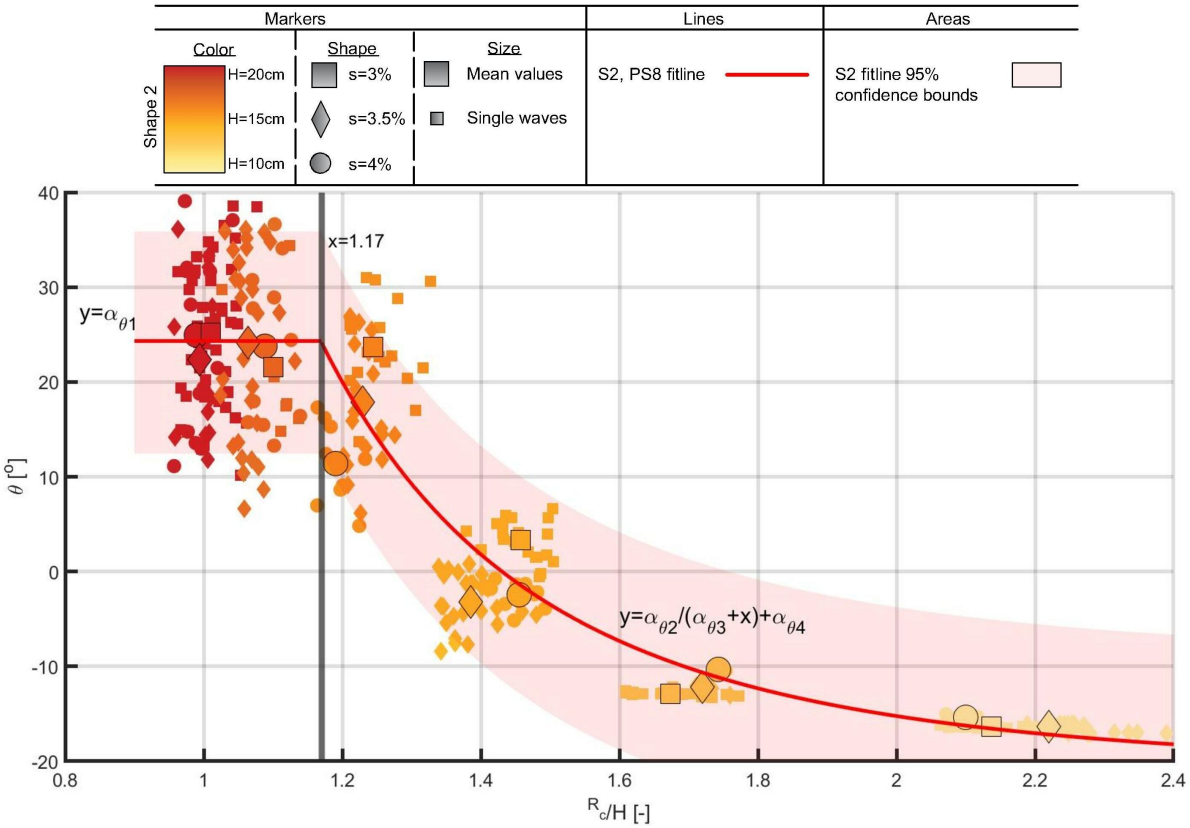

Figure 3.11: Scatter plot of force angle θ against $\frac{U}{R_c/H}$ for single wave events (small markers) and mean values per experiment (larger markers); red-yellow spectrum colors symzolize experiments performed with S2; light and dark colors distinguish between different wave heights ($H = 10cm - H = 20cm$ respectively); wave target steepness of 4%, 3.5% and 3% is symbolized with circles, diamonds and squares respectively; the fit results are presented as solid lines with their 95% confidence intervals as light shaded red areas.

4

Discussion

In order to give a better sense of how the two shapes compare, Figure 4.1 presents the results regarding mean values of maximum pressure and overtopping per wave for $S1$ and $S2$. The left y axis shows the rate of mean overtopping decrease per wave state, $\frac{V_{S1}-V_{S2}}{V_{S1}}[-]$, while the right y axis shows the rate of increase of mean maximum pressure per wave state, $\frac{P_{S2}-P_{S1}}{P_{S1}}[-]$. V_{S1}, V_{S2}, P_{S1} and P_{S2} are the mean values of single wave events of overtopping and maximum pressure per wave state, for the vertical wall and the crownwall.

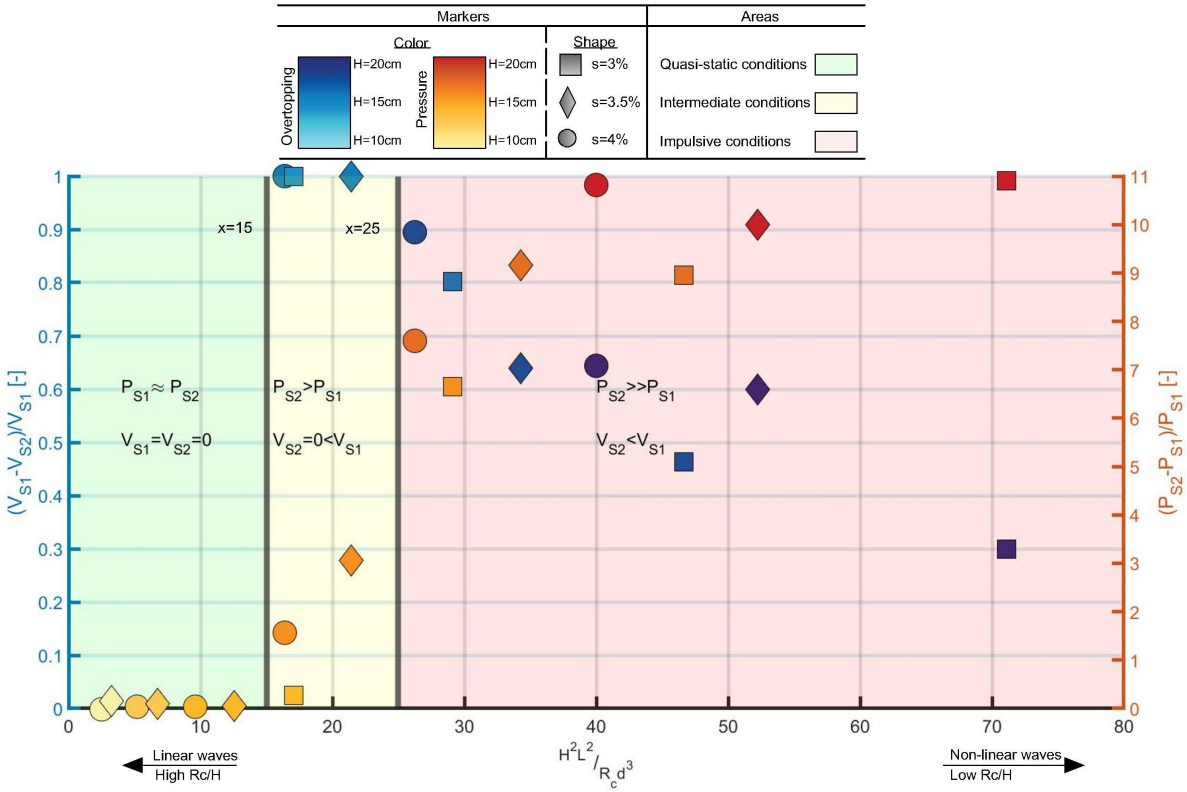

Figure 4.1: Scatter plot showing the rate of overtopping decrease $\frac{V_{S1}-V_{S2}}{V_{S1}}[-]$ on the left axis and rate of pressure increase $\frac{P_{S2}-P_{S1}}{P_{S1}}[-]$ on the right axis, as a result of the crownwall. Blue spectrum colors symbolize the decrease of overtopping volume, while red spectrum colors the increase of pressure; light and dark hues distinguish between different wave heights; wave target steepness of 4%, 3.5% and 3% is symbolized with circles, diamonds and squares respectively;

The domain is roughly divided in three sections. The first one for $\frac{U}{R_c/H} < 15$ includes low wave states which apply low quasi-static loads and overtopping occurs for neither $S1$ or $S2$. The second one for $15 < \frac{U}{R_c/H} < 25$ includes the intermediate wave states which barely reach the edge of the recurve. These wave states result in

overtopping for $S1$, while for $S2$ no overtopping occurs and a peak appears in the pressure signal. The third area for $\frac{U}{R_c/H} > 25$ includes higher wave states for which impacts and overtopping occur for $S2$.

Figure 4.1 shows that for $\frac{U}{R_c/H} < 15$, no overtopping occurs for either $S1$ or $S2$. The design of a crownwall for extreme conditions in this interval does not make sense, since the purpose of a crownwall by definition is to further reduce overtopping. Higher values between $15 < \frac{U}{R_c/H} < 25\,[-]$ result in 100% reduction of the overtopping volume, meaning that for the specific wave states, overtopping occurs only for $S1$. On the other side, for $\frac{U}{R_c/H} > 25\,[-]$ the rate of overtopping reduction gradually becomes smaller as the crownwall loses its effectiveness to block high waves. This means that designing a crownwall to operate for $\frac{U}{R_c/H} < 25\,[-]$ is optimal in terms of overtopping. Regarding the rate of pressure increase, the quasi-static loading for $\frac{U}{R_c/H} < 15[-]$ leads to almost no change in the mean maximum pressure. For $15 < \frac{U}{R_c/H} < 25\,[-]$ this changes as there is an increase of the mean maximum pressure of the wave states belonging in this interval up to a factor of 3. The magnitude and the quasi-trapezoidal pressure distribution of these wave states (Figures Figure 3.5g, Figure 3.5h and Figure 3.5i) shows that these wave states are a transitional state between impulsive and quasi-static loading. Therefore, this interval is not considered a threat to the stability of the structure. For $\frac{U}{R_c/H} > 25[-]$, the most severe wave loading results in an increase of the mean maximum pressure by a factor of 11 as a result of the impacts. Taking both aspects into account, a crownwall of this type should be designed to operate in the interval $0 < \frac{U}{R_c/H} < 25[-]$, while higher values should be reached only during extreme wave conditions.

In order to properly apply the equations of pressure (Equation 3.2) and overtopping (Equation 3.1) for these values, certain limitations should firstly be defined. The expression of these variables through $\frac{U}{R_c/H}$ is convenient because it combines the effect of the different applied values of wave steepness $s = H/L$ and wave height H, while it includes the effect of relative freeboard R_c/H as well. For example, using the variables s or R_c/H or d/L or U alone to express either V or P does not provide complete information regarding the characteristics of a wave (H,L) and their relation to the crest freeboard (R_c). At this point, it should be mentioned that the application range of these equations does not identify with their limits expressed through $\frac{U}{R_c/H}$. The $Ursell$ number can be broken down into $U = \frac{H/L}{(d/L)^3} = \frac{s}{(d/L)^3}$, leading to the dimensionless number $\frac{U}{R_c/H} = \frac{s}{(d/L)^3(R_c/H)}$. This means that all these three dimensionless numbers with their examined ranges $s = 3-4\%$, $d/L = 0.07-0.20$ and $R_c/H = 1-2$ should be considered in order to properly describe the applicability range of these equations.

The extreme example of a tidal wave ($s = 0\%$) with a low wave height e.g. $H = 4cm$, $L = 15330km$ is assumed. For the specific case of $R_c = 20cm$ and $d = 50cm$, $\frac{U}{R_c/H} \approx 10^{11}$ which leads to unreasonably high overtopping volume and pressure if applied in Equation 3.1 and Equation 3.2. The wave though is not expected to even reach the tip of the structure because $R_c/H = 0.2/0.04 = 5$, which highlights the need to set a limit for the relative freeboard. The value of the lowest overtopping wave is $R_c/H \approx 1.40$ for both shapes, which is suggested as the limit for the application of these equations. This ensures that only waves that reach the tip of the recurve are considered. On the other side, take the example of a wave with a large wave height and short wave length e.g. $s = 14\%$, $H = 25cm$, $L = 1.79m$, leading to $R_c/H = 20/25 = 0.8 < 1.40$. This ratio shows that this wave is expected to generate impacts and overtopping, but using these values with $\frac{U}{R_c/H} \approx 7.91$ leads to extremely low overtopping and pressure. As a conclusion, these formulas can not be applied outside the experimental limits of steepness $s = 3-4\%$. In addition, these equations are highly sensitive to water depth changes as $V \sim 1/d^3$ and $P \sim tanh(1/d^3)$. This means that application of these formulas outside the experimental range $d/L = 0.07-0.20$ leads to large errors; waves with $d/L < 0.07$ are almost broken waves which are not part of this study, while increasing values of $d/L > 0.20$ lead to decreasing overtopping volumes and pressure, which does not make sense.

These equations are derived and meant to be used for individual waves. Nevertheless, they can be used for irregular wave fields as well by using the largest wave height of the spectrum. This is known to be approximately $H_{max} = 1.89H_s$ for a *Rayleigh* distributed irregular wave spectrum. Using H_{max} as an input in these equations can estimate the load or overtopping volume of the highest wave.

As an example, an imaginary vertical breakwater is assumed, with $d = 10m$, which is designed for an Ultimate Limit State (ULS) with $H_{s,ULS} = 2.5m$ and a Serviceability Limit State (SLS) of $H_{s,SLS} = 1m$. This means that the maximum expected wave is $H_{max,SLS} \approx 1.89H_{s,SLS} = 1.89m$ and $H_{max,ULS} = 4.72m$ respectively. A peak steepness of $s = 2\%$ is assumed for both states, which translates to a steepness of the maximum wave approximately $s = 3.78\%$. The values of this imaginary setup are picked so that the maximum wave corresponds to the limits of $s = 3-4\%$ and $d/L = 0.07-0.20$. For maximum efficiency, the SLS can be defined at the limit which impact and overtopping occur for $S2$, or $R_c/H = 1.40 \Rightarrow R_c = 2.68m$. For an acceptable over-

topping volume of $5m^3/m$, the R_c for ULS can be defined by using the formula for overtopping, leading to $R_{c,S1} = 8.62m$ and $R_{c,S2} = 6.61m$. The $\frac{U}{R_c/H}$ values for these cases are 42.4 and 52.75 respectively. The selection of $S2$ and $R_{c,S2} = 6.61m$ leads to $P_{max,ULS} \approx 400kPa$ and $R_c/H_{max,SLS} = 3.5$, meaning that no overtopping is anticipated for the SLS.

Failure of hydraulic concrete structures most often happens abruptly, meaning that the approach of using the single maximum expected wave is convenient. A crownwall usually fails as a result of an individual wave event applying a large load on the structure and happens momentarily, not over time. On the other hand, the overtopping phenomenon is usually studied over time and the overtopping volume of the single maximum wave cannot properly describe this process. Actual sea states are irregular, and the individual overtopping volume of the maximum wave cannot properly express the effectiveness of the crownwall during a storm that may last several hours. As a result, further research is suggested to be done primarily on irregular waves. The importance of overtopping in defining the crest freeboard was already highlighted above, while an irregular wave approach can give results that resemble much better actual sea states. As $H_{max} \approx 1.89H_s$, it is suggested that irregular tests are carried for the same wave steepness and a significant wave height half of the regular wave heights applied in this study. The aforementioned application ranges of the equations highlight the need of investigation of different ranges of wave steepness (e.g. $s < 2\%$ or $s > 4\%$), relative water depth ratios (e.g. $d/L > 0.20$) and relative freeboard ($R_c/H < 1$). In addition, a very specific shape of crownwall is studied, meaning that possible derivation from this geometry may affect the load magnitude and distribution. The comparison of the equation by Castellino et al. (2021) with the results of pressure, shows a maximum 45% increase of the load on the crownwall compared to a recurved parapet. Thus, the investigation of different recurve radius or overhang length that can lead to a more effective shape could be interesting. Lastly, the effect of directional waves is not considered in this manuscript. Extension of this study to this aspect that exists in real sea states can help in a more complete understanding of the associated phenomena.

5

Conclusion

This thesis presents the experimental results of a crownwall with a fully curved face and a vertical wall subjected to non-breaking wave loading. Several analyses are performed in order to describe the behavior of this type of crownwall in terms of overtopping and loading. The final aim of this manuscript is to gain better understanding of this type of crownwall and provide tools to calculate the studied variables. The research question that was set in Chapter 1 is:

"How does a crownwall with a fully curved face perform in comparison with a vertical wall, in non–breaking wave conditions and in terms of loading and overtopping?"

Which can further be broken down in two sub-questions.

"What equations can be used to predict overtopping and loading on a crownwall with a fully curved face?"

Several equations are derived for the crownwall that can be employed to calculate the individual overtopping volume V, maximum pressure P, impulse I, impulse duration t_{imp}, force F, force angle θ and point of application ζ.

The reflection coefficient K_r of the crownwall is found to have an approximately constant value of $K_r \approx 0.92$. For $R_c/H < 1.20$, there is a gradual reduction of K_r as a result of overtopping. As this variable drops only in cases of overtopping, it means that it is dominated by wave run-up and wave height. This means that the dimensionless numbers d/L and s are not relevant, and the value $K_r = 0.92$ can be applied for $d/L > 0.07$ and irregardless of s.

The overtopping analysis shows that the effectiveness of the crownwall in blocking overtopping volumes is limited, as the results of the two shapes tend to align for high $\frac{U}{R_c/H}$ values (Figure 3.3). Equation 3.1 can be used to estimate the expected overtopping volume of an individual wave, within the ranges of $R_c/H < 1.40$, $0.07 < d/L < 0.20$ and $s = 3-4\%$.

The results of pressure (P) regarding $S2$ and for $\frac{U}{R_c/H} < 14.9$ lead to quasi-static loads that can be predicted very well by the *Goda* formula. For $\frac{U}{R_c/H} > 14.9$, the equation for recurved parapets by Castellino et al. (2021) is evaluated, showing that pressures generated on a crownwall with a fully curved face are up to 45% larger. For this interval, impacts occur and the trend of results can be described by Equation 3.2, which approximates the maximum pressure of a wave near the outer edge of the recurve for waves with $R_c/H < 1.40$, $0.07 < d/L < 0.20$ and $s = 3-4\%$. Alternatively, the upper limit of this equation, $P = \alpha_{p1}\rho g H$ can be used as an approximation of maximum pressure, as it only depends on H. This constant value is reached for $\frac{U}{R_c/H} > 60$,which is the case with $H = 20cm$ and $s = 3\%$. As a consequence, this equation is suggested to be used for $R_c/H < 1$, while values of $s < 3\%$ can be applied. Values of $s > 3\%$ are expected to give reasonable results and lead in a slight overestimation of pressure. This equation is not dependent on water depth, meaning that values of $d/L > 0.20$ can be applied as well.

For the cases where impacts occurred, impulses I are derived from the pressure signal and are found to follow a very similar trend to pressure results. Equation 3.4 can be used to describe this trend, which reaches a constant value of $I = \alpha_{I1}\rho g H T$ at $\frac{U}{R_c/H} \approx 20$ (Figure 3.7), which is considerably smaller than $\frac{U}{R_c/H} \approx 60$ mentioned above for pressure. This comes as a result of the shortening of the duration of the impulse for

increasing $\frac{U}{R_c/H}$ (Figure 3.8). In addition, the rising part of this equation for $\frac{U}{R_c/H} < 20$ refers to experiments that do not exhibit a fully impulsive pressure profile. The constant value is reached around a mean effective relative freeboard $R_c/H = 1.21 \approx 1.20$, which is suggested as a limit to use the equation $I = \alpha_{I1}\rho g H T$. This equation indicates that both wave height and wave period, thus wave steepness, influence impulses for the entire interval. Taking into account the linear dependency of I with H and T and the small scatter of the impulse results, these are strong indications that the formula $I = \alpha_{I1}\rho g H T$ can be used outside the experimental limit $s = 3-4\%$. This equation is independent of d^3, meaning that different non-breaking d/L ratios can be used as well. The results of impulses are found to be more stable compared to peak pressures. This shows the potential of using impulses to calculate loading (e.g. Chen et al., 2019), as their estimation is less uncertain compared to peak pressure.

The impulse duration t_{imp} is found to follow a hyperbolic trend (Equation 3.6), while t_{imp} gets shorter for increasing values of $\frac{U}{R_c/H}$. As t_{imp} is expressed through this variable and no constant value is reached, similar arguments as the case of overtopping can be made. This means that the limits of $d/L = 0.07-0.2$, $R_c/H < 1.40$ and $s = 3-4\%$ can not be violated.

The results of force F regarding the crownwall can be approximated by Equation 3.7 for $\frac{U}{R_c/H} > 14.7$, which reaches a constant value of F (Equation 3.7) for $\frac{U}{R_c/H} > 60$. As the force signal is derived by integration of the pressure signal, the same trend is followed and the same arguments can be made regarding s, d/L and R_c/H. Consequently, this equation can be used for $R_c/H < 1.40$, while the steady value of $F = \alpha_F \rho g H^2$ can be used for $R_c/H < 1$ as an upper limit estimation of the impulsive force . No equation is provided for cases without impacts, as this interval is irrelevant to design.

Table 5.1: Derived equations for crownwall with a fully curved face and application range. Valid application ranges are denoted with green while not valid ranges are denoted with red.

Variable	Equation	R_c/H 1	1.20	1.40	s 3%	4%	d/L 0.07	0.20
Reflection coefficient	$K_r = 0.92$							
Overtopping	$\frac{V}{(BH^2)} = \alpha_{q1}\left(\frac{U}{R_c/H}\right)^{\alpha_{q2}} + \alpha_{q3}$							
Pressure	$\frac{P}{\rho g H} = \alpha_{p1} tanh(\alpha_{p2}\frac{U}{R_c/H} - \alpha_{p3})$ $P = \alpha_{p1}\rho g H$							
Impulse	$\frac{I}{\rho g H T} = \alpha_{I1} tanh\left(\alpha_{I2}\frac{U}{R_c/H} - \alpha_{I3}\right)$ $I = \alpha_{I1}\rho g H T$							
Impulse duration	$\frac{t_{imp}}{T} = \frac{\alpha_{t1}}{\frac{U}{R_c/H}+\alpha_{t2}}$							
Force	$\frac{F}{\rho g H^2} = \alpha_{f2} tanh\left(\alpha_{f3}\frac{U}{R_c/H} - \alpha_{f3}\right)$ $F = \alpha_{f2}\rho g H^2$							
Force point of application	$\zeta = \alpha_{\zeta 1}$ $\zeta = \alpha_{\zeta 2}\left(R_c/H\right)^{\alpha_{\zeta 3}} + \alpha_{\zeta 4}$							
Force angle	$\theta = \alpha_{\theta 1}$ $\theta = \alpha_{\theta 1}\left(R_c/H\right)^{\alpha_{\theta 2}} + \alpha_{\theta 3}$							

The point of application of the force ζ for $S2$ can be approximated by Equation 3.9a and 3.9b , which show that ζ tends to attain a constant mean value for decreasing R_c/H, around $\zeta \approx 0.55 R_c$. The angle of application of the force relative to SWL (Figure 2.12) is found to be $\theta = -19°$ upward from horizontal for $R_c/H \approx 2.2$,

which increases and reaches a steady mean value, around $\theta \approx 25.1°$. Equations 3.10a and 3.10b can be used to calculate θ and decompose the total force acting on the crownwall to its tangential components, F_x and F_z. These equations show that the point and angle of application have a steady value for very high wave loads ($R_c/H < 1.17 \approx 1.20$) and are suggested to be used for non-breaking waves regardless of s and d/L. The combination of these equations can give a complete description of the total applied force and be used to predict the behavior of the crownwall against typical failures such as overturning. An overview of the equations with the suggested limitations is given in Table 5.1.

"How can the results from these equations be compared to a vertical wall?"

In order to provide tools for comparison, experimental results of a vertical wall regarding the variables K_r, V, P, F and ζ are presented in this study.

The analysis of the wave characteristics shows a steady mean reflection coefficient for $R_c/H > 1.20$, with a value of $K_r = 0.94$. Lower values lead to a gradual reduction of the reflection coefficient while the lowest measured mean value is $K_r = 0.83$.

Equation 3.1 can be used to calculate overtopping on a vertical wall and compare it to a crownwall with a fully curved face. The results of overtopping follow a very similar trend to $S2$, meaning that the same limitations regarding s, R_c/H and d/L hold here as well.

Regarding loading, the formula of $Goda$ is evaluated, which is found to predict accurately pressure at SWL. Application of this formula for higher positions of the wall leads to an underestimation of pressure up to 25% for the worst loading case. The results of pressure tend to acquire a constant $P/\rho g H$ value (Figure 3.6), which shows again the dominance of wave height in this phenomenon. The employment of this formula to calculate F and ζ results in a slight underestimation of both variables, which is related to the aforementioned underestimation of pressure at higher positions. Nevertheless, taking into account its range of applicability, the use of the *Goda* formula is suggested to estimate loading on a vertical wall. ζ is found to acquire a constant mean value for $R_c/H < 1.17$, $\zeta_{S1} \approx 0.46$. This is considerably lower than the value calculated for $S2$, $\zeta_{S2} = 0.55R_c$, and leads to a larger overturning moment on the structure. An overview of the derived an evaluated equations is presented in Table 5.2.

Table 5.2: Derived and evaluated tools for calculating the load and overtopping on a vertical wall.

Variable	Equation	Comments
Reflection coefficient	$K_r = 0.94$	see Table 5.1
Overtopping	$\frac{V}{(BH^2)} = \alpha_{q1}\left(\frac{U}{R_c/H}\right)^{\alpha_{q2}} + \alpha_{q3}$	see Table 5.1
Pressure	Goda	Accurate at SWL. Accuracy decreases for higher positions.
Force	Application of Goda formula	Underestimates forces.
Force point of application	Application of Goda formula	Slightly underestimates for $R_c/H < 1.17$
Force angle	0	-

A

Lab set-up

A.1. Force, Moment and Pressure Transducers

Initially, the superstructure was divided into three parts with widths of 0.32 m, 0.15 m and 0.32 m and a force and a moment sensor were mounted under the superstructure. Eventually it was not possible to retrieve results from them, but the procedure for selecting the sensors and the rest of equipment is also a part of this study and is explained below.

Numerical simulation experiments similar to the performed experiments were performed by *Rome University of Sapienza*. Table A.1 shows the provided maximum force generated on the crownwall calculated from these numerical simulations. $q_{y,max}$ $[N/m]$ is the vertical component of the force, $q_{x,max}$ $[N/m]$ is the horizontal component while x_G and ζ_G are the coordinates of the point of application of the force with a reference point the outer, lowest seaward point of the crownwall (Figure A.1, blue dot).

Table A.1: Maximum forces and coordinates of point of application of the force.

Geometry	$q_{x,max}[N/m]$	x_G [cm]	$q_{H,max}$ [N/m]	ζ_G [cm]
Shape A	0	0	358	8.8
Shape B	770.1	5.4	2173.4	12

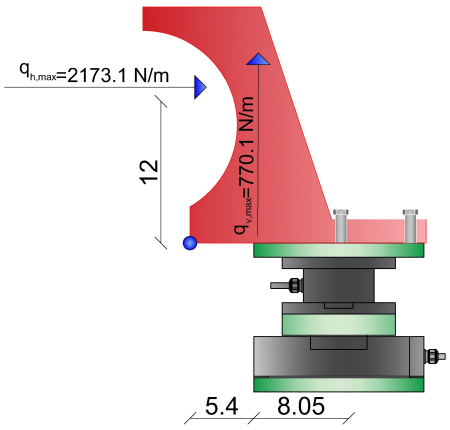

Figure A.1: Calculation of expected maximum force and moment

The maximum expected total horizontal $F_{x,max}$ $[N]$ and vertical $F_{z,max}$ $[N]$ force are calculated by multiplying $q_{x,max}$ $[N/m]$ and $q_{y,max}$ $[N/m]$ with the crownwall middle section width, equal to 0.15 m. The maximum expected moment M_{max} is calculated as shown in Equation A.1.

$$M_{max} = F_{z,max} \times 8.05/100 + F_{x,max} \times 12/100 \tag{A.1}$$

The results of the above procedure are shown in Table A.2.

Table A.2: Expected maximum force and moment.

Geometry	$F_{V,max}[N/m]$	$F_{h,max}[N]$	$M_{max}[Nm]$
Shape A	0	53.7	4.73
Shape B	115.51	330	48.90

Taking into account that $F_{x,max} = 330\,N$ and $M_{max} = 48.90\,Nm$, *K3D120-500N* and *TQ-D2553* force and moment transducers are selected, as their 500 N and 50 Nm limit is reasonably higher.

In addition to the above, initially a hammer impact test was planned, which was not performed in the end. For the middle section of the crownwall, it has to be ensured that there would be a large numerical difference between the natural frequency of the superstructure and the frequency of the impulse. For this reason, the frequency of the impulses was provided from *Rome university of Sapienza* as well. The values of the impulse duration are shown in Table A.3 .

Table A.3: Numerical simulation results of impulse duration for wave steepness $s = 3\%$ and $s = 4\%$ and $H = 0.18\,m$, $H = 0.20\,m$ and $H = 0.22\,m$.

Wave Height [m]	$f_{s=3\%}[Hz]$	$f_{s=4\%}[Hz]$
0.18	5.03	7.1
0.2	4.74	5.68
0.22	4.63	4.90

The stiffness (k) of the force and moment transducers is calculated by dividing the instruments rated force F_x and M_x by the rated displacement ϵ_x and ϵ_z.

$$k_x = \frac{F_x}{\epsilon_x} = \frac{500N}{0.06mm} = 8.3 \times 10^6 N/m \tag{A.2}$$

$$k_{rot} = \frac{M_z}{\epsilon_z} = \frac{200Nm}{0.0010rad} = 1.97 \times 10^5 Nm/rad \tag{A.3}$$

Lastly, in order to calculate the natural frequencies of the crownwall, the total mass of the structure is calculated. This is done by calculating the crownwalls cross section area A_{Cr} and contributing water mass cross section area A_w (Figure A.2). A_{Cr} and A_w are multiplied with the middle sections width 0.15 m to calculate the volume of the crownwall's middle section V_{Cr} and contributing water mass volume V_w. Multiplying these values with their respective densities $\rho_{Cr} = 1400\,kg/m^3$ and $\rho_w = 1000\,kg/m^3$ results in the masses m_{Cr} and m_w. The two masses are added to calculate the total mass of the middle section m_{tot}. This is demonstrated in Table A.4.

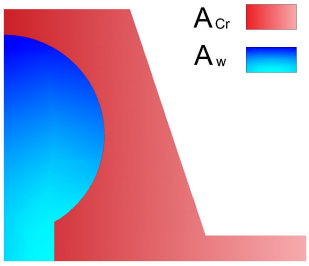

Figure A.2: Graphical representation of A_{cr} and A_w

Table A.4: Calculation of total mass m_{tot}. A is the cross section surface, V is the middle section volume, m is the mass while the indexes Cr, w and tot mean "crownwall", "water" and "total" respectively

Geometry	$A_{Cr}[m^2/m]$	$A_w[m^2/m]$	$V_{Cr}[m^3 \times 1000]$	$V_w[m^3 \times 1000]$	$m_{Cr}[kg]$	$m_w[kg]$	$m_{tot}[kg]$
A	0.028	0	4.26	0.00	5.75	0.00	5.75
B	0.030	0.011	4.46	1.65	6.01	1.65	7.66

The natural frequency of the structure is calculated as shown in Equations A.4 and A.5.

$$f_{n,x} = \frac{1}{2}\pi\sqrt{\frac{k_x}{m_{tot}}} = 2055.5Hz \tag{A.4}$$

$$f_{n,rot} = \frac{1}{2}\pi\sqrt{\frac{k_{rot}}{m_{tot}}} = 251Hz \tag{A.5}$$

As the difference between $f_{n,rot} = 251Hz$ and the maximum expected impulse frequency $f_{imp,max} = 7.1Hz$ is around $251 - 7.1 \approx 244Hz$, the selection of the instruments is considered acceptable.

Eight *HKM-375(M)* pressure transducers are used in total, the positioning of which is shown in Figure A.3. Their orientation relative to the ground (ϕ) and the integration areas used for the calculation of forces (A) are given in Table A.5.

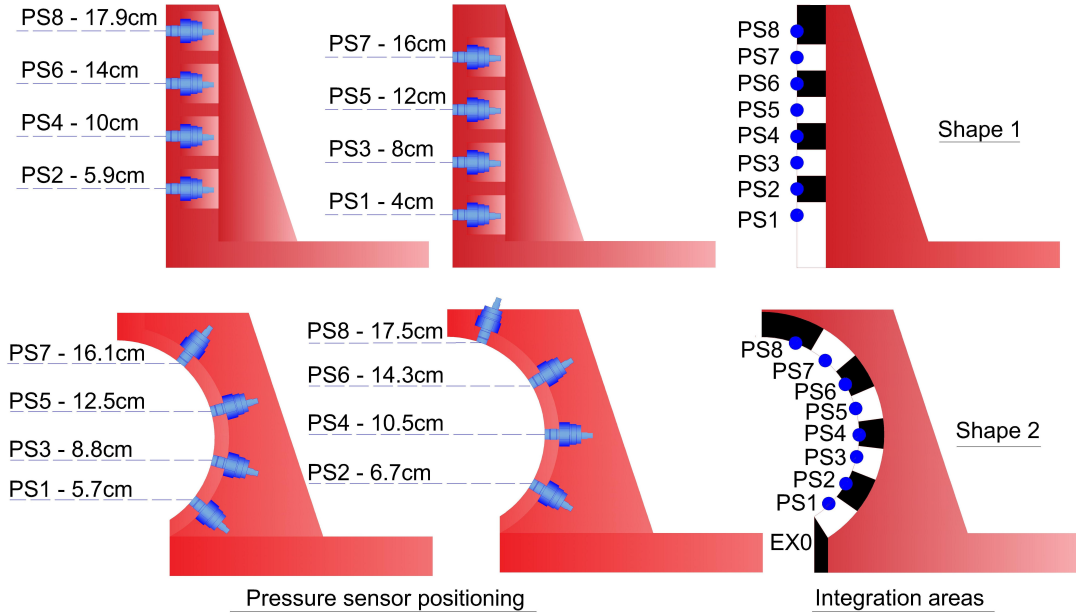

Figure A.3: Back view of the crownwall and cross sections showing the positioning of HKM-375(M) pressure transducers for Shapes A and B

Table A.5: Orientation of and length of integration areas.

Instrument	$\phi_{S1,j}$ [^{o}]	$A_{S1,j}$ [cm]	$\phi_{S2,j}$ [^{o}]	$A_{S2,j}$ [cm]
EX0	-	-	0	4.3
PS1	0	5.0	318.49	2.3
PS2	0	2.0	327.78	2.3
PS3	0	2.0	344.81	1.9
PS4	0	2.0	358.75	1.9
PS5	0	2.0	13.46	2.0
PS6	0	2.0	28.94	2.2
PS7	0	2.0	47.53	2.5
PS8	0	3.0	67.66	3.9

A.2. Calibration of instruments

The force and moment transducers calibration functions are retrieved by hanging a basket on the force sensor (Figure A.4a), and on an arm attached on the moment sensor (Figure A.4b). The maximum anticipated horizontal force and moment are $F_{x,max} = 330N$ and $M_{max} = 48.9\,Nm$ respectively. Therefore, the calibration is performed by slowly loading the sensors in 8 equally sized steps, for a maximum load of $35kg \times 9.81m/s^2 \approx 350$ N and $10kg \times 9.81m/s^2 \times 0.9m \approx 91Nm$. The volt indication V for each of the steps is retrieved, and the calibration function of each loading step is defined as $c_F = \frac{\Delta F}{\Delta V}$. The total calibration function of the instrument is defined as the mean value of the calibration function of each individual loading step.

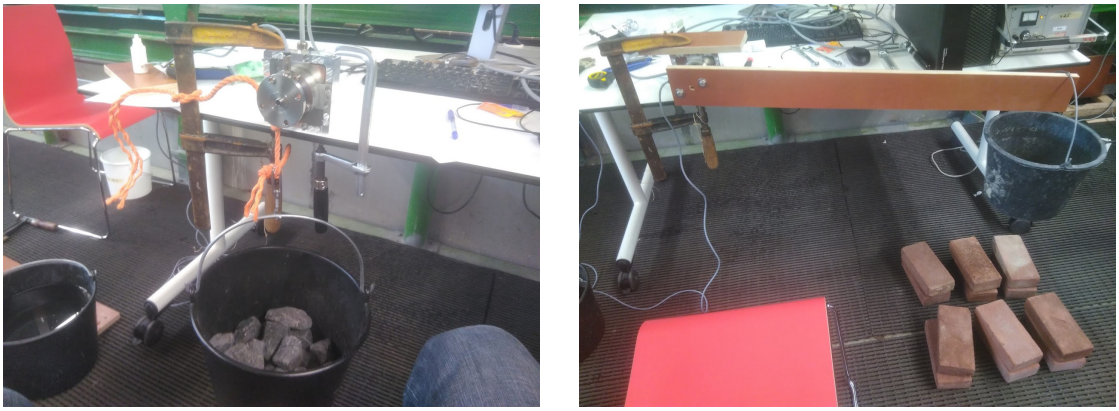

(a) Force sensor calibration.

(b) Moment sensor calibration.

Figure A.4: Setup of calibration of instruments.

The calibration functions of the wave gauges are derived by repositioning them vertically in water in 10 different vertical positions, covering all the allowable wave gauge range. The indication on the scale of the wave gauge is retrieved for each repositioning step. The calibration function for each step between the 10 positions is then calculated as $c_{WG} = \Delta x/\Delta V$, where Δx is the vertical displacement of the WG and ΔV the difference in volt indication. The calibration function of the WG is defined as the mean value of the calibration functions of the individual steps.

The calibration function of the pressure sensors is retrieved from the manufacturer. Lastly, the calibration of the wave pedal is performed similarly as the wave gauges, by placing a scale on the pedal, repositioning it and retrieving the vold indication for each repositioning step. The calibration functions of all instruments are shown below in Table A.6.

Table A.6: Callibration functions of instruments.

Instrument	Callibration	Units
$WG1$	2.31	$[cm/V]$
$WG2$	2.25	$[cm/V]$
$WG3$	2.24	$[cm/V]$
$WG4$	2.62	$[cm/V]$
$WG5$	2.38	$[cm/V]$
$WG6$	2.27	$[cm/V]$
$WG7$	-	$[-]$
$WG8$	2.66	$[cm/V]$
$WG9$	-4.38	$[cm/V]$
$PS1$	7471.43	$[Pa/V]$
$PS2$	7445.75	$[Pa/V]$
$PS3$	7456.62	$[Pa/V]$
$PS4$	7476.51	$[Pa/V]$
$PS5$	7441.55	$[Pa/V]$
$PS6$	7407.35	$[Pa/V]$
$PS7$	7450.94	$[Pa/V]$
$PS8$	7440.58	$[Pa/V]$
Wave Pedal	1.16	$[cm/V]$

A.3. Overtopping box

The overtopping box is made of wood and has a mouth width of $B = 0.112m$. A cross section of the overtopping box is shown in Figure A.5.

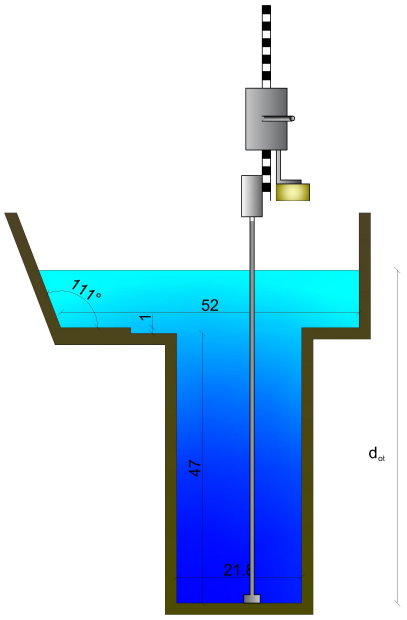

Figure A.5: Cross section of overtopping box, dimensions in *cm*.

The function converting the reading of $WG9$ in m to m^3 is given in Equations A.6a, A.6b and A.6c.

$$V = \begin{cases} 0.216 \times 0.128 \times d_{ot} & d < 0.47m \quad \text{(A.6a)} \\ 0.012995 + 0.296 \times 0.128 \times (d_{ot} - 0.47) & 0.47 \leq d < 0.48m \quad \text{(A.6b)} \\ 0.013373 + 0.19097 \times (d_{ot} - 0.48)^2 + (d_{ot} - 0.48) \times 0.52) \times 0.28 & d \geq 0.48m \quad \text{(A.6c)} \end{cases}$$

Where d_{ot} is the reading of the water depth as shown in Figure A.5. The functions are retrieved theoretically and confirmed by slowly filling the box with water in steps. For each of the steps, the water volume is weighted and the indication of a scale in the box is applied in Equations A.6a, A.6b, A.6c. The measured weight is formulated to volume by multiplying it with $\rho = 1000kg/m^3$, while the results of these two measurement procedures show a good agreement, as presented in Figure A.6.

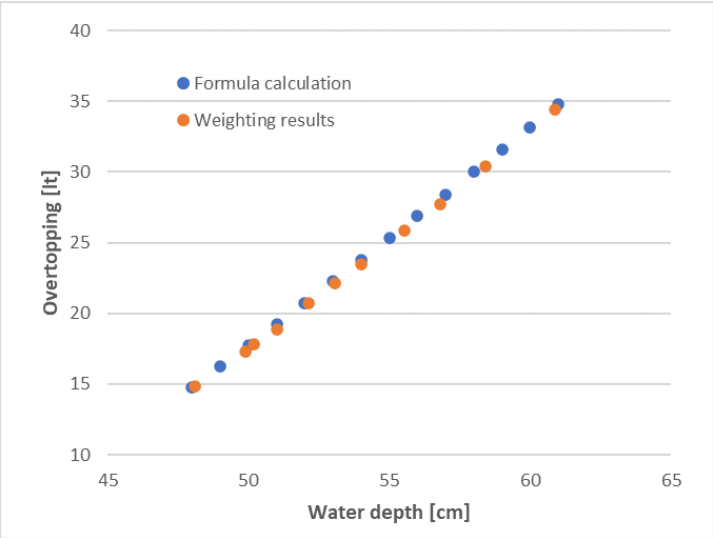

Figure A.6: Confirmation of overtopping box formula.

A.4. Design of Framework

As demonstrated in Chapter 2, an aluminium beams framework is used in order to support the superstructure. This structure is designed by taking into account the following:

- The superstructure is divided into 3 parts, therefore the framework is designed to be able to support all of them;
- A force transducer is mounted under the middle part of the superstructure, creating a gap of between the superstructure and the vertical wall;
- The maximum allowed displacement of the force and moment transducers is 0.06 mm and 0.01 mm respectively. Thus, the safety gap between flat vertical wall and the bottom part of superstructure is set to 0.5mm.
- A water tank is placed behind the crownwall in order to collect overtopping volumes, thus it is ensured that enough space is available on the back of the superstructure to fit the water tank;
- More beams than required to fix the crownwalls are used in order to increase the stiffness of the framework in order to ensure that small vibrations of the support structure do not have an evident effect on the sensor signals;

Figures A.7-A.20 present analytical drawings of the support structure.

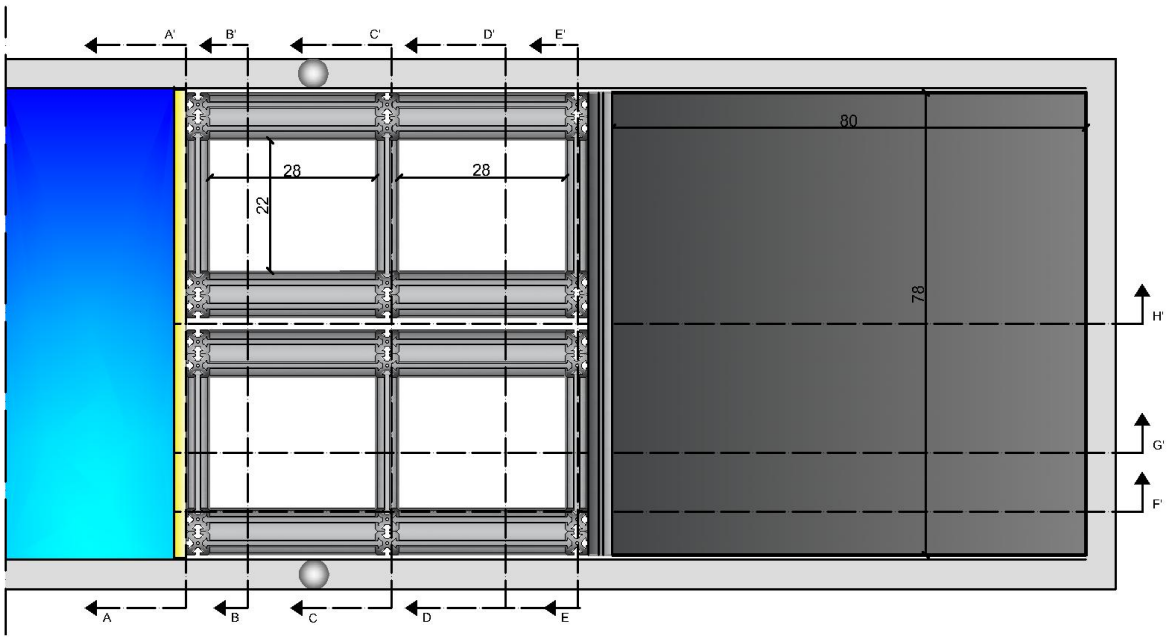

Figure A.7: Top view from z=15cm

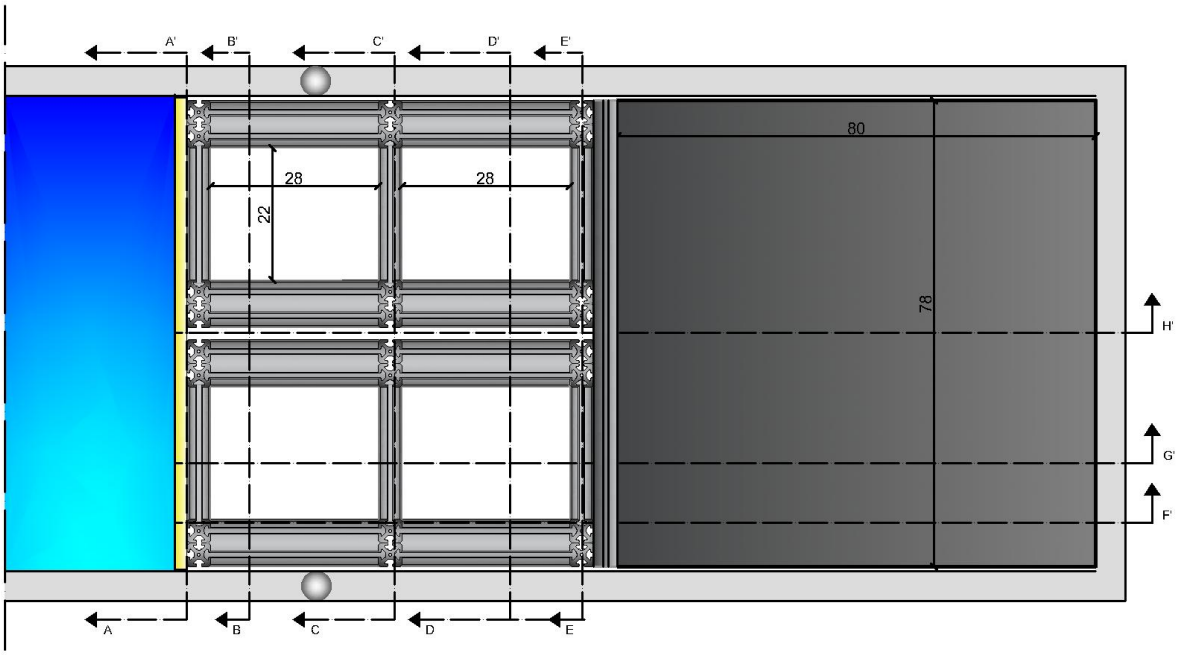

Figure A.8: Top view from z=30cm

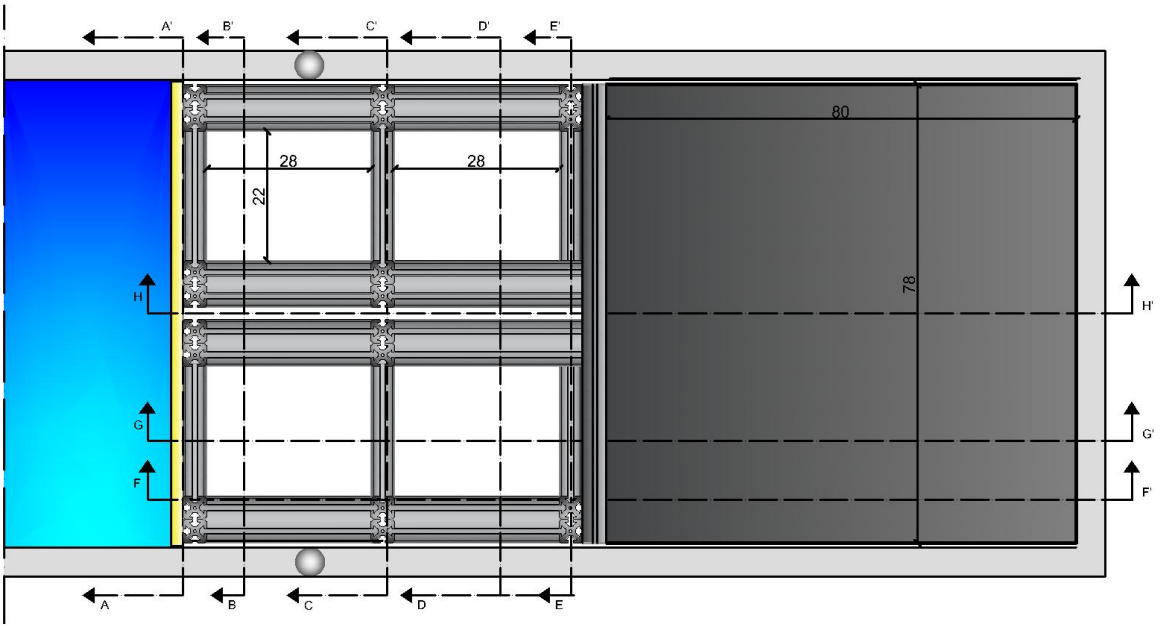

Figure A.9: Top view from z=45cm

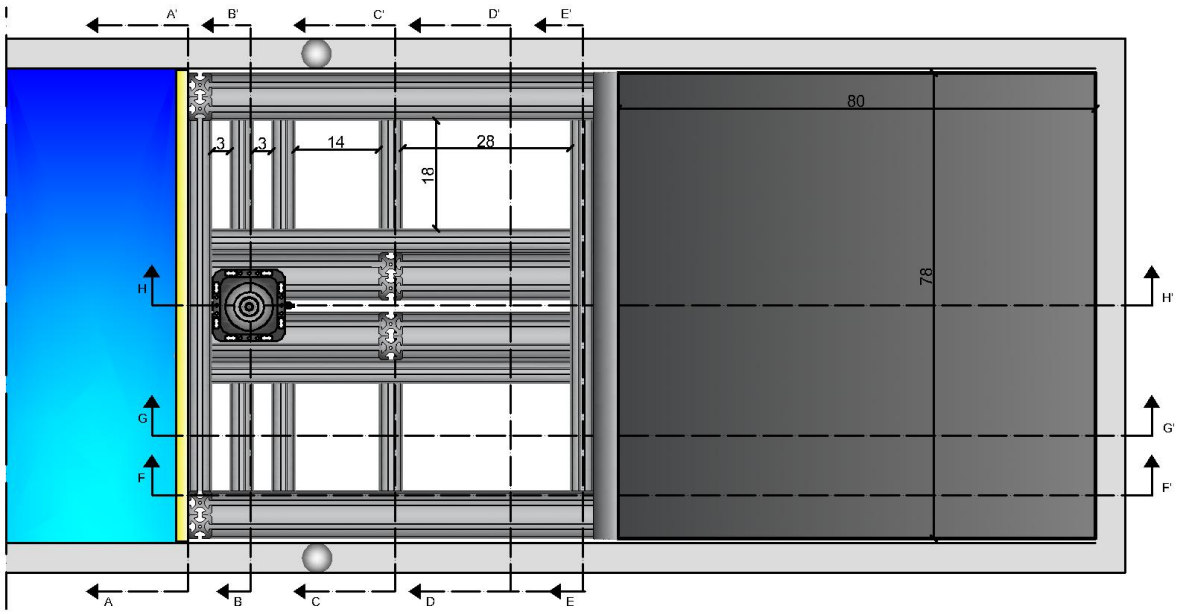

Figure A.10: Top view from z=50cm

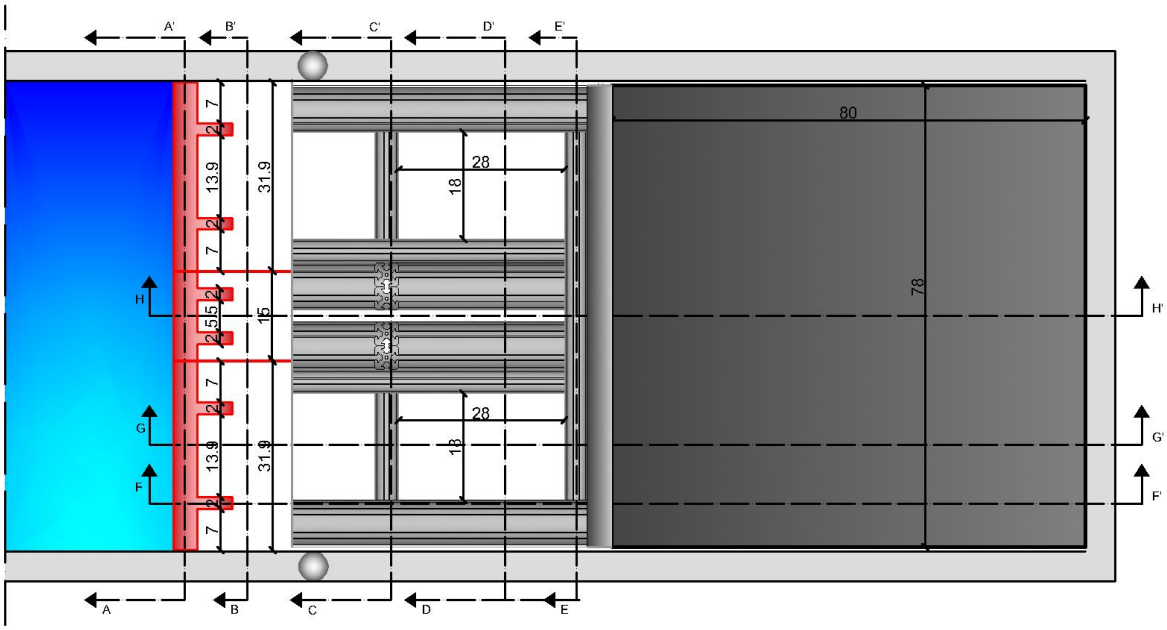

Figure A.11: Top view from z=52cm

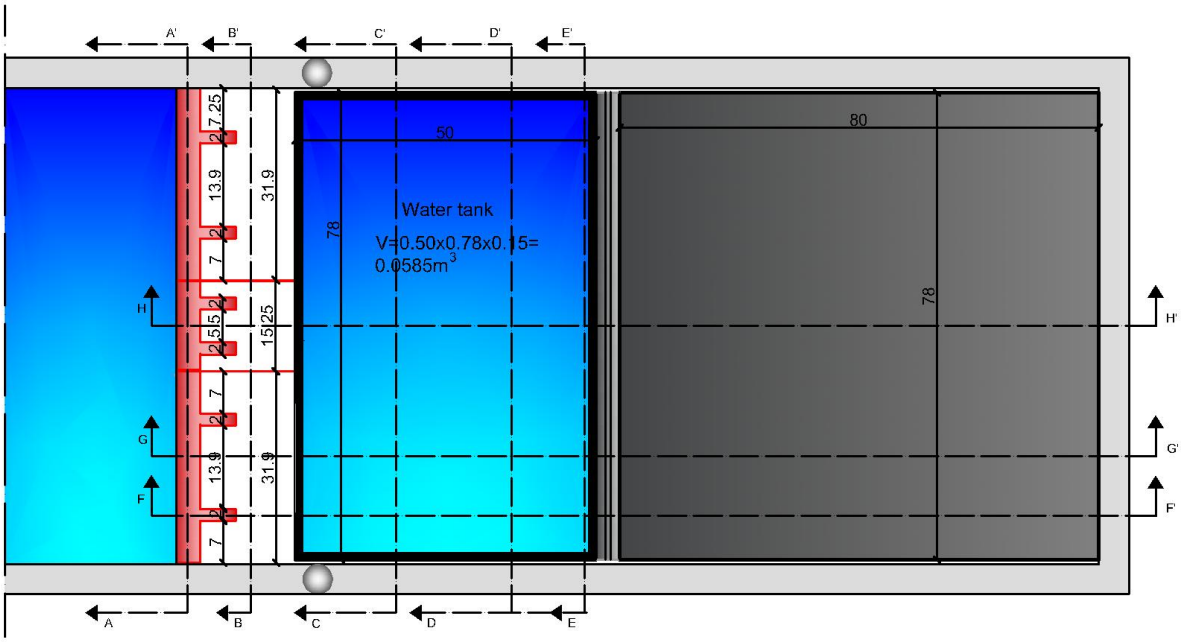

Figure A.12: Top view from z=70cm

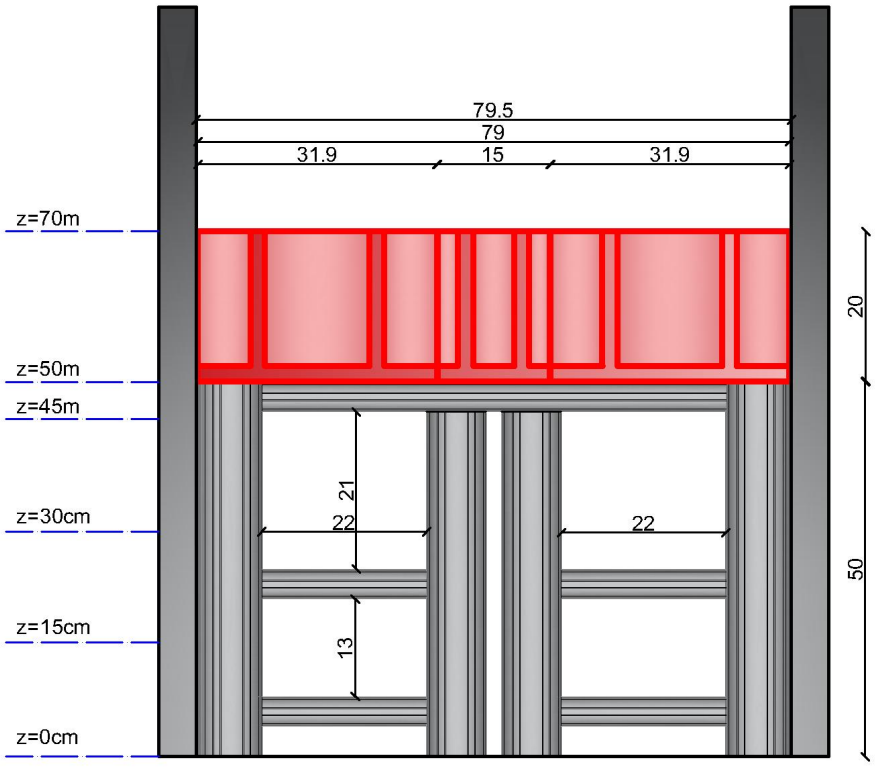

Figure A.13: Cross section A-A'

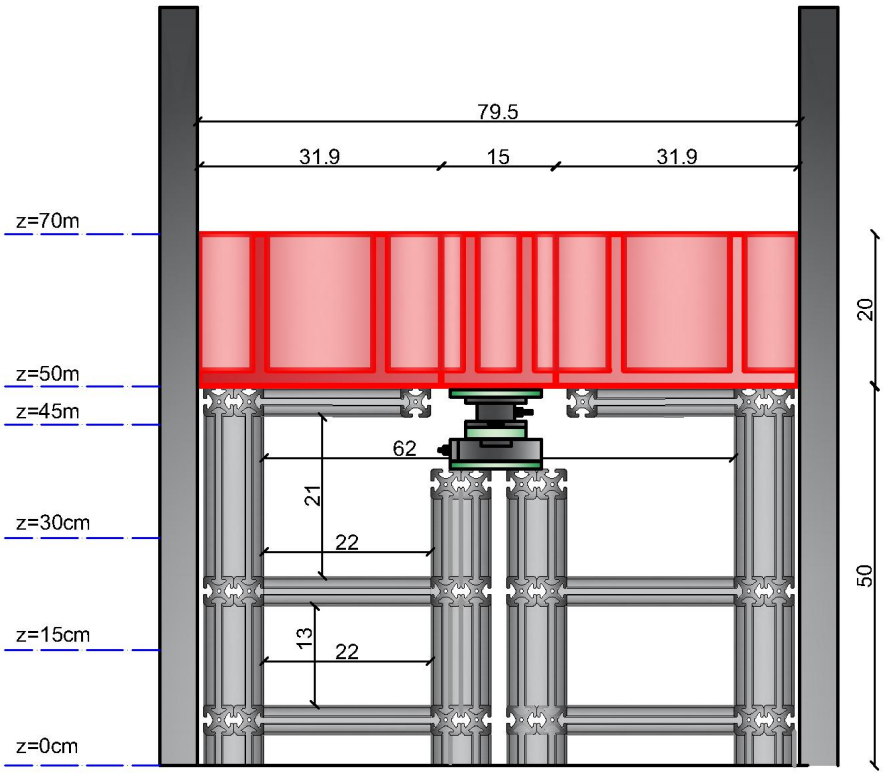

Figure A.14: Cross section B-B'

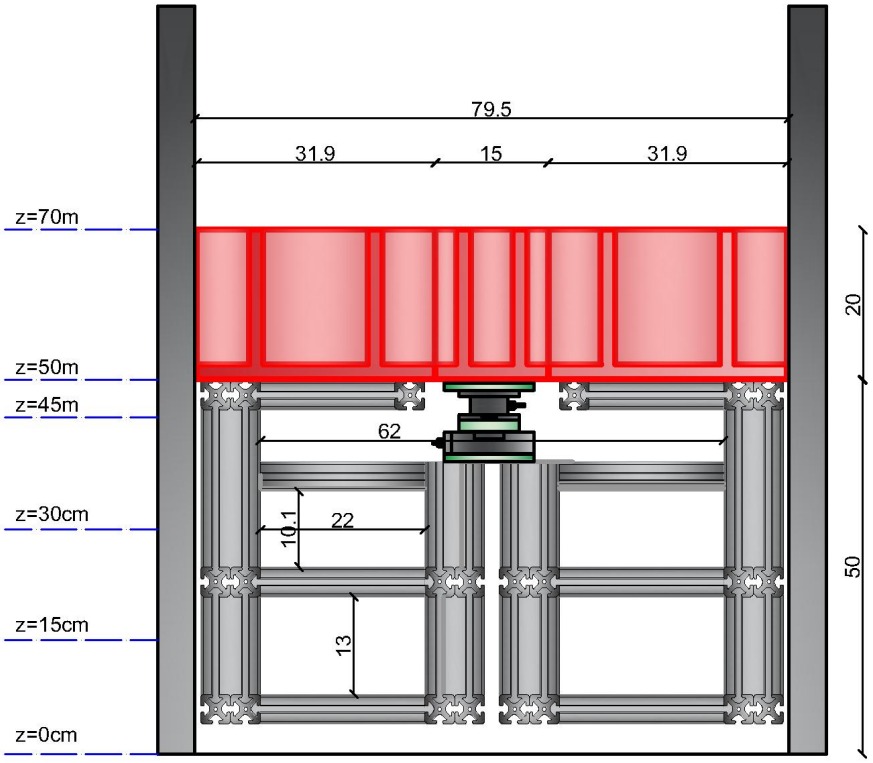

Figure A.15: Cross section C-C'

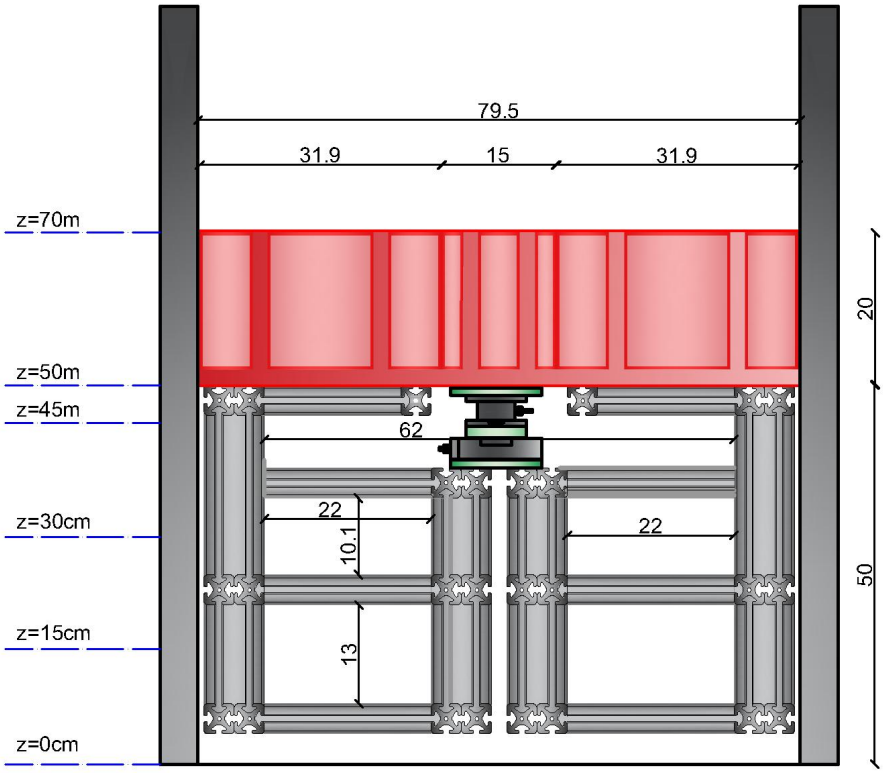

Figure A.16: Cross section D-D'

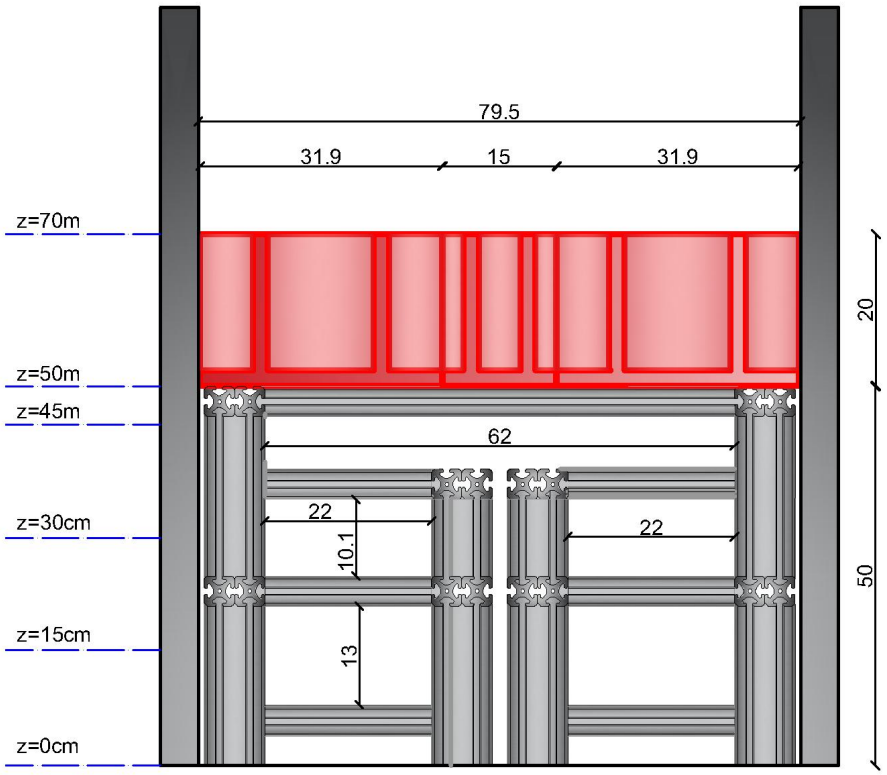

Figure A.17: Cross section E-E'

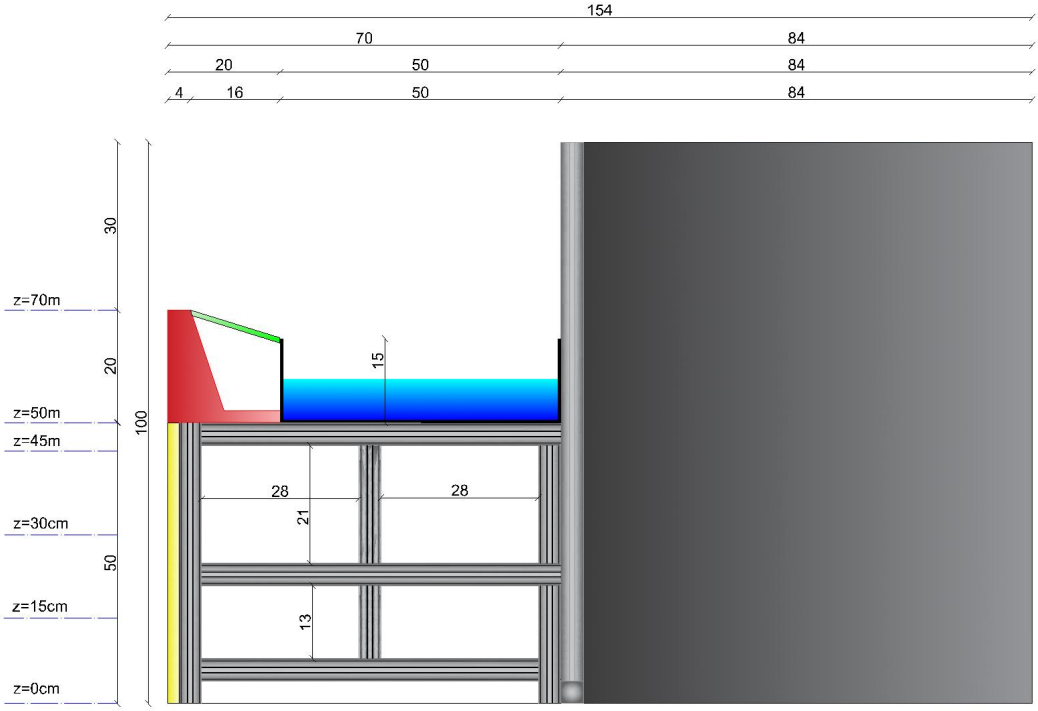

Figure A.18: Cross section F-F'

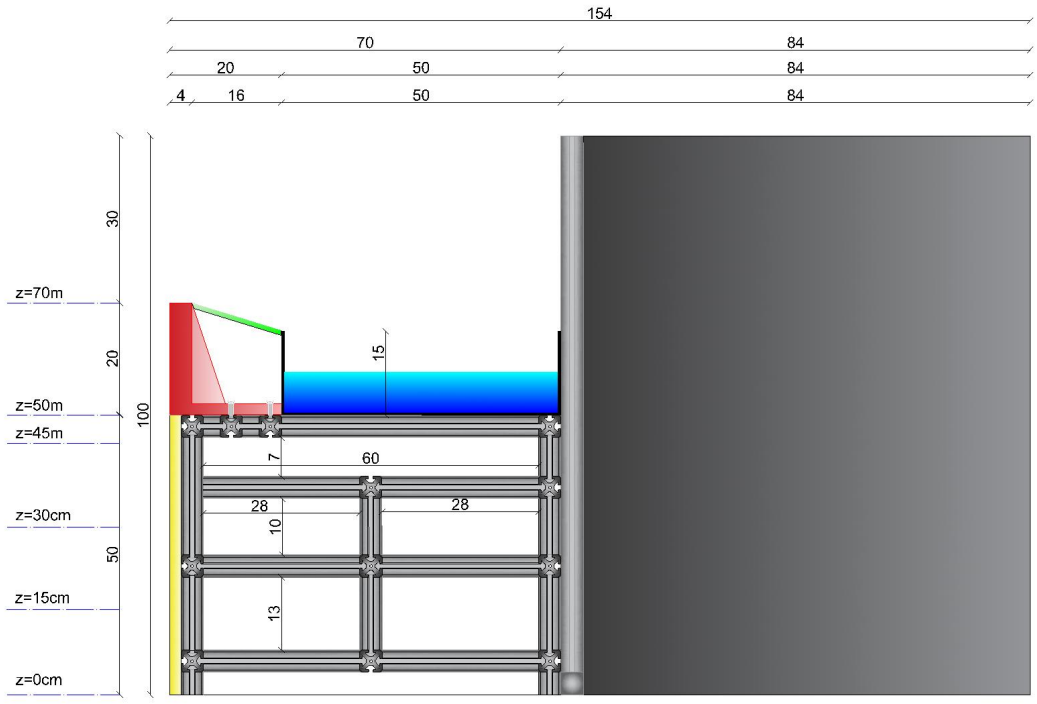

Figure A.19: Cross section G-G'

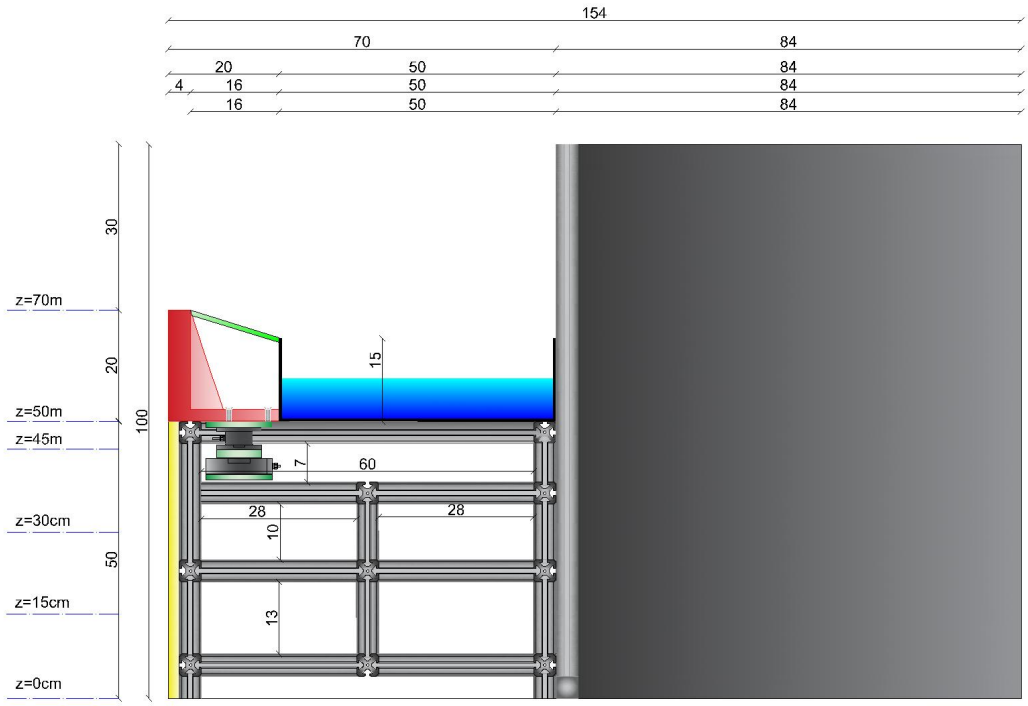

Figure A.20: Cross section H-H'

B

Methodologies

B.1. Goda method

The methodology for calculating pressures on a vertical wall by Goda (1974) is given below through Equations B.1-B.9.

$$\eta^* = 0.75(1 + cos\beta)\lambda_1 H_d \tag{B.1}$$

$$p_1 = \frac{1}{2}(1 + cos\beta)(\lambda_1\alpha_1 + \lambda_2 a_* cos^2\beta)\rho g H_d \tag{B.2}$$

$$p3 = \alpha_3 p_1 \tag{B.3}$$

$$p4 = \alpha_4 p_1 \tag{B.4}$$

$$p_u = 0.5(1 + cos\beta)\lambda_3\alpha_1\alpha_3\rho g H_d \tag{B.5}$$

$$\alpha_* = \alpha_2 \qquad \text{for non breaking waves} \tag{B.6}$$

$$\alpha_1 = 0.6 + \frac{1}{2}\left[\frac{4\pi h}{sinh(4\pi h)}\right]^2 \tag{B.7}$$

$$\alpha_2 = min\left\{\frac{h_b - d}{3h_b}\left(\frac{H_d}{d}\right)^2, \frac{2d}{H_d}\right\} \tag{B.8}$$

$$\alpha_3 = 1 - \frac{h'}{h}\left[1 - \frac{1}{cosh(2\pi h/L_d)}\right] \tag{B.9}$$

$$\alpha_4 = \begin{cases} \left(1 - \dfrac{h_c}{\eta^*}\right) & \eta^* > h_c \quad \text{(B.10a)} \\ 0 & \eta^* \leq h_c \quad \text{(B.10b)} \end{cases}$$

Where:

$\eta*$	=Elevation to which the wave pressure is exerted	$[m]$
β	=Angle between wave propagation line and a normal to the breakwater line	$[rad]$
H_d	=Unreflected design wave height	$[m]$
L_d	=Design wave length	$[m]$
p_1	=Wave pressure at still water level	$[Pa]$
p_3	=Wave pressure at sea bed level	$[Pa]$
p_4	=Wave pressure at $\eta*$	$[Pa]$
p_u	=Uplift pressure at front of structure	$[Pa]$
α_*	=Pressure coefficient that accounts for wave impact	$[-]$
α_1	=Pressure coefficient that accounts for wave length of design wave	$[-]$
α_2	=Pressure coefficient that accounts for wave steepness	$[-]$
α_3	=Pressure coefficient that accounts for the decrease in wave pressure over depth	$[-]$
$\lambda_{1,2,3}$	=Modification factors that account for the geometry of the structure	$[-]$
h_b	=Water depth in front of the structure, 5 wave lengths away front the wall	$[m]$
hc	=Height between SWL and top of caisson	$[m]$
h	=Depth in front of the rubble mound	$[m]$
h'	=Height of vertical breakwater	$[m]$
d	=Depth in front of the structure	$[m]$

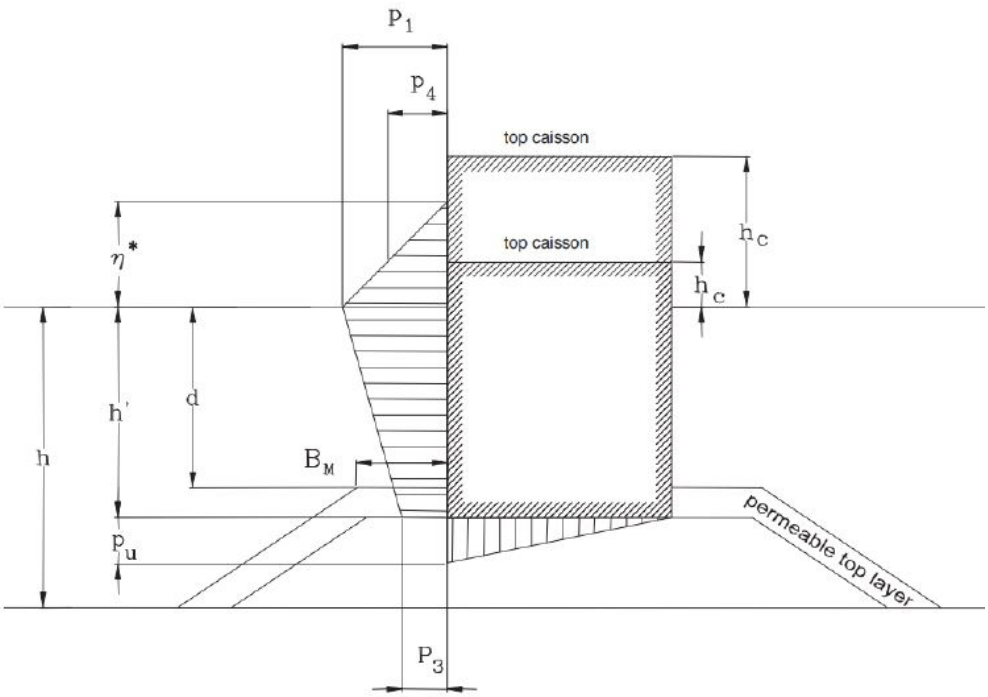

Figure B.1: Wave pressure distribution according to Goda (1974). Image taken from Veendorp and Niemijer (2003)

.

Goda (1974) uses the significant wave height $H_d = H_{1/3}$ and peak period $T_d = T_{1/3}$ as design parameters, and assumes a trapezoidal pressure distribution as shown in Figure B.1.

B.2. Reflection Analysis

The reflection analysis of the obtained signal is done according to Zelt and Skjelbreia (1993). In this paper, a method based on linear wave theory is presented which is used to decompose a one dimensional wave signal in left and right wave travelling components for an arbitrary number of wave gauges. Using standard Fourier analysis techniques, the right and left wave components can be calculated as shown in Equations B.11, B.12

and B.13.

$$\alpha_{Lj} = \left[S_j \sum_{p=1}^{P} W_{j,p} A_{j,p} e^{-i\Delta\phi_{j,p}} - \sum_{p=1}^{P} W_{j,p} A_{j,p} e^{i\Delta\phi_{j,p}} \sum_{q=1}^{P} W_{j,q} e^{-2i\Delta\phi_{j,q}} \right] \frac{e^{-i\phi_{j,1}}}{D} \tag{B.11}$$

$$\alpha_{Rj} = \left[S_j \sum_{p=1}^{P} W_{j,p} A_{j,p} e^{i\Delta\phi_{j,p}} - \sum_{p=1}^{P} W_{j,p} A_{j,p} e^{-i\Delta\phi_{j,p}} \sum_{q=1}^{P} W_{j,q} e^{2i\Delta\phi_{j,q}} \right] \frac{e^{i\phi_{j,1}}}{D} \tag{B.12}$$

$$D = S_j^2 - \sum_{p=1}^{P} W_{j,p} e^{2i\Delta\phi_{j,p}} e^{-2i\Delta\phi_{j,q}} = 4 \sum_{p=1}^{P} \sum_{q \le P} W_{j,p} W_{j,q} sin^2 \Delta\phi_{j,pq} \tag{B.13}$$

where

$$\Delta\phi_{j,pq} = \Delta\phi_{j,p} - \Delta\phi_{j,q} = \phi_{j,p} - \phi_{j,q} = k_j (x_p - x_q) \tag{B.14}$$

In the equations above, $\omega_j = 2\pi j/T$, T is the length of the time series, $k_j = 2\pi/\lambda_j$ is the wave number which can be related to ω_j by using the dispersion relation $\omega_j^2 = g k_j tanh(kd)$, d is the water depth, g is the gravitational acceleration and $S_j \equiv \sum_{p=1}^{P} W_{k,p}$. The time t is discrete for a sampled signal ($t \rightarrow m\Delta t$, for $m = 0, 1, 2..., N-1$, with $\Delta t = T/N$. Lastly, $W_{j,p}$ are weighting factors for the different wave gauges.
The sensitivity of the above formulas to errors in measuring the Fourier coefficients ($A_{j,p}$) at a given frequency ω_j depends on the choice of the weighting coefficients $W_{j,p}$ as well as the spacing of the wave gauges relative to the wave length associated with ω_j. For this reason, the selection of the positioning of the wave gauges is of major importance for the reflection analysis.
The largest amplification of errors for an arbitrary number of wave gauges occurs if the number $sin\Delta\phi_{j,pq} = n\frac{x_p - x_q}{\lambda_j}$ is an integer for each combination of p and q, where p and q denote wave gauge number ($p = 1, 2, ..., P$ and $q = 1, 2, ..., P$). This validation is shown in Tables B.1 and B.2 for the four wave gauges $W.G.2, W.G.3 W.G.4$ and $W.G.5$ that were used for the reflection analysis. It may be noticed in B.2 that the fraction $\frac{x_p - x_q}{\lambda_j}$ is never an integer or equal to 0.5.

Table B.1: Positioning of wave gauges

Wave Gauge	**Position [m]**
W.G. 1	3.35
W.G. 2	16.2
W.G. 3	16.9
W.G. 4	17.3
W.G. 5	17.6
W.G. 6	33.33

Table B.2: Validation of positioning of wave gauges. On the left column λ_p is the different wave lengths used during the experiments.

	x_3-x_2	x_4-x_2	x_5-x_2	x_4-x_3	x_5-x_3	x_5-x_4
	0.65	1.10	1.35	0.45	0.65	0.25
$L_p[m]$	$(x_p-x_q)/L_p[-]$					
7.33	0.10	0.15	0.18	0.05	0.09	0.03
6.67	0.11	0.17	0.20	0.06	0.10	0.04
6.29	0.11	0.18	0.21	0.06	0.10	0.04
6.00	0.12	0.18	0.23	0.07	0.11	0.04
5.71	0.12	0.19	0.24	0.07	0.11	0.04
5.50	0.13	0.20	0.25	0.07	0.12	0.05
5.33	0.13	0.21	0.25	0.08	0.12	0.05
5.14	0.14	0.21	0.26	0.08	0.13	0.05
5.00	0.14	0.22	0.27	0.08	0.13	0.05
4.67	0.15	0.24	0.29	0.09	0.14	0.05
4.57	0.15	0.24	0.30	0.09	0.14	0.05
4.50	0.16	0.24	0.30	0.09	0.14	0.06
4.00	0.18	0.28	0.34	0.10	0.16	0.06
3.50	0.20	0.31	0.39	0.11	0.19	0.07
3.43	0.20	0.32	0.39	0.12	0.19	0.07
3.33	0.21	0.33	0.41	0.12	0.20	0.08
3.00	0.23	0.37	0.45	0.13	0.22	0.08
2.86	0.25	0.39	0.47	0.14	0.23	0.09
2.50	0.28	0.44	0.54	0.16	0.26	0.10

B.3. Recurved parapet pressure

This section presents the methodology by Castellino et al. (2018) that is followed in Section 2.2 to estimate pressures on a recurved parapet. This study performs various numerical experiments of recurved parapets with various exit angles and recurve radius. An extension of the Goda (1974) is suggested that can be used in order to calculate pressure on a recurve parapet as a result of a wave impact. This formula reads as shown in Equation B.15.

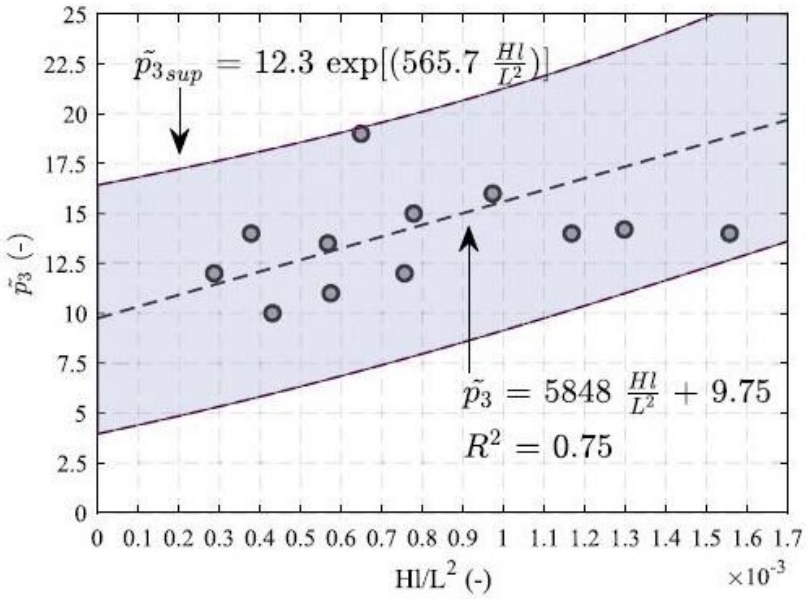

Figure B.2: Dependence of $\tilde{p}_3$ on the non-dimensional parameter Hl/L^2 and the linear fitting line. l, H and L represent the overhang, the regular wave height and the wavelength respectively. Image taken from Castellino et al. (2021)

.

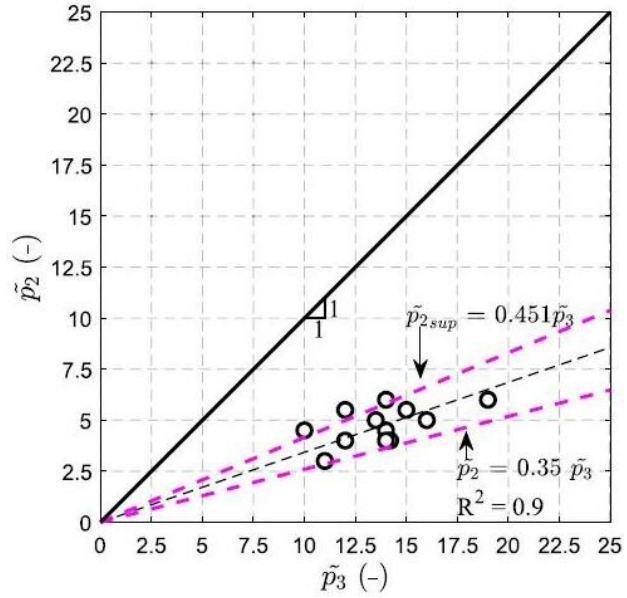

Figure B.3: Scatter plot between $\tilde{p}_2$ and $\tilde{p}_3$ pressure values and the linear fitting line. Image taken from Castellino et al. (2021)

.

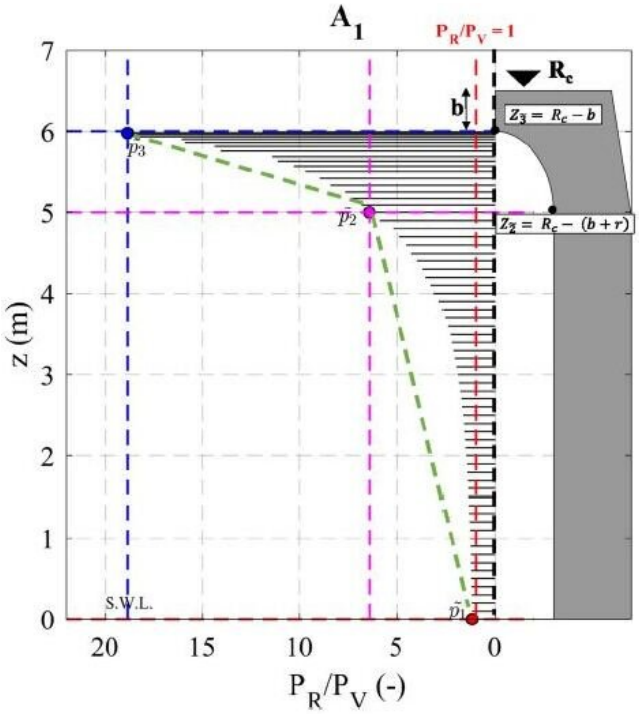

Figure B.4: Impulsive pressure distribution and dimensionless pressure values of $\tilde{p}_1$, $\tilde{p}_2$ and $\tilde{p}_3$. Image taken from **?**

.

$$P_R = P_V + \tilde{p}P_V = P_v(1 + \tilde{p}) \tag{B.15}$$

Where P_R is the pressure on the recurved parapet, P_V is the pressure on the vertical wall according to *Goda* formula, $\tilde{p} = P_R/P_V$ is the non-dimensional parametric pressure distribution acting on the recurved parapet (above the *SWL*). This extension can be used to calculate pressure on three points of the parapet as shown in Figure B.4, at SWL ($\tilde{p}_1$), at the starting point of the recurve ($\tilde{p}_2$) and at the outer top edge of the

recurve ($\tilde{p_3}$). This study assumes that $\tilde{p_1} = 1$, while the values of $\tilde{p_2}$ and $\tilde{p_3}$ can be calculated by using Figures B.2 and B.3 .

B.4. Smooth function

The Matlab function *smooth* is used in order to approximate the quasi-static part of the pressure signals, as demonstrated in Subsection 2.2.3. This funtions smooths the response data by using a moving average filter. For example, the first few elements of the pressure signal vector p is modified to $pp = smooth(p)$ as follows.

$$pp(1) = p(1) \tag{B.16}$$

$$pp(2) = (p(1) + p(2) + p(3))/3 \tag{B.17}$$

$$pp(3) = (p(1) + p(2) + p(3) + p(4) + p(5))/5 \tag{B.18}$$

$$pp(4) = (p(2) + p(3) + p(4) + p(5) + p(6))/5 \tag{B.19}$$

The advantage of this method is that the option *"rloess"* can be employed. This command performs a local regression using weighted linear least squares and a 2^{nd} degree polynomial model. This method assigns lower weight to outliers in the regression, while it assigns zero weight to data outside six mean absolute deviation. Applying this command on the impulsive pressure signals results in a smooth quasi static signal, as the outlying peak impulsive pressure moments are assigned a zero weight value.

Abbreviations

Abbreviation	*Description*
ARC	Active reflection compensation
$C-CI$	Confined crest impact
OE	Overtopping event
PS	Pressure sensor
SWL	Still water level
$S1$	Vertical wall
$S2$	Crownwall with a fully curved face
WE	Wave event
WG	Wave gauge

List of Figures

List of Tables

List of Symbols

Greek Symbols

Symbol	*Description*	*Units*
$\alpha_{\zeta 1}$	First fit coefficient of force point of application formula for crownwall with a fully curved face	[−]
$\alpha_{\zeta 2}$	Second fit coefficient of force point of application formula for crownwall with a fully curved face	[−]
$\alpha_{\theta 1}$	First fit coefficient of force formula for crownwall with a fully curved face	[−]
$\alpha_{\theta 2}$	Second fit coefficient of force formula for crownwall with a fully curved face	[−]
$\alpha_{\theta 3}$	Third fit coefficient of force formula for crownwall with a fully curved face	[−]
α_{f1}	First fit coefficient of force formula for crownwall with a fully curved face	[−]
α_{f2}	Second fit coefficient of force formula for crownwall with a fully curved face	[−]
α_{f3}	Third fit coefficient of force formula for crownwall with a fully curved face	[−]
α_{f4}	Fourth fit coefficient of force formula for crownwall with a fully curved face	[−]
α_{I1}	First fit coefficient of impulse formula for crownwall with a fully curved face	[−]
α_{I2}	Second fit coefficient of impulse formula for crownwall with a fully curved face	[−]
α_{I3}	Third fit coefficient of impulse formula for crownwall with a fully curved face	[−]
α_{p1}	First fit coefficient of pressure formula for crownwall with a fully curved face	[−]
α_{p2}	Second fit coefficient of pressure formula for crownwall with a fully curved face	[−]
α_{p3}	Third fit coefficient of pressure formula for crownwall with a fully curved face	[−]
α_{t1}	First fit coefficient of impulse duration formula for crownwall with a fully curved face	[−]
α_{t2}	Second fit coefficient of impulse duration formula for crownwall with a fully curved face	[−]
$\alpha_{q1,S1}$	First fit coefficient of overtopping formula for vertical wall	[−]
$\alpha_{q2,S1}$	Second fit coefficient of overtopping formula for vertical wall	[−]
$\alpha_{q3,S1}$	Third fit coefficient of overtopping formula for vertical wall	[−]
$\alpha_{q1,S2}$	First fit coefficient of overtopping formula for crownwall with a fully curved face	[−]
$\alpha_{q2,S2}$	Second fit coefficient of overtopping formula for crownwall with a fully curved face	[−]
$\alpha_{q3,S2}$	Third fit coefficient of overtopping formula for crownwall with a fully curved face	[−]
α_1	Goda formula pressure coefficient that accounts for the wave length of design wave	[−]
α_2	Goda formula pressure coefficient that accounts for the wave steepness	[−]
α_3	Goda formula pressure coefficient that accounts for the decrease in wave pressure over depth	[−]
α_4	Goda formula relative run up coefficient	[−]
$\alpha*$	Pressure coefficient that accounts for the wave impact	[−]
β	Goda formula angle between wave direction and a line normal to the breakwater	$[rad]$
ζ	Force application point in the vertical relative to mean still level	$[m]$
ζ_i	Force application point in the vertical relative to mean still level of wave event i	$[m]$
η_{in}	Incoming water elevation signal	$[m]$
η_{ref}	Reflected water elevation signal	$[m]$
$\eta*$	Goda formula elevation to which pressure is exerted	$[m]$
θ	Force angle relative to flat bottom	[°]
θ_i	Force angle relative to flat bottom of wave event i	[°]
ρ	Density of water	$[kg/m^3]$
ϕ	Angle of pressure sensors relative to the ground [°]	

Latin Symbols

Symbol	*Description*	*Units*
A	Integration area of force	$[m^2]$
A_j	Integration area of pressure sensor j	$[m^2]$
d	Water depth in front of the structure	$[m]$
f_s	Instrument sampling rate	$[kHz]$
F	Wave force	$[N]$
F_{max}	Maximum pressure	$[N]$
$F_{tot,i}$	Total maximum force of wave event i	$[N]$
$F_{x,i}$	Maximum force in the x direction of wave event i	$[N]$
$F_{y,i}$	Maximum force in the y direction of wave event i	$[N]$
g	Gravity constant	$[m/s^2]$
H	Wave height	$[m]$
$H_{1/3}$	Significant wave height	$[m]$
H_d	Goda formula design wave height	$[m]$
H_{in}	Incoming wave height	$[m]$
$H_{in,i}$	Incoming wave height of single wave i	$[m]$
H_{m0}	Significant wave height	$[m]$
H_{in}	Reflected wave height	$[m]$
$H_{ref,i}$	Reflected wave height of wave event i	$[m]$
$I_{i,j}$	Impulse area of wave event i and signal of pressure sensor j	$[Pa \times s]$
K_r	Reflection coefficient	$[-]$
$K_{r,i}$	Reflection coefficient for wave event i	$[-]$
L	Wave length	$[m]$
$L_{in,i}$	Incoming wave length of wave event i	$[m]$
$L_{ref,i}$	Reflected wave length of wave event i	$[m]$
$L_{m-1,0}$	Deep water wave length	$[m]$
$P_{i,j}$	Maximum pressure of wave event i and $PS\ j$	$[Pa]$
P	Wave pressure	$[N/m^2]$
q	Overtopping discharge	$[m^3/s/m$
R_c	Crest freeboard	$[m]$
s	Wave steepness	$[-]$
$s_{m-1,0}$	Deep water wave steepness	$[-]$
t	Time	$[s]$
$t_{w,i}$	Wave starting moment	$[s]$
T	Wave period	$[s]$
$T_{1/3}$	Significant wave period	[s]
$t_{imp,i}$	Impulse duration of wave event i	$[s]$
$T_{in,i}$	Incoming wave period of wave event i	$[s]$
$T_{ref,i}$	Reflected wave period of wave event i	$[s]$
$t_{w,i}$	Zero-down crossing start moment of a wave event	$[s]$
$t_{start,i+1}$	Zero-down crossing starting en of a wave event	$[s]$
U	Ursell number	$[-]$
U_i	Ursell number of wave event i	$[-]$

Bibliography

Nigel William Henry Allsop and Tom Bruce. Failure analysis of historic vertical breakwaters, part 2: Alderney, guernsey and dover, uk. *Proceedings of the Institution of Civil Engineers-Forensic Engineering*, pages 1–12, 2020a.

Nigel William Henry Allsop and Tom Bruce. Failure analysis of historic vertical breakwaters, part 1: Wick. *Proceedings of the Institution of Civil Engineers-Forensic Engineering*, 172(2):43–53, 2020b.

N.W.H. Allsop and M. Calabrese. *Impact Loadings on Vertical Walls in Directional Seas*, pages 2056–2068. 1998.

NWH Allsop, JE McKenna, Diego Vicinanza, and TTJ Whittaker. New design methods for wave impact loadings on vertical breakwaters and seawalls. In *Coastal Engineering 1996*, pages 2508–2521. 1997.

W Allsop, Diego Vicinanza, and JE McKenna. Wave forces on vertical and composite breakwaters. 1996.

R A Bagnold. Interim report on wave-pressure research. (includes plates and photographs). *Journal of the Institution of Civil Engineers*, 12(7):202–226, 1939. doi: 10.1680/ijoti.1939.14539.

Phillip Besley. Wave overtopping of seawalls, design and assessment manual. *R&D technical report W178*, 1998.

PA Blackmore and PJ Hewson. Experiments on full-scale wave impact pressures. *Coastal Engineering*, 8(4): 331–346, 1984.

M Castellino, P Sammarco, A Romano, L Martinelli, P Ruol, L Franco, and P De Girolamo. Large impulsive forces on recurved parapets under non-breaking waves. a numerical study. *Coastal Engineering*, 136:1–15, 2018.

Myrta Castellino, Javier Lara, Alessandro Romano, I. Losada, and Paolo de girolamo. Wave loading for recurved parapet walls in non-breaking wave conditions: Analysis of the induced impulsive forces. 01 2019.

Myrta Castellino, Alessandro Romano, Javier L Lara, Iñigo J Losada, and Paolo De Girolamo. Confined-crest impact: Forces dimensional analysis and extension of the goda's formulae to recurved parapets. *Coastal Engineering*, 163:103814, 2021.

Xuexue Chen, Bas Hofland, Wilfred Molenaar, Alex Capel, and Marcel R.A. Van Gent. Use of impulses to determine the reaction force of a hydraulic structure with an overhang due to wave impact. *Coastal Engineering*, 147:75–88, 2019. ISSN 0378-3839. doi: https://doi.org/10.1016/j.coastaleng.2019.02.003. URL `https://www.sciencedirect.com/science/article/pii/S0378383918302990`.

Yung-Fang Chiu, Jaw-Guei Lin, Shang-Chun Chang, Yin-Jei Lin, and Chia-Hsin Chen. An experimental study of wave forces on vertical breakwater. *Journal of Marine science and technology*, 15(3):158–170, 2007.

MJ Cooker and DH Peregrine. A model for breaking wave impact pressures. In *Coastal Engineering 1990*, pages 1473–1486. 1991.

A Cornett, Y Li, and A Budvietas. Wave overtopping at chamfered and overhanging vertical structures. In *Proc. International Workshop on Natural Disasters by Storm Waves and Their Reproduction in Experimental Basins, Kyoto, Japan*, 1999.

Giovanni Cuomo, William Allsop, Tom Bruce, and Jonathan Pearson. Breaking wave loads at vertical seawalls and breakwaters. *Coastal Engineering*, 57(4):424–439, 2010a.

Giovanni Cuomo, William Allsop, and Shigeo Takahashi. Scaling wave impact pressures on vertical walls. *Coastal Engineering*, 57(6):604–609, 2010b.

Ermano de Almeida and Bas Hofland. Experimental observations on impact velocity and entrapped air for standing wave impacts on vertical hydraulic structures with overhangs. *Journal of Marine Science and Engineering*, 8(11):857, 2020a.

Ermano de Almeida and Bas Hofland. Validation of pressure-impulse theory for standing wave impact loading on vertical hydraulic structures with short overhangs. *Coastal Engineering*, page 103702, 2020b.

A. de Rouville, P. Besson, and P. Petry. *État actuel des études internationales sur les efforts dus aux lames*. 1938. URL `https://books.google.gr/books?id=_SDCoAEACAAJ`.

Dimitrios Dermentzoglou, Myrta Castellino, Paolo De Girolamo, Maziar Partovi, Gerd-Jan Schreppers, and Alessandro Antonini. Crownwall failure analysis through finite element method. *Journal of Marine Science and Engineering*, 9(1):35, 2021.

Maarten W Dingemans. *Water wave propagation over uneven bottoms*, volume 13. World Scientific, 1997.

MW Dingemans, AC Radder, and HJ De Vriend. Computation of the driving forces of wave-induced currents. *Coastal Engineering*, 11(5-6):539–563, 1987.

Yoshimi Goda. New wave pressure formulae for composite breakwaters. In *Coastal Engineering 1974*, pages 1702–1720. 1974.

I Hiroi. The force and power of waves. *The Engineer*, 130:184–185, 1920.

Bas Hofland, Mirek Kaminski, and Guido Wolters. Large scale wave impacts on a vertical wall. *Coastal Engineering Proceedings*, 1(32):15, 2010.

Ole Juul Jensen. *A monograph on rubble mound breakwaters*. Danish Hydraulic Institute, 1984.

M Salih Kirkgöz. An experimental investigation of a vertical wall response to breaking wave impact. *Ocean Engineering*, 17(4):379–391, 1990.

M Salih Kirkgöz. Impact pressure of breaking waves on vertical and sloping walls. *Ocean Engineering*, 18(1-2): 45–59, 1991.

M Salih Kirkgöz. Influence of water depth on the breaking wave impact on vertical and sloping walls. *Coastal engineering*, 18(3-4):297–314, 1992.

MS Kirkgöz. Breaking wave impact on vertical and sloping coastal structures. *Ocean Engineering*, 22(1):35–48, 1995.

A Kortenhaus, R Haupt, and H Oumrraci. Design aspects of vertical walls with steep foreland slopes. In *Breakwaters, coastal structures and coastlines: Proceedings of the international conference organized by the Institution of Civil Engineers and held in London, UK on 26-28 September 2001*, pages 220–232. Thomas Telford Publishing, 2002.

Andreas Kortenhaus, J Pearson, T Bruce, NWH Allsop, and JW Van der Meer. Influence of parapets and recurves on wave overtopping and wave loading of complex vertical walls. In *Coastal Structures 2003*, pages 369–381. 2004.

Bernard Le Méhauté. *An introduction to hydrodynamics and water waves*. Springer Science & Business Media, 2013.

MA Losada, FL Martin, and R Medina. Wave kinematics and dynamics in front of reflective structures. *Wave Forces on Inclined and Vertical Wall Structures*, pages 282–310, 1995.

JG Marinski and H Oumeraci. Dynamic response of vertical structures to breaking wave forces–review of the cis design experience. In *Coastal Engineering 1992*, pages 1357–1370. 1993.

L Martinelli, P Ruol, M Volpato, C Favaretto, M Castellino, P De Girolamo, L Franco, A Romano, and P Sammarco. Experimental investigation on non-breaking wave forces and overtopping at the recurved parapets of vertical breakwaters. *Coastal Engineering*, 141:52–67, 2018.

Robert C Royal Minikin. *Winds, waves, and maritime structures: Studies in harbour making and in the protection of coasts*. Griffin, 1963.

Jorge Molines, Arnau Bayón, M. Esther Gómez-Martín, and Josep R. Medina. Numerical study of wave forces on crown walls of mound breakwaters with parapets. *Journal of Marine Science and Engineering*, 8(4), 2020. ISSN 2077-1312. doi: 10.3390/jmse8040276. URL https://www.mdpi.com/2077-1312/8/4/276.

Hocine Oumeraci, Andreas Kortenhaus, William Allsop, Maarten de Groot, ROGER Crouch, H Vrijling, and HESSEL Voortman. *Probabilistic design tools for vertical breakwaters*. CRC Press, 2001.

MW Owen and AAJ Steele. Effectiveness of recurved wave return walls. 1993.

Jon Pearson, Tom Bruce, William Allsop, Andreas Kortenhaus, and JENTSJE van der Meer. Effectiveness of recurve walls in reducing wave overtopping on seawalls and breakwaters. In *Coastal Engineering 2004: (In 4 Volumes)*, pages 4404–4416. World Scientific, 2005.

Jan Pedersen and Hans F Burcharth. Wave forces on crown walls. In *Coastal Engineering 1992*, pages 1489–1502. 1993.

C Ramkema. A model law for wave impacts on coastal structures. In *Coastal Engineering 1978*, pages 2308–2327. 1978.

George Bishop Roux. *Reduction of seawall overtopping at the Strand*. PhD thesis, Stellenbosch: Stellenbosch University, 2013.

George Sainflou. Essai sur les digues maritimes verticales. *Annales de ponts et chaussÈes, vol 98, tome II, 1928 (4) pp 5-48*, 1928.

Talia Schoonees. *Impermeable recurve seawalls to reduce wave overtopping*. PhD thesis, Stellenbosch: Stellenbosch University, 2014.

Dimitris Stagonas, Javier L Lara, Inigo J Losada, Pablo Higuera, Francisco F Jaime, and Gerald Muller. Large scale measurements of wave loads and mapping of impact pressure distribution at the underside of wave recurves. In *Proceedings of the HYDRALAB IV Joint User Meeting*, 2014.

Thomas Stevenson. *The design and construction of harbours: a treatise on maritime engineering*. A. and C. Black, 1886.

S Takahashi. Experimental study on impulsive pressures on composite breakwaters. *Rep. Port Harbor Res. Inst.*, 31(5):33–72, 1993.

S Takahashi, S Hosoyamada, and S Yamamoto. Hydrodynamic characteristics of sloping top caissons. In *Proceedings of International Conference on Hydro-technical Engineering for Port and Harbour Construction, PHRI*, 1994.

Shigeo Takahashi. Design of vertical breakwaters. *PHRI reference document nr. 34*, 2002.

K Tanimoto, K Moto, S Ishizuka, and Y Goda. An investigation on design wave force formulae of composite-type breakwaters. In *Proc. 23rd Japanese Conf. Coastal Eng*, pages 11–16, 1976.

Vicente Negro Valdecantos, José Santos López Gutiérrez, Jose Ignacio Polvorinos Flors, and Jorge Molines. Discussion: Comparative study of breakwater crown wall–calculation methods. In *Proceedings of the Institution of Civil Engineers-Maritime Engineering*, volume 167, pages 154–155. Thomas Telford Ltd, 2014.

J. W. van der Meer, NWH Allsop, T. Bruce, Julien De Rouck, Andreas Kortenhaus, T. Pullen, H. Schüttrumpf, Peter Troch, and B. Zanuttigh. *EurOtop: Manual on wave overtopping of sea defences and related sturctures : an overtopping manual largely based on European research, but for worlwide application*. 2016.

M Veendorp and J Niemijer. Leidraad kunstwerken. *L15 DWW2003-059-isbn 9026955440*, 2003.

Th Von Karman. The impact on seaplane floats during landing. 1929.

Jessica Zelt and James Eric Skjelbreia. Estimating incident and reflected wave fields using an arbitrary number of wave gauges. 1993.